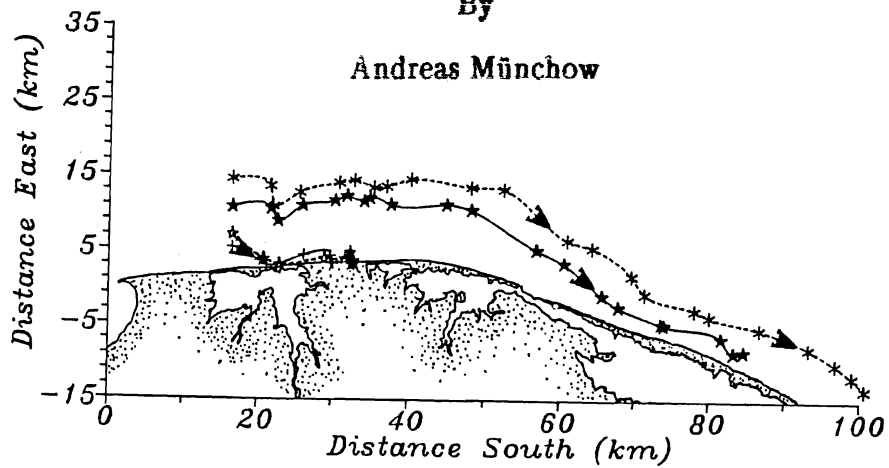


THE FORMATION OF A BUOYANCY DRIVEN COASTAL CURRENT

By

Andreas Münchow



A dissertation submitted to the Faculty of the University of Delaware in partial fulfillment of the requirements for the degree of Doctor of Philosophy in Oceanography

May 1992

THE FORMATION OF A
BUOYANCY DRIVEN COASTAL CURRENT

By

Andreas Münchow


Approved:

Carolyn A. Thoroughgood, Ph.D.
Dean of the College of Marine Studies


Approved:

Carol E. Hoffecker, Ph.D.
Acting Associate Provost for Graduate Studies

I certify that I have read this dissertation and that in my opinion it meets the academic and professional standard required by the University as a dissertation for the degree of Doctor of Philosophy.

Signed: 
Richard W. Garvine, Ph.D.
Professor in charge of dissertation

I certify that I have read this dissertation and that in my opinion it meets the academic and professional standard required by the University as a dissertation for the degree of Doctor of Philosophy.

Signed: 
Kuo-Chuin Wong, Ph.D.
Member of dissertation committee

I certify that I have read this dissertation and that in my opinion it meets the academic and professional standard required by the University as a dissertation for the degree of Doctor of Philosophy.

Signed: 
David C. Chapman, Ph.D.
Member of dissertation committee

I certify that I have read this dissertation and that in my opinion it meets the academic and professional standard required by the University as a dissertation for the degree of Doctor of Philosophy.

Signed: 
James O'Donnell, Ph.D.
Member of dissertation committee

ACKNOWLEDGEMENTS

The crew of the R/V Cape Henlopen under Captain Don McCann lived up to their reputation. Every trip was an exciting experience. From Tim Pfeiffer I learnt at sea a new computer language on each of four experiments; he taught me the ADCP, designed a superb shipboard data acquisition system, and, finally, let me exploit it for real time data analysis.

Dr. Richard W. Garvine served as my principal advisor and as the Chief Scientist. He did not, however, interfere with my often chaotic juggling of data. While supervising students myself, I noticed how hard it is to accept the working style of someone else. Rich teaches by example and hard work. He did not even forget the "P" in PhD, and my years with him included E110, Thoreau, and Chaucer. Drs. David Chapman, James O'Donnell, and Kuo-Chuin Wong were all very active committee members. During two experiments at sea with Kuo I saw that a Chief Scientist has to do work, lots of it, actually. Jim always encouraged me to do more while Dave, despite being 500 miles away, always responded quickly, pointedly, and critically.

Theoretical discussions with Dr. John McCalpin and the keen interest of Dr. Pablo Huq opened new perspectives and earned me some

Guinness Stout. Drs. Geyer, Candela, Foreman, Lwiza, and Royer all shared their views on the ADCP and coastal dynamics with me. Rich was instrumental in all these contacts as he continuously supported my travels to Cape Cod, New Orleans, Alaska, the Netherlands, and Wales.

The success of the drifter study depended crucially upon Art Sundberg and Robert McCarthy. Bob went to sea catching drifters only to give them back to the sea goddess. I was home to direct him via a radio link, but that contact broke down more often than not. Nevertheless, Bob lost no drifter. His cool restraint matched my enthusiastic willingness to take risks. Together, I think, we optimized our different strengths designing drifter studies. Les, Tim and Claudia, Joy, Glen, Doug, Ann, and Jürgen shared hands and brains on the project. Claudia also helped with software on the SUN. Xin, Jinhua, Todd, Chandrasekar, and Mary all participated in our enjoyable weekly group meetings. Sheila, I love the car and hope it will stay my largest one.

Finally, Mary Ann provided lasting, honest, and challenging companionship with her two wonderful sons, David and Daniel. I loved the "tidal wave," the "clay fight," and the "cliff climbing" games the best. Mary Ann, you taught me compromise and compassion. My sister Christina and brother-in-law, George, offered crucial shelter and bread when I needed it the most. The National Science Foundation of the United States funded this study through grant OCE-8816009 to Dr. R.W. Garvine.

To
Ilsebill

TABLE OF CONTENTS

List of Tables	viii
List of Figures	ix
Abstract	xiii
Chapter 1: Introduction	1
Chapter 2: Observational Overview	11
Chapter 3: The Source Region	27
Chapter 4: The Plume Region	67
Chapter 5: The Coastal Current Region	133
Chapter 6: An Instability	165
Chapter 7: Discussion and Parameters	183
References	196

LIST OF TABLES

3.1:	Subtidal buoyancy flux across transects	48
3.2:	Across-channel momentum balance	56
3.3:	Scales and parameters for the source region	65
4.1:	Summary of experiments and data sources	70
4.2:	Results of time domain statistics	81
4.3:	Eulerian statistics from drifters and current meters	98
4.4:	Along-shelf momentum balance off New Jersey	125
4.5:	Scales and parameters for the plume region	131
5.1:	Scales and parameters for the coastal current region	163

LIST OF FIGURES

1.1:	Map of the study area	8
2.1:	Salinity distribution in March 1952	12
2.2:	Salinity distribution in June 1990	14
2.3:	Salinity distribution in May 1989	15
2.4:	Map of principal axes of M_2 tidal currents	18
2.5:	Subtidal currents from S4 current meters	19
2.6:	Parameters and sketch of dynamical regions	25
3.1:	Bathymetry and stations of the source region	28
3.2:	The front of the source region on 06–18–1989	30
3.3:	Two vertical salinity profiles near a front	32
3.4:	Two drifter trajectories in the source region	33
3.5:	Temperature–Salinity diagrams	35
3.6:	Subtidal transects of density anomaly	37
3.7:	Principal axes for the M_2 surface currents	39

3.8:	Subtidal currents from ADCP profiling	40
3.9:	Tidal density, speed, and buoyancy flux at B2	44
3.10:	Transects of subtidal buoyancy flux per unit area	46
3.11:	As fig. 3.10, but for the shelf transect C	49
3.12:	Observed vs. geostrophic vertical current shear	53
3.13:	Subtidal momentum balance across the source region	57
3.14:	Horizontal current shear across transect B	60
3.15:	Potential vorticity across transect B	62
4.1:	Discharge, wind, and current time series	68
4.2:	Seven maps of surface salinity for the plume region	72
4.3:	Subtidal current vectors on salinity map in May 1990	77
4.4:	Lagged cross-correlations	83
4.5:	Coherencies of along-shore surface currents	85
4.6:	Locations and periods of drifter deployment	89
4.7:	Trajectories of all drifters	91
4.8:	Drifter trajectories sorted by wind direction	92
4.9:	Lagrangian auto-correlation function	96

4.10:	Eulerian statistics from drifter and current meter data	99
4.11:	Across-shore current profile from drifter data	102
4.12:	Results of drifter dispersion	106
4.13:	Maps of ADCP surface and bottom current vectors . . .	109
4.14:	Salinity distribution on transect C	111
4.15:	Comparison of Ekman with ADCP currents	116
4.16:	Vertical current profiles from ADCP data	118
4.17:	Thermal wind diagnostics for April and June 1989 . . .	120
4.18:	Time series of depth averaged along-shelf momentum . .	126
5.1:	Trajectories of 4 drifters	135
5.2:	Sea surface temperature from AVHRR on day 139	136
5.3:	Salinity and subtidal flow field in May 1990	138
5.4:	Salinity field in June 1990	140
5.5:	Plume of the Hudson River near its source	142
5.6:	Hudson Coastal Current 06-14-1989	144
5.7:	Hudson Coastal Current signals in time series	147
5.8:	Hudson Coastal Current 06-17-1989	148

5.9:	Retreat of the Hudson Coastal Current	150
5.10:	Transect of subtidal velocities 06–17–1989	152
5.11:	Coastal eddy off New Jersey	154
5.12:	Discharge, wind, current, and salinity time series . .	155
5.13:	Cross–correlation of discharge with surface salinities	157
5.14:	Thermal wind diagnostics for Delaware Coastal Current	161
6.1:	Instabilities from AVHRR sea surface temperature . . .	166
6.2:	ADCP and CTD transect locations on salinity map . . .	167
6.3:	Subtidal surface velocity vectors on salinity map . .	170
6.4:	Across–shore subtidal velocity transect	171
6.5:	ADCP and S4 current meter intercomparison	172
6.6:	Three successive along–shore density transects	173
6.7:	Along–shore subtidal velocity transect	175
7.1:	Along–shore variability of nondimensional parameters .	185

ABSTRACT

The influx of buoyant waters into the coastal ocean affects the dynamics there profoundly. Lateral density gradients induce pressure gradients which, if balanced geostrophically, force an along-shore current in the direction of Kelvin wave phase propagation. This dissertation describes two such currents which indeed are in geostrophic balance across the shelf. The Delaware Coastal Current receives its buoyancy from the Delaware Estuary, while the Hudson Coastal Current receives its buoyancy from the Hudson River. I give a detailed description of both these currents in the Mid-Atlantic Bight in this dissertation, but emphasize the Delaware Coastal Current more.

In 1989 and 1990 we repeatedly profiled the shelf with shipboard CTD and ADCP instruments. A thermo-salinograph provided data to construct maps of surface salinities which proved useful to interpret transect data in a three-dimensional context. I frequently identify frontal regions, instabilities, and eddies which I describe, analyze, and speculate on with data from current meters, clusters of satellite-tracked drifters, meteorological buoys, tide gauges, and space borne AVHRR sensors. I describe a complex but coherent three-dimensional flow and density field, analyze dominant balances estimated from data, and speculate on the dynamics with the aid of calculated Rossby (ϵ), Burger (S), and Ekman (E_V) numbers. Vorticity

ratios guide the interpretation of the large data set also.

The dynamical richness of the observed flow and density fields challenges present modeling capabilities, even though its basic ingredients are rather simple: Sloping isopycnals form an off-shore zone of large density gradients that reach the sloping bottom. Moderately upwelling favorable winds oppose the along-shore current, induce depth dependent across-shore flow, and thus reduce isopycnal slopes. Tidal mixing, on the other side, acts to homogenize the water column vertically, and thus enhances isopycnal slopes. Meanders and instabilities develop frequently. However, since downstream from the source region $\epsilon \leq S \ll 1$, I argue that a frontal geostrophic model on a topographic β -plane will serve as a first step to understand the findings reported in this dissertation.

CHAPTER 1: INTRODUCTION

1.1 Perspective

The German novelist Günter Grass retold the old folk tale of a people nourishing on the Vistula Estuary of what is now Poland. From time immemorial, so the tale goes, men have been advised by a god-like Flounder which pre-historic fishermen accidentally caught in their nets and let go. Since then the flounder appears, if called upon, for help, advice, and spiritual enlightenment. I cite the story of the Flounder as early evidence of human interaction with an estuarine and coastal environment. In the broadest sense that is the subject of this dissertation. More specifically, I will describe and partly explain how estuarine buoyancy fluxes affect the distribution of riverborne material and dynamics on the inner continental shelf in the vicinity of the Delaware Estuary on the eastern seaboard of North America.

Estuaries such as the Delaware Estuary discharge their load of brackish water into the salty coastal ocean. The density differences between brackish estuarine and salty oceanic water masses force a flow on the shelf. Density gradients induce pressure gradients which are often balanced by Coriolis forces. In the northern hemisphere such a balance turns the estuarine outflow to the right looking seaward. I call such currents

"buoyancy driven coastal currents." They are partly responsible for the distribution of riverborne nutrients, larvae, sediments, sewage, toxic chemicals, and oil from accidental spills. An example of such a spill occurred on March 23, 1989 as the M/T Exxon Valdez ran aground in Prince William Sound, Alaska, and released 11 million gallons of North Slope crude oil during the first 2 weeks of the accident. The local buoyancy driven coastal current advected the oil 290 km along the shelf while spreading it only 20 km across (Royer et al. 1990). Clean-up costs exceeded 1 billion U.S. dollars and legal litigation is still pending.

This study on the circulation of the inner continental shelf near the Delaware Estuary touches aspects of local dynamics which range from classical theories of wind driving (Ekman, 1905) to those of poorly understood submeso-scale vortices (Thompson and Young, 1989). The linear and nonlinear interaction of different physical processes in the presence of tides with the buoyancy driven coastal current adds to the complexity of the flow field I encountered. Therefore, this dissertation is more exploratory than final. Our data collecting array barely resolved the spatial and temporal variability of the dynamics on the inner shelf. I am thus more frequently raising new questions than answering them satisfactorily. The organization of this dissertation, however, emphasizes regions of different dynamics. After providing an observational overview in chapter 2, in the following chapters 3, 4, and 5 I discuss a source, plume, and coastal current region. Chapter 6 details an instability or eddy in the coastal current, and

the last chapter 7 concludes this study with a discussion of dominant scales and parameters. These properties are offered to guide future modeling studies on inner continental shelves in the presence of buoyancy.

1.2 Review of Outflow Dynamics

Woods and Beardsley (1988) studied estuarine outflow problems with a set of analytical, numerical, and laboratory experiments. They examined vorticity dynamics for fluids of constant density. The outflowing fluid enters a uniformly sloping shelf where vortex tube stretching and friction determines its path. Their studies relate indirectly to the discharge of water from major rivers, since they isolate barotropic from baroclinic effects. For small Rossby numbers Woods and Beardsley (1988) found that for small river discharge Csanady's (1978) arrested topographic wave dynamics resulted, while for moderate discharge they reproduced the one-layer results of Beardsley and Hart (1978), namely that outflowing estuarine waters turn to the right in the northern hemisphere. However, in their laboratory studies they discovered that for large Rossby numbers a cyclonic vortex appeared to the left of the outflow, whereas to the right (cum sole) a train of cyclonic and anti-cyclonic vortices formed. The last result is intriguing, since coastal currents are indeed often unstable (Johannessen et al., 1989). Further below I present evidence of both cyclonic and anti-cyclonic vortices within our study area.

Most outflows, however, are not barotropic, but transport buoyancy into the coastal ocean. Observations of buoyant outflows consistently stress the close correlation of coastal currents with buoyancy sources upstream. Simpson and Hill (1986) sketched the outflow of buoyant Irish Sea water along the west coast of Scotland to the north. There, a buoyancy driven, weak, but stable current system branches when it encounters a gap in the coastline. Also in Europe, the Rhine outflow forms a coastal current that influences the entire Dutch coastal zone. Intense field studies are presently underway and early results one finds in de Ruijter et al. (1990) and van der Giessen et al. (1990). In the South-Atlantic Bight on the eastern seaboard of the USA Blanton (1981) describes observations that indicate a buoyancy driven coastal current in thermal wind balance. In a different study Hickey et al. (1991) attributed about 15% of the variance of the Vancouver Island Coastal Current to buoyancy forcing from the Fraser River, British Columbia. Johannessen et al. (1989) and Mork (1981) described the Norwegian Coastal Current and its instabilities. Ikeda et al. (1989) sought to simulate these with a two layer quasi-geostrophic numerical model. Royer (1983), Johnson et al. (1988), and Åhlén et al. (1987) studied the Alaska Coastal Current, its seasonal variability, and instability, respectively. Tang (1980) and Mertz et al. (1988) studied the hydrography, evolution, and instabilities of the Gaspé Current in Canada. This current derives its buoyancy from the St. Lawrence River and appears as a shallow, buoyancy driven coastal jet. As the St. Lawrence River widens smoothly, its Kelvin number $K \equiv W/L_D$ increases to $O(1)$ inside the estuary and the coastal jet

emerges from the classical vertical two-layer gravitational circulation (Hansen and Rattray, 1965) under the influence of Coriolis force. Here W and L_D are the local width and internal deformation radius, respectively.

At the offshore edge of buoyant outflows the depth of the upper layer or plume often vanishes abruptly and forms a front with oceanic waters offshore. These estuarine plumes and fronts have motivated much modeling work. Garvine (1987) investigated the dynamics of such plumes with a reduced gravity, steady state, layer model. He treated fronts as discontinuities where frictional dissipation takes place. O'Donnell (1988) developed a numerical layer model which simulates time-dependent plume dynamics and fronts. There is a fundamental physical difference between reduced gravity (Garvine, 1987; O'Donnell, 1988) and barotropic models (Woods and Beardsley, 1988). For the former, bottom friction is usually negligible and an offshore traveling water parcel gains anti-cyclonic vorticity due to vortex tube squashing, since the upper layer depth decreases offshore toward the density front. In contrast, for the barotropic case bottom friction is a major term in the vorticity balance and an offshore parcel gains cyclonic vorticity due to vortex tube stretching because the total water depth increases offshore. Finally, for a baroclinic current that extends to the bottom, no simple interpretation is possible as now both a barotropic and a baroclinic response may occur. Further, two or more active layers may interact.

Buoyancy driven coastal currents are affected by other forcing agents besides pressure gradients which buoyancy gradients produce. Winds (Saetre et al., 1988; Hill and Simpson, 1988), variable bottom topography, strong tides in concert with topography (Zimmerman, 1980; Münchow et al. 1991a), and circulation produced by wind forced coastal upwelling (Chao, 1987; Barth, 1989; Petrie et al., 1987) complicate the flows considerably. A comprehensive approach to modeling buoyant outflow dynamics incorporates all these physical processes into a three-dimensional, numerical, primitive equation model. Weaver and Hsieh (1987) and Chao (1988) developed such "general circulation models" which concentrate on estuarine-shelf interactions under wind and buoyancy forcing. Particularly useful is the simulation of finite amplitude instabilities. Chao (1987) showed that buoyancy driven currents on the shelf are marginally unstable and that temporal changes in wind or buoyancy forcing could trigger instabilities. Send (1989) supports the finding that temporal changes in the wind field can lead to locally unstable flows. He describes observed flow fields off California after the relaxation of up-welling favorable winds and simulates the observation of a local instability with barotropic vorticity contour dynamics (Pratt and Stern, 1986; Stern, 1989). Such instabilities can evolve into cyclonic and anti-cyclonic vortices which are readily observed in the laboratory. Two laboratory studies which relate to the evolution of instabilities into eddies are Griffiths and Linden (1981) and Whitehead and Chapman (1986). The former authors studied the continuous release of a buoyant fluid from a point source into a rotating tank where a buoyancy

driven coastal current evolved and became unstable when it reached a critical width. Whitehead and Chapman (1986) measured the width and speed of propagation of the leading edge of such a current which they interpreted as the head of a gravity current (Simpson, 1987). In the next chapters I will show surface salinity contours which suggest the presence of such a gravity current off Delaware.

The wealth of theoretical and laboratory studies on buoyancy driven coastal currents would appear to treat all possibilities. But none of these studies applies to coastal currents of moderate strength on shallow continental shelves. Such flows are common; the Delaware and Hudson River outflows and the South-Atlantic Bight coastal current (Blanton, 1983) are three examples located nearby, while the Scottish Coastal Current (Simpson et al., 1989) and Rhine outflow (de Ruijter et al., 1990) are two examples far away.

1.3 Data Sources

From March through June 1989 we studied the flow and density field in an area of expected strong buoyancy driven flows in shallow water. The study area (fig. 1.1) centers on the mouth of the Delaware Estuary and extends 35 km offshore and 100 km alongshore. We collected both Eulerian and Lagrangian current data as well as extensive hydrography.

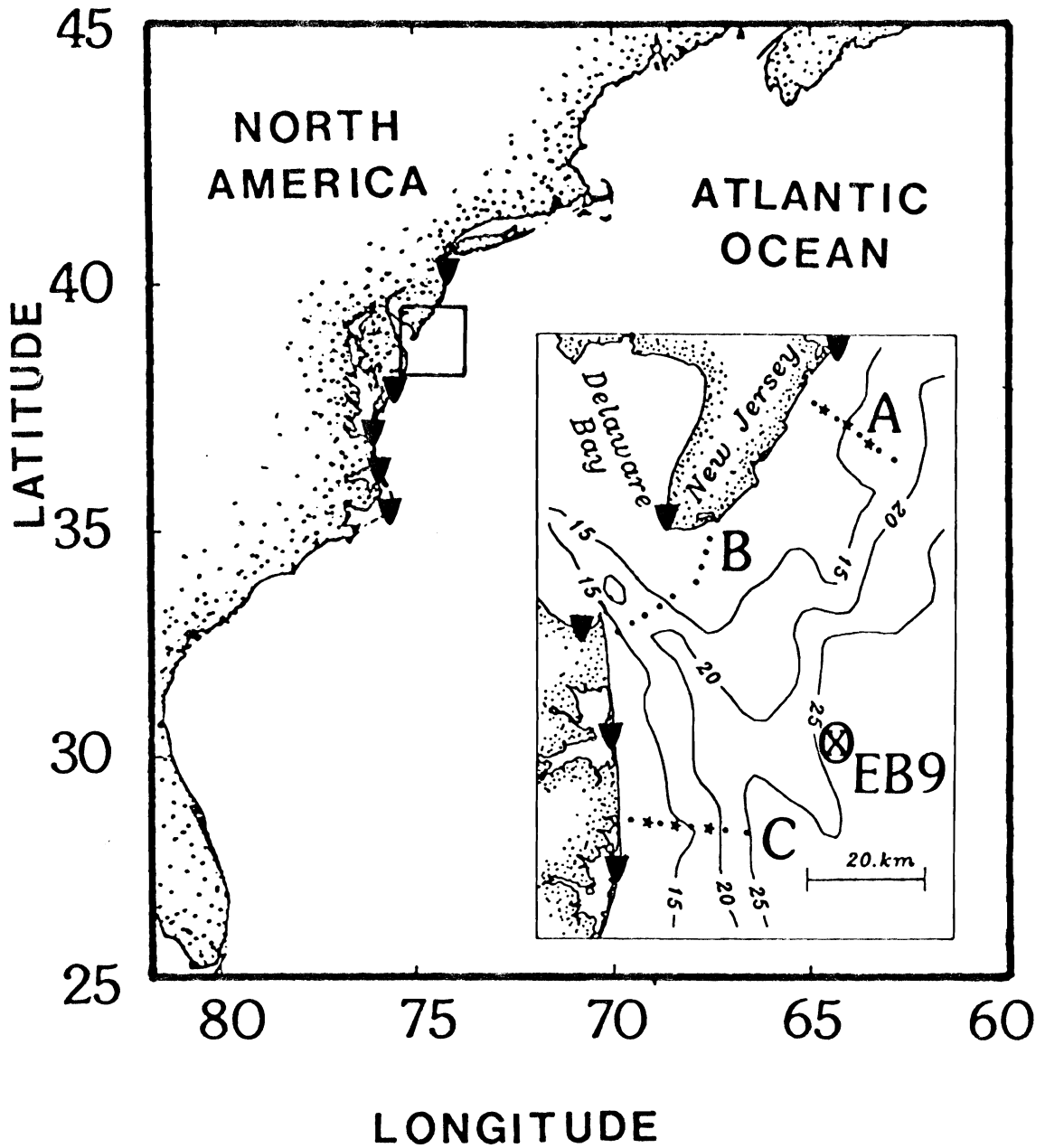


Figure (1.1). Map of the study area. The insert is an enlargement of the area near 38N and 75W. The triangles mark the location of coastal tide gauges and EB9 represents a meteorological buoy. I denote the three major transects as A, B, and C. Current meter mooring locations I depict as filled stars on transects A and C. The dots on each transect mark the location of CTD and ADCP stations.

A 307 kHz ship mounted acoustic Doppler current profiler (ADCP) of RDI Inc. and ten moored InterOcean S4 current meters (see fig. 1.1 for locations) provided Eulerian current measurements. Münchow et al. (1991b) describe the ADCP, its calibration, use, and performance, as well as the methodology to remove tidal currents from the data it returns. Also shown in fig. 1.1 are the location of six current meter moorings, four of which had two S4 meters attached to them at 6 m and 10 m below the surface. The most offshore moorings on transects A and C (see fig. 1.1) had only a single instrument at a depth of 6 m. The moorings were maintained from March through June 1989 and returned velocity, conductivity, and temperature data every half hour representing temporal averages of 5 minutes. From the latter data density time series can be computed. While the S4 data lack spatial coverage, especially in the vertical, they have excellent temporal coverage. The reverse is true for the ADCP data. Hence, these data sets complement each other.

The Lagrangian description of the flow field was obtained by satellite tracked drifters using the ARGOS system. Since the attached drogue was centered at 3 m depth, the data represent an estimate of Lagrangian velocity near the surface where the buoyancy forcing was greatest. We deployed between four and seven buoys on a total of seven occasions and received about 6–8 satellite fixes per day for each buoy, each with about 150 to 350 m radius of uncertainty.

The hydrographic surveys employed standard vertical CTD profiling along transects as well as an underway thermosalinograph. Fig. 1.1 shows the major transect locations. The thermosalinograph measured temperature and salinity from water pumped at a depth of about 0.5 m.

Supplementary data consist of freshwater discharge data from the U.S. Geological Survey for the Delaware and Hudson River, sea level data from the National Ocean Service from 10 coastal stations between Sandy Hook, NJ and Cape Hatteras, NC, and wind data from the National Climatic Data Center (see fig. 1.1 for locations). Satellite imagery of sea surface temperature complements the present data set on a larger scale.

CHAPTER 2: OBSERVATIONAL OVERVIEW

2.1 Introduction

The spatial and temporal variability of the subtidal flow and density fields on the shelves in the Mid-Atlantic Bight defies any clear, coherent, or comprehensive description and explanation. Therefore, I will first provide the observational background of simple ideas on the outflow of buoyant waters from the Delaware Estuary and the downstream coastal current on the shelf. Throughout this dissertation I will use the terms "downstream" and "upstream" always with reference to the direction of Kelvin wave phase propagation. This direction is to the south in the Mid-Atlantic Bight. In the following chapters I will then describe and analyze the flow and density field and their evolution in time in much detail. Here, I merely introduce the coastal current and state the main results. The coastal current undergoes dramatic along-shelf transitions and is frequently unstable.

2.2 Hydrography

In fig. 2.1 I redraw the horizontal and vertical distribution of salinity near the Delaware Estuary as Haskins (1954) reported it to the U.S.

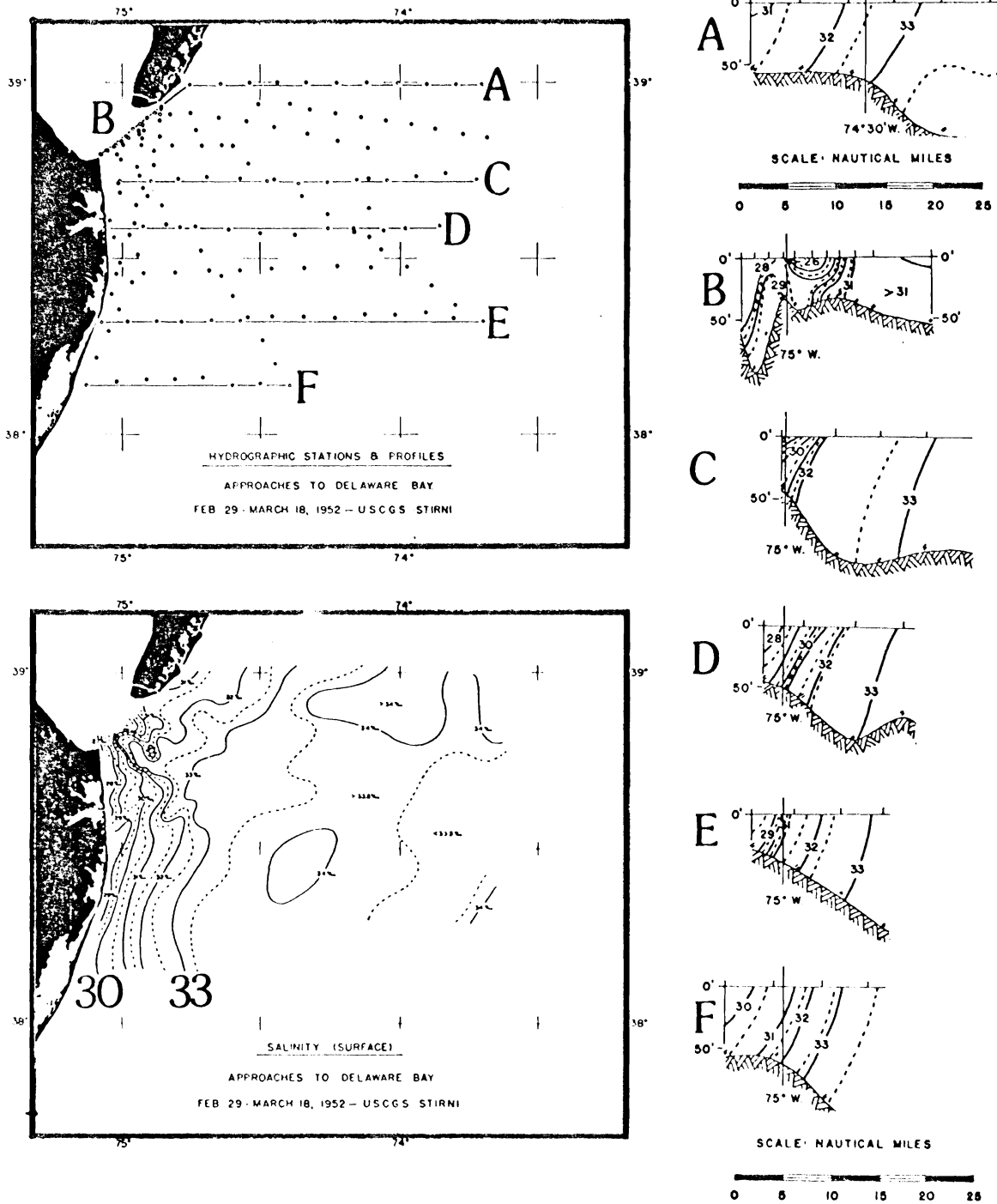


Figure 2.1. Salinity distribution in March 1952. Reproduced from Haskins (1954).

Navy. It took him almost 3 weeks to complete the survey in early March of 1952. I know now and discuss later that the salinity field changes within days; hence fig. 2.1 is severely aliased and should be interpreted qualitatively only. Nevertheless, the convoluted and banded structure of the light water along the Delaware and Maryland shores is the first recorded evidence of the coastal current. Horizontal gradients are larger downstream of the estuary as compared to those upstream. From the vertical transects across the shelf, I infer that a large salinity gradient at about 15 km from the coast separates buoyant inner shelf from ambient shelf waters. The buoyant waters inshore extend to the bottom and are thus subject to bottom friction. One could argue that this is merely due to wind stirring and thermal convection in winter, but while these are certainly contributing processes, I argue below that the shallowness of the water depth is all-important.

In fig. 2.2 I present results from a similar survey undertaken during the peak of the stratified season (June 12, 1990) with weak winds blowing. Again, an undulating low salinity band hugs the coast downstream of the mouth of the Delaware Estuary. Upstream we find almost uniform ambient shelf waters. Again, a zone of enhanced gradients separates buoyant inshore from ambient shelf waters, and again, the buoyant inner shelf waters extend to the bottom. Wong and Münchow (1991) discuss details of this survey which includes a description of the hydrography within the estuary.

Finally, fig. 2.3 depicts the local hydrography on May 24, 1989,

Salinity June 1990

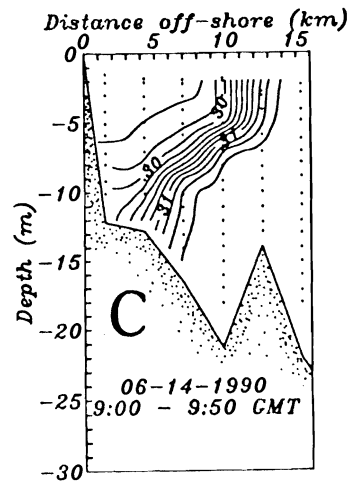
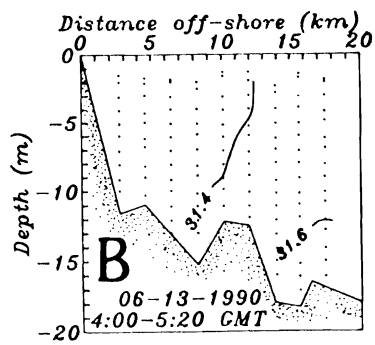
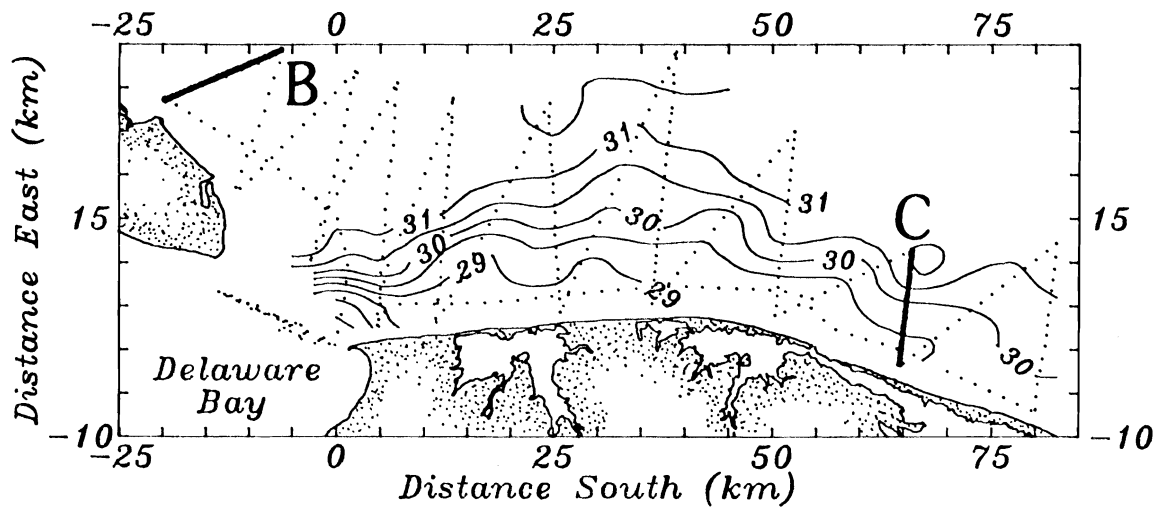


Figure 2.2. Salinity distribution in June 1990. Data from Wong and Münchow (1991). Note the absence of any stratification upstream of Delaware Bay (transect B) and the presence of a front downstream of Delaware Bay (transect C).

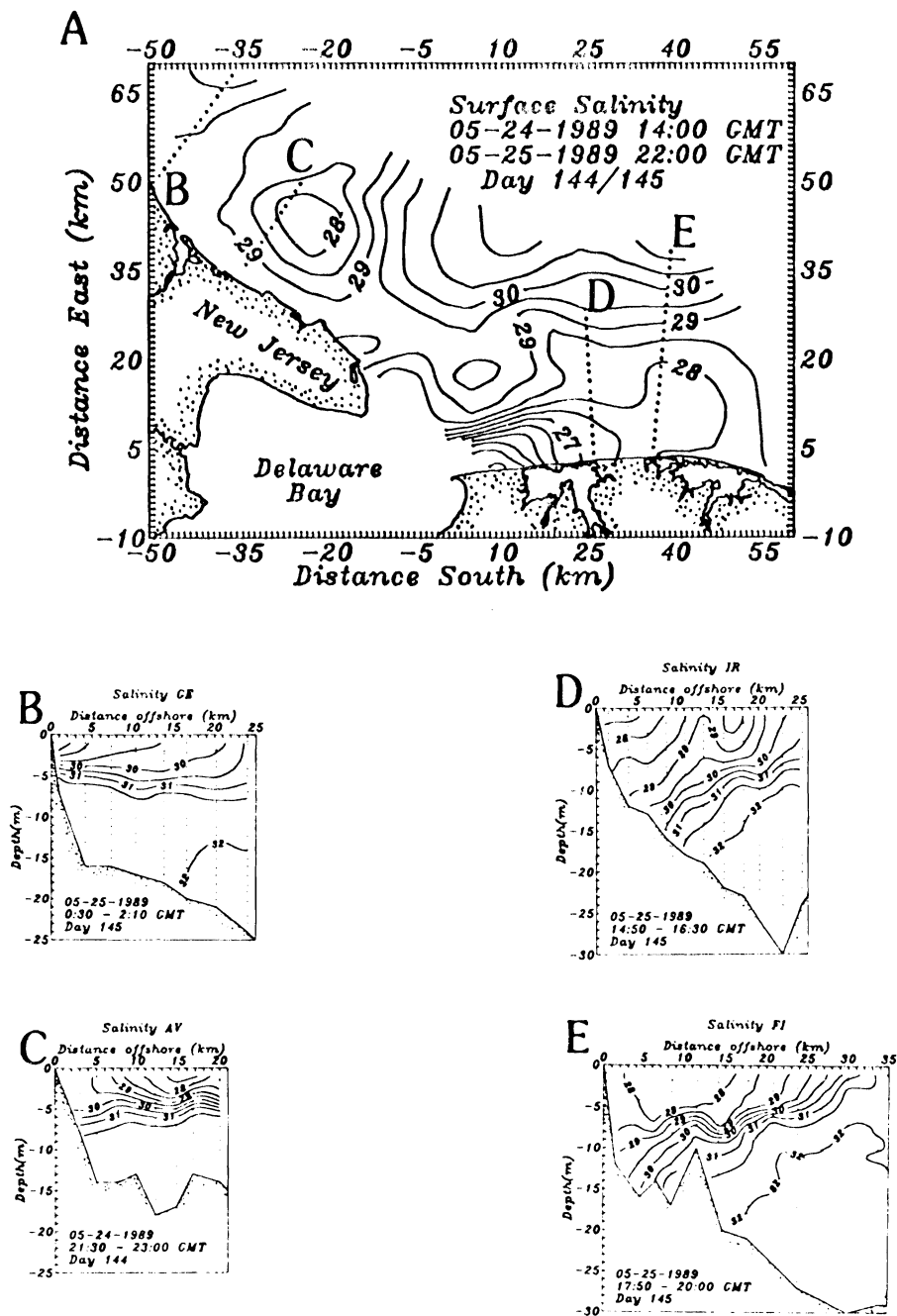


Figure 2.3. Salinity distribution in May 1989. Four transects are labeled B, C, D, and E on the map of surface salinity (A). Note the shallow eddy off the coast of New Jersey.

about 10 days after torrential rains whose floods killed three people in New Castle County, Delaware. The freshwater discharge rate of the Delaware River reached its annual peak well above $2000 \text{ m}^3/\text{s}$. On the shelf, again, we encounter complex structures throughout the study region. A circular pool of light water detaches from the coast of New Jersey, a front at the mouth of the estuary indicates the narrow outflow, several smaller eddies occur offshore where salinity gradients are largest, and the 28 psu salinity contour resembles the head of a gravity current. The vertical distribution of salinity during this event (fig. 2.3) is stratified off New Jersey, but partially mixed off the coasts of Delaware and Maryland. The large eddy upstream of Delaware Bay is only 5 m deep, but downstream the buoyant waters extend, again, to the bottom. These transects probably represent maximum vertical stratification of the coastal current during the year.

In this section I presented three examples of the hydrography on the shelf in the vicinity of Delaware Bay. None of them is typical; none of them is simple; all of them indicate light waters near the coast downstream from the estuary; all of them show buoyant waters extending to the bottom off Delaware. Next I will give an overview of the flow field on the inner shelf.

2.3 Tidal, Subtidal, and Mean Flow Fields

On the continental shelf of the Mid-Atlantic Bight tidal currents

contribute about half of the observed total current variance. The dominant tidal constituent is the principal lunar M_2 tide. Münchow et al. (1991a) analyzed a large current meter data set from moorings deployed on the shelf near the Delaware Estuary. Fig. 2.4 shows the principal axes of the tidal ellipses from that study. Tidal currents are weak off New Jersey and far offshore (<10 cm/s), strong over the deep channel at the mouth of the estuary (>80 cm/s), and of intermediate strength off Delaware and Maryland (~ 20 cm/s). Offshore and off New Jersey the major axes of the tidal currents cross isobaths, conforming with the model predictions of Battisti and Clarke (1982). Near the shore, in contrast, currents are dominantly along isobaths. Further details and discussion of the tidal velocity field the interested reader will find in Münchow et al. (1991a).

Subtidal currents in the study area are driven by local winds (Masse, 1988), along-shelf pressure gradients (Noble et al., 1983), tidal rectification (Münchow et al., 1991a), and buoyancy fluxes (Garvine, 1991). The Delaware Estuary introduces important perturbations of the flow field on the shelf through estuary-shelf interactions (Masse, 1990) which Pape and Garvine (1982) first investigated with drifters. In fig. 2.5a I show the principal axes after removing the mean and filtering out tidal and inertial motion. The axes are strongly polarized along isobaths. The currents on the major axis are between 7 and 11 cm/s with larger values offshore near the surface. The orientation of the major axis near the surface is about 9 degrees to the right relative to those near the bottom. Such a finding is consistent

M_2 Tidal Ellipses

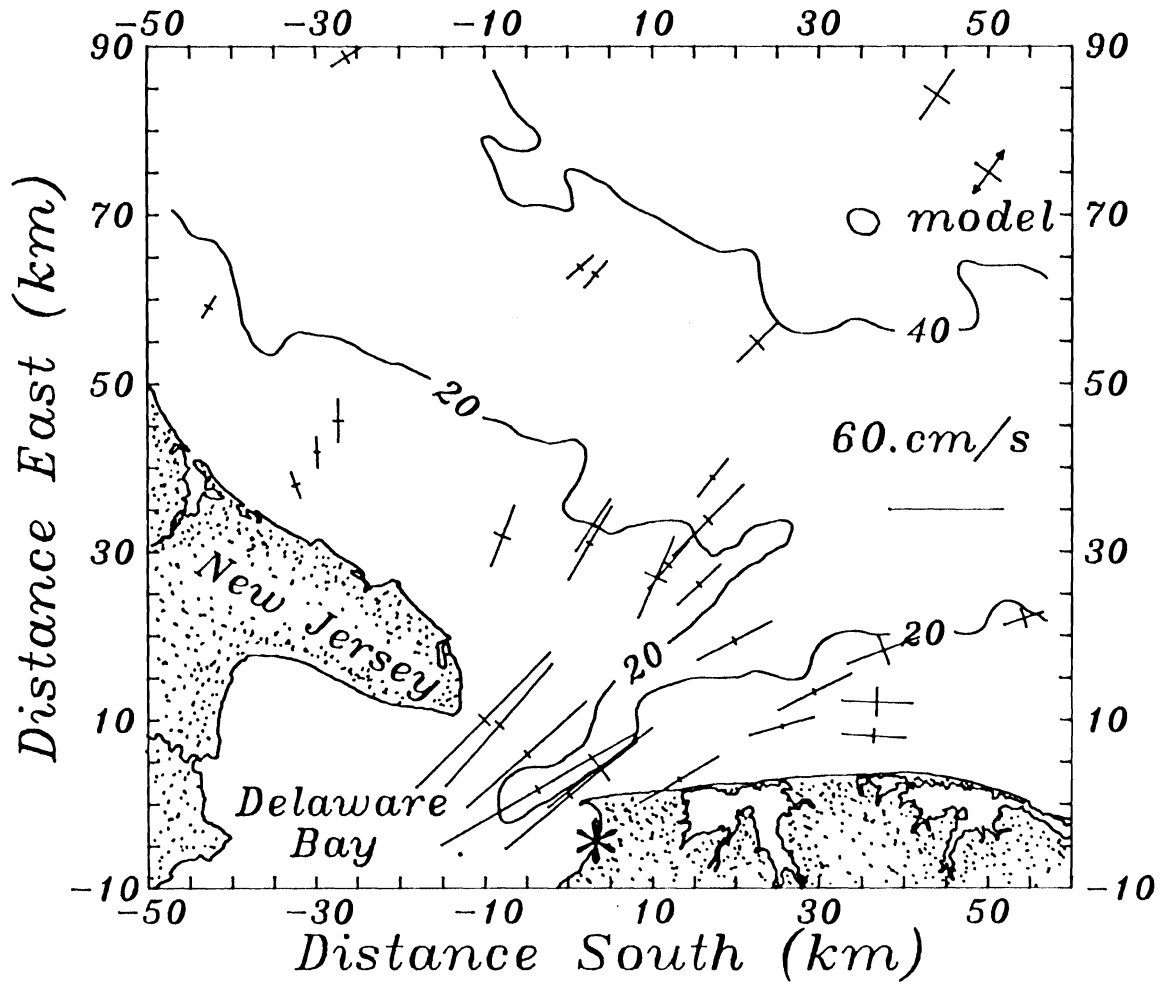


Figure 2.4. Map of principal axes of M_2 tidal currents. Reproduced from Münchow et al. (1991a).

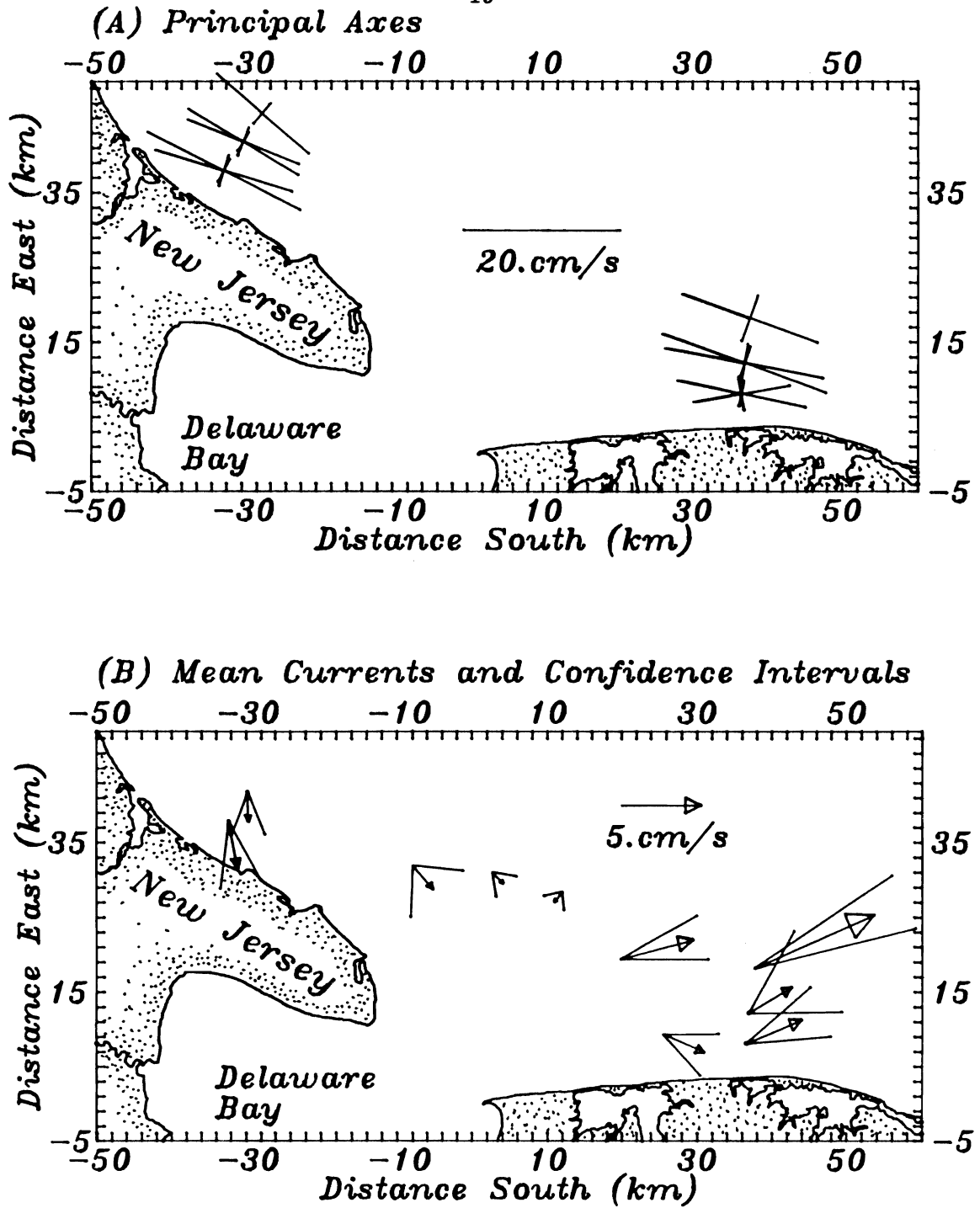


Figure 2.5. Subtidal currents from S4 current meters: (a) Principal axes for the deviation from the record mean; some locations show two pairs of axes. They represent data from bottom and surface current meters; (b) record mean currents and 95% confidence limits for speed and direction.

with frictional steering within a bottom Ekman layer. In chapter 4.5 I will investigate the vertical current structure within an Ekman layer that occupies most of the water column.

Mean currents are those at periods larger than the observational period. They are the most effective in transporting material in the coastal ocean and thus are always of prime interest. Garvine (1991) analyzed data from long term current meter moorings which he deployed in an arc around the mouth of the Delaware Estuary. The radius of that arc was about 30 km. In fig. 2.5b I show mean currents from that study along with those from this one. Upstream of the estuary mean currents are weak and directed either onshore or toward the estuary, while downstream they are strong and directed toward downstream. The latter flow indicates the Delaware Coastal Current. All error bars reflect 95% confidence limits for speed (Kundu and Allen, 1976) and direction (Mardia, 1972). Off Delaware I find a strong jet near the surface with maximum speed of about 8 cm/s. The current is strongly sheared, too, and reduces to about 4 cm/s next to the coast. In subsequent chapters I will indeed describe a coastal current whose core lies off the coast about 15 km.

In this section I introduced the flow field at different frequencies. The spatial variability emphasizes the complexity of the dynamics involved. The subtidal flow, however, appears to be controlled by friction, topography, and buoyancy forcing. Subtidal current speeds are about 10 cm/s and are

embedded in a dominantly semi-diurnal tidal velocity field of about equal strength.

2.4 Discussion, Scales, and Parameters

This dissertation will describe the formation of a buoyancy driven coastal current as observed with moored and shipboard instruments which electronically collect and digitally store huge amounts of data. In order to keep this dissertation concise, I will describe the coastal current in two successive steps. First I will always present selected aspects of the flow to make a clear observational statement. This statement I then transcend by computing nondimensional parameters that characterize all data. While the preceding sections of this chapter represent an example of the first step, this section is more typical for the second one. I define Rossby, Burger, Froude, and Ekman numbers, present their along-shore variability, and introduce three dynamically different regimes that are suggested by the parameters. A detailed discussion of each region will then be the subject of subsequent chapters.

I define three nondimensional parameters as ratios of different length scales. Each of these scales measures the influence of a physical process that contributes to the often complex flow and density field of the coastal current. The internal deformation radius I define as

$$L_D = N D / f$$

where N is the stability, buoyancy, or Brunt–Väisälä frequency, i.e.,

$$N^2 = - (g/\rho_0) \partial_z \rho$$

and D , f , and ρ are depth, Coriolis parameter, and density, respectively. The reference density ρ_0 I always take as 1025.5 kg/m^3 . The scale L_D represents the influence of vertical stratification on the horizontal circulation in a rotating system. A second length scale is the inertial radius L_i which depends upon a velocity scale U , i.e.,

$$L_i = U/f.$$

This scale represents nonlinear inertial forces. A third independent length scale of the coastal current is the distance L of buoyant waters from the coast. In an inviscid, linear, and steady system $L \sim L_D$ (Gill, 1976). Generally, however, the two scales may differ, as indeed they do in the present application. I speculate that frictional stresses widen the buoyant waters on the shelf and thus influence L .

All three length scales range between 2 and 30 km and are thus much smaller than the shelf width which is more than 100 km in the Mid–Atlantic Bight. This latter geometric scale is thus unimportant for the

dynamics of the coastal current. Another geometric scale, however, is potentially important. Submarine sand waves with scales $O(1 \text{ km})$ occasionally become comparable to one of the three dynamical scales that I introduced above. Oscillatory tidal currents over such topography generate a subtidal flow besides increasing vertical mixing (Zimmerman, 1980, 1986; Münchow et al., 1991a). Further, sand banks aligned parallel to the shore constitute locally enhanced bottom slopes reminiscent of a shelf break. Frequently I find large density gradients at locations where the bottom slopes are large. Small scale topographic features may thus influence or control the flow locally. Generally, however, sand banks are merely local features that I therefore neglect.

From the three horizontal length scales L_D , L_i , and L I define two nondimensional parameters, namely a Burger number S where

$$S = (L_D/L)^2$$

and a Rossby number ϵ where

$$\epsilon = L_i/L$$

while the internal Froude number F is then a function of S and ϵ , namely

$$F = \epsilon S^{-1/2} = L_i/L_D.$$

In the following I also use a second, independently determined estimate of the Rossby number. From transect data I first compute transverse current shears. These I then interpret as estimates of the relative vorticity ξ . The ratio ξ/f , where f is the Coriolis parameter (planetary vorticity), then constitutes an alternative measure of inertial to Coriolis forces, i.e., the Rossby number.

In a turbulent flow the Ekman layer depth δ_E and the water depth D define still another nondimensional parameter, namely the Ekman number E_v , where

$$E_v = (\delta_E/D)^2$$

and

$$\delta_E = (2A_v/f)^{1/2}$$

where A_v is a vertical eddy viscosity. I have then defined three independent parameters S , ϵ , and E_v which I use to describe the formation of a buoyancy driven coastal current. The along-shore variability of the former two parameters distinguishes different stages of the formation process that I summarize next.

The major result of this dissertation is fig. 2.6a. It depicts the along-shore variability of the coastal current in terms of the Burger

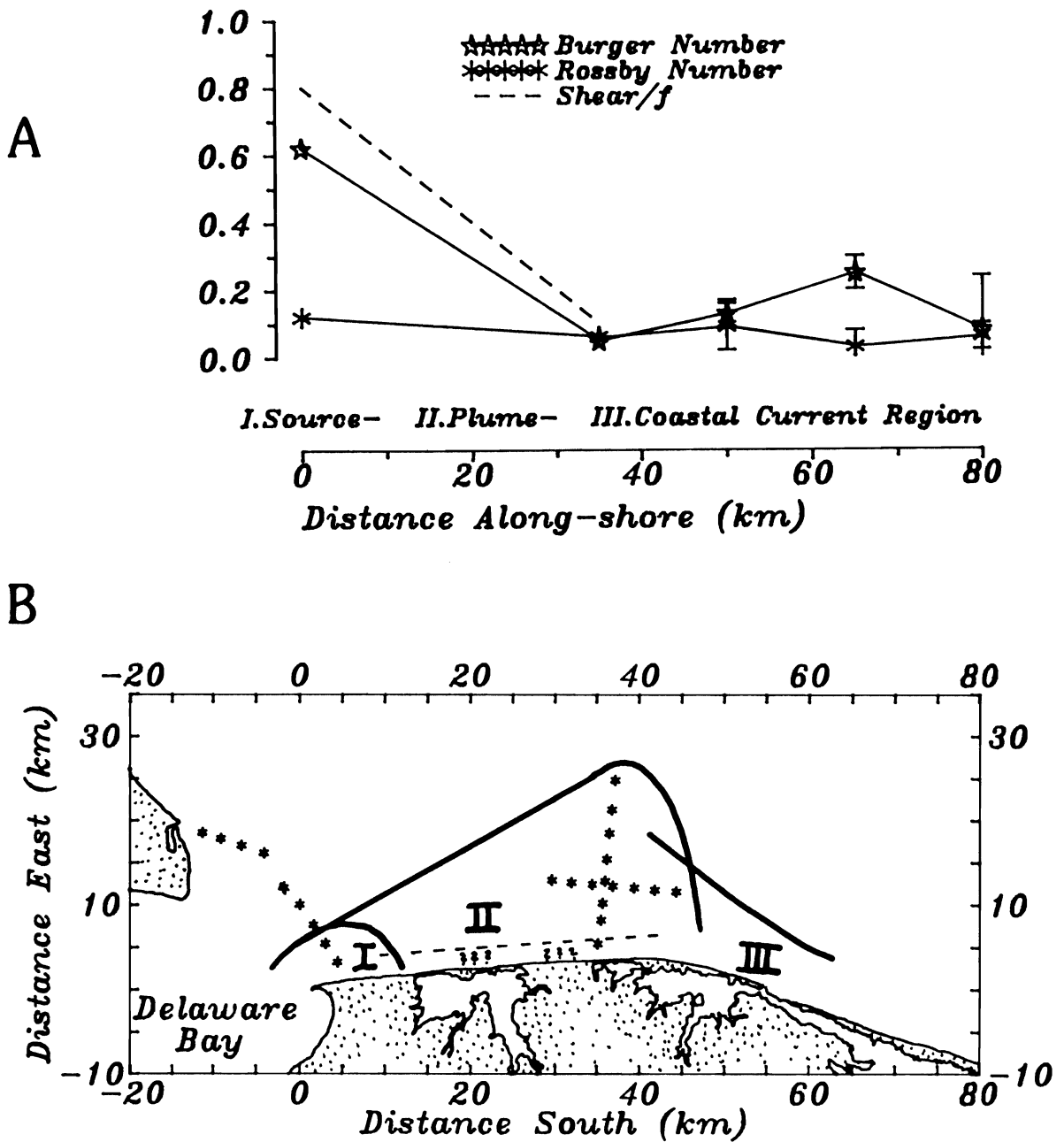


Figure 2.6. Parameters and sketch of dynamical regions. (a) Parameters of the Delaware Coastal Current and (b) conceptual sketch of the different regions). The stars in (b) represent major CTD and ADCP stations.

numbers, Rossby numbers, and vorticity ratios (labeled shear/ f in fig. 2.6) that I computed from all data. Each point in the diagram I will discuss in detail in subsequent chapters. Here, I merely point out that near the source of the coastal current (the mouth of the estuary) both the vorticity ratio and the Burger number are $O(1)$. This implies that the flow is nonlinear and that the width of the current scales well with the deformation radius. I speculate that friction is unimportant here. Downstream, both these parameters decrease and become much smaller than 1. This implies that the flow becomes linear and that either frictional or instability processes or both widen the coastal current beyond the deformation radius. Further downstream yet, all parameters settle to almost constant values. I interpret this as the region where the coastal current has finally formed. From fig. 2.6a I thus infer three different regions that I sketch in fig. 2.6b. The source region near the mouth of the estuary is the subject of chapter 3. The seaward flow there is nonlinear and exhibits strong frontal characteristics. A transition or plume region is evident about 20 km downstream from the source. The flow widens, loses its frontal character, and becomes linear. This region is the subject of chapter 4 which is the main chapter of this dissertation. Finally, the coastal current narrows again downstream and becomes uniform in its parameters along the shelf. This domain I call the "coastal current region," the subject of chapter 5.

CHAPTER 3: THE SOURCE REGION

3.1 Introduction

This chapter addresses the mouth of the Delaware Estuary between Cape May, NJ, and Cape Henlopen, DE, as the source of buoyant waters for the shelf. In fig. 3.1 I show the area both as a map with station locations (fig. 3.1a) and as an isometric projection of the bottom topography (fig. 3.1b). Two deep channels connect the estuary and the shelf near Delaware while shallow shoals separate them near New Jersey. This arrangement of channels and shoals impacts the distribution of water masses, fluxes, and vorticities profoundly. All these I discuss in this chapter. First, however, I introduce the frontal characteristics of the source region, as they dominate the density field, the flow field, the buoyancy fluxes, and the dynamics.

3.2 Fronts

After we recovered the last mooring shortly after dawn of the last day of the last experiment in June 1989, the R/V Cape Henlopen and a tired crew sailed to their home port in Lewes, DE. Nobody paid much attention to the oceanography anymore, even though shipboard instruments were still recording. Upon approaching the source region, however, we noticed sudden

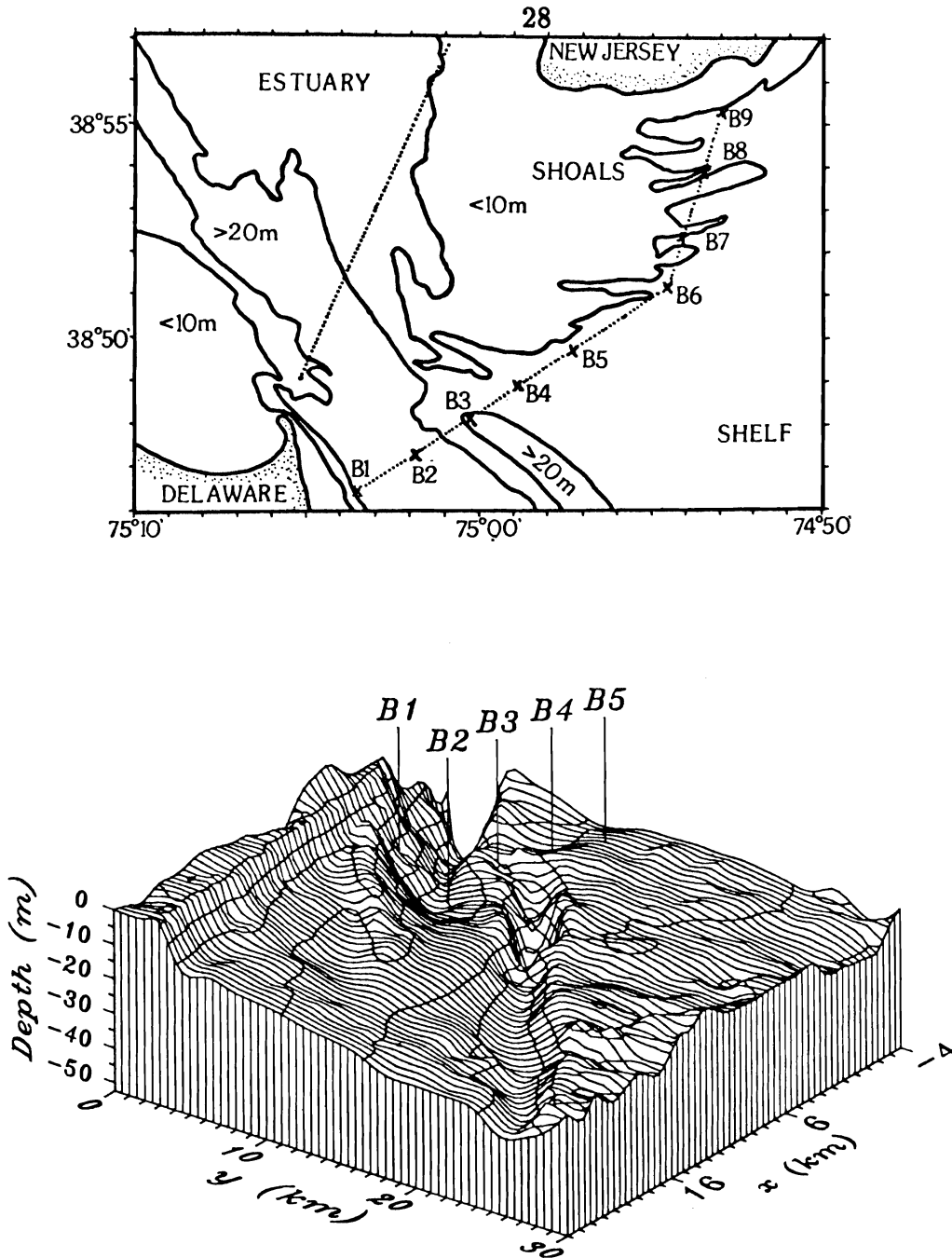


Figure 3.1. Bathymetry and stations of the source region: (a) Depth contours and transects across the mouth of the Delaware Estuary; note the deep channel that connects shelf and estuary near Delaware and the shoal that separates them near New Jersey; (b) isometric projection of bottom topography as seen from the shelf looking into the estuary, i.e., the view is from the shelf break to the North-West.

dense fog that disappeared just as suddenly 10 km later. While the thermosalinograph cannot record fog, it did measure the surface salinity and temperature of the water along the ship track. In fig. 3.2 I depict ship track, temperature, and salinity which shows that the ship sailed from warm into cold and back into warm water. We observed the fog where the water was cold. Apparently the water vapor content of the air condensed over cold water. Simpson and Pingree (1978) reported similar fog near fronts in the Celtic Sea, UK.

Fig. 3.2 thus documents a front that separates different water masses. The home-bound track began in ambient shelf waters that are both warm (18.5°C) and salty (31 psu) near the surface. Along the ship track water temperatures decrease to 15°C while salinities stay constant as the ship passes a tidal mixing zone near the shoals off New Jersey that Münchow et al. (1991a) discuss in much detail. Finally, we enter a third water mass, namely the buoyant outflow from the estuary. Both temperature and salinity change dramatically over small spatial scales. The 4 psu and 4°C change in salinity and temperature, respectively, implies a density difference of about 4.5 kg/m^3 over scales that are $O(100\text{m})$. The density field is then strongly frontal.

Another, equally dramatic example of frontal structures originates from two CTD transects less than 100 m apart which I took within 5 minutes of each other. Tidal currents have just turned from flood to ebb, i.e., the

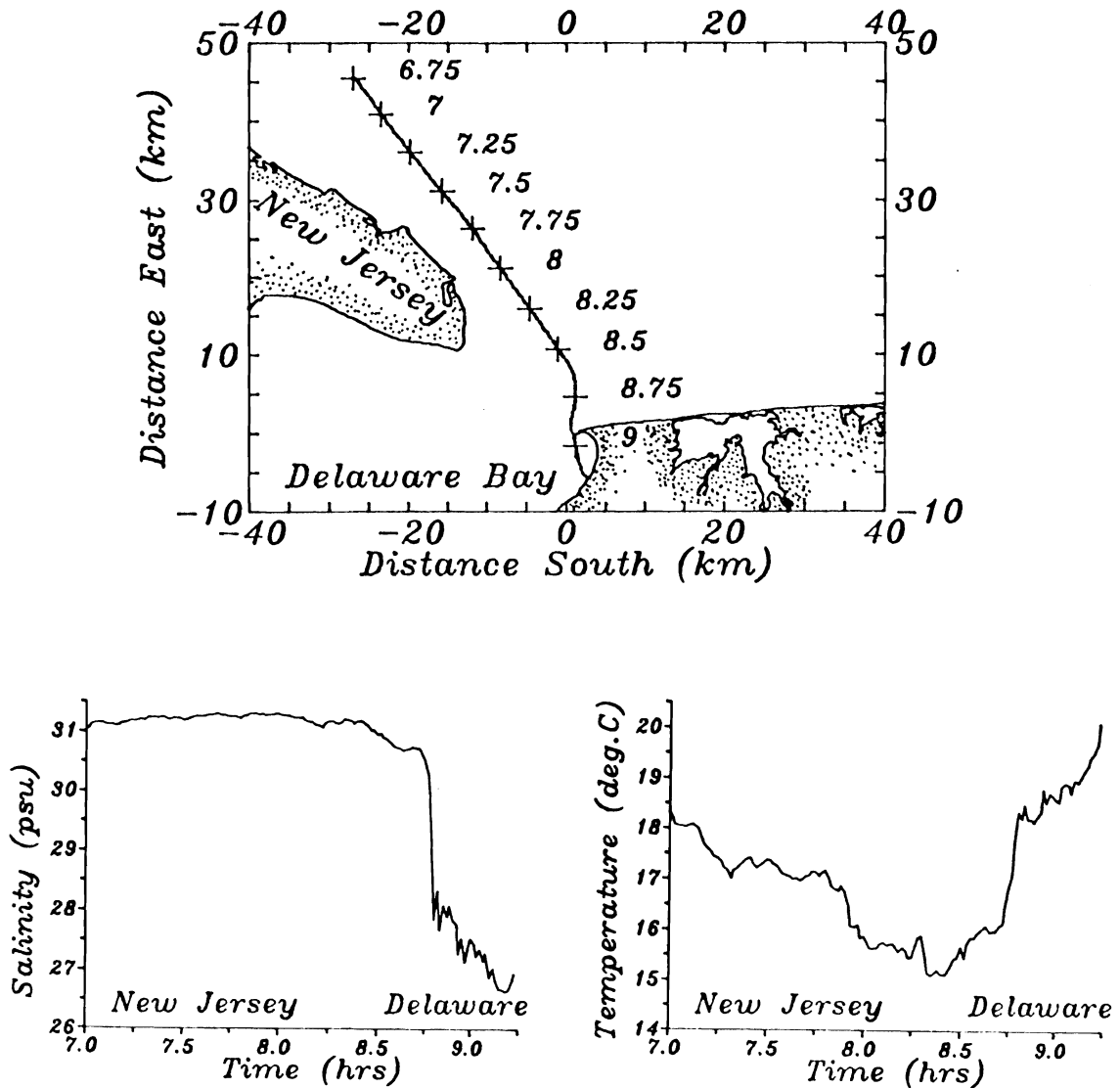


Figure 3.2. The front of the source region on 06-18-1989: (a) Ship track, labels indicate time of the day in hours EDT; (b) time series of salinity along the ship track; (c) time series of temperature along the ship track. The change of salinity and temperature at 8.75 hours represents a decrease in density by more than 4 kg/m^3 .

tidal phase is 210 degrees or 1 hour past local M_2 low water. Fig. 3.3 shows the two profiles which exhibit a surface salinity difference of more than 1.5 psu. These are frontal regions which we did not resolve since our station separation generally exceeded 2 km (see fig. 3.1). Also, computer generated maps interpolate data first onto a regular grid before drawing contours. This procedure further smooths out frontal structures.

As tidal currents influence the front that separates buoyant from ambient shelf waters, tidal and subtidal flows cannot easily be separated in a Lagrangian sense. Tidal currents may force a particle into the buoyant outflow which then will remove that particle from the source region permanently. Fig. 3.4 represents two drifters which sat in the "cold spot" for three days until one of them got a tidal kick into the coastal current. It never returned.

3.3 Water Masses

In the last section I suggested that in the source region fronts separate different water masses. To examine the mass field more systematically, I will now compare temperature–salinity (T–S) relationships for the estuary, the source region, and the shelf. Thereafter I discuss subtidal density data from two source region transects.

From Wong and Münchow (1991) I borrow two T–S diagrams from

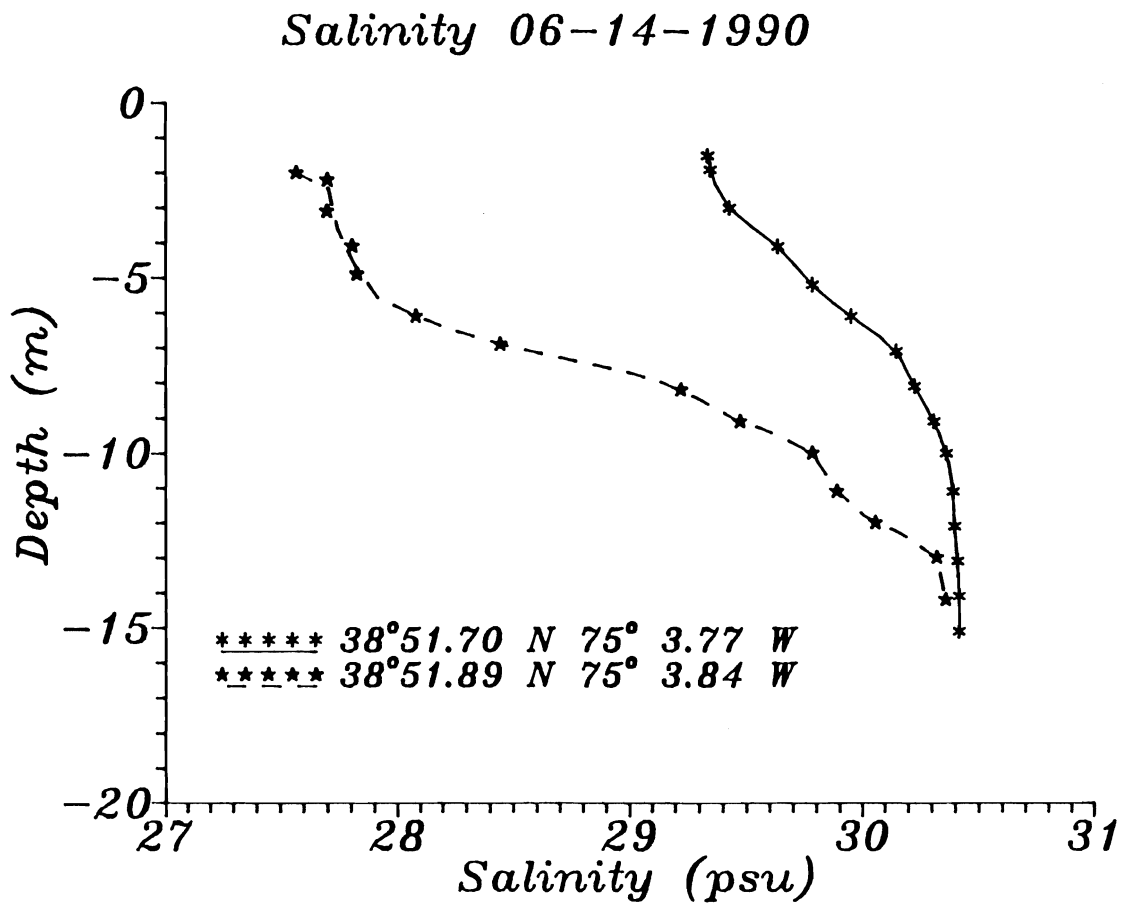


Figure 3.3. Two vertical salinity profiles near a front. The spatial and temporal separations are less than 100 m and 5 min., respectively. A tidally advected front separates the two different surface waters.

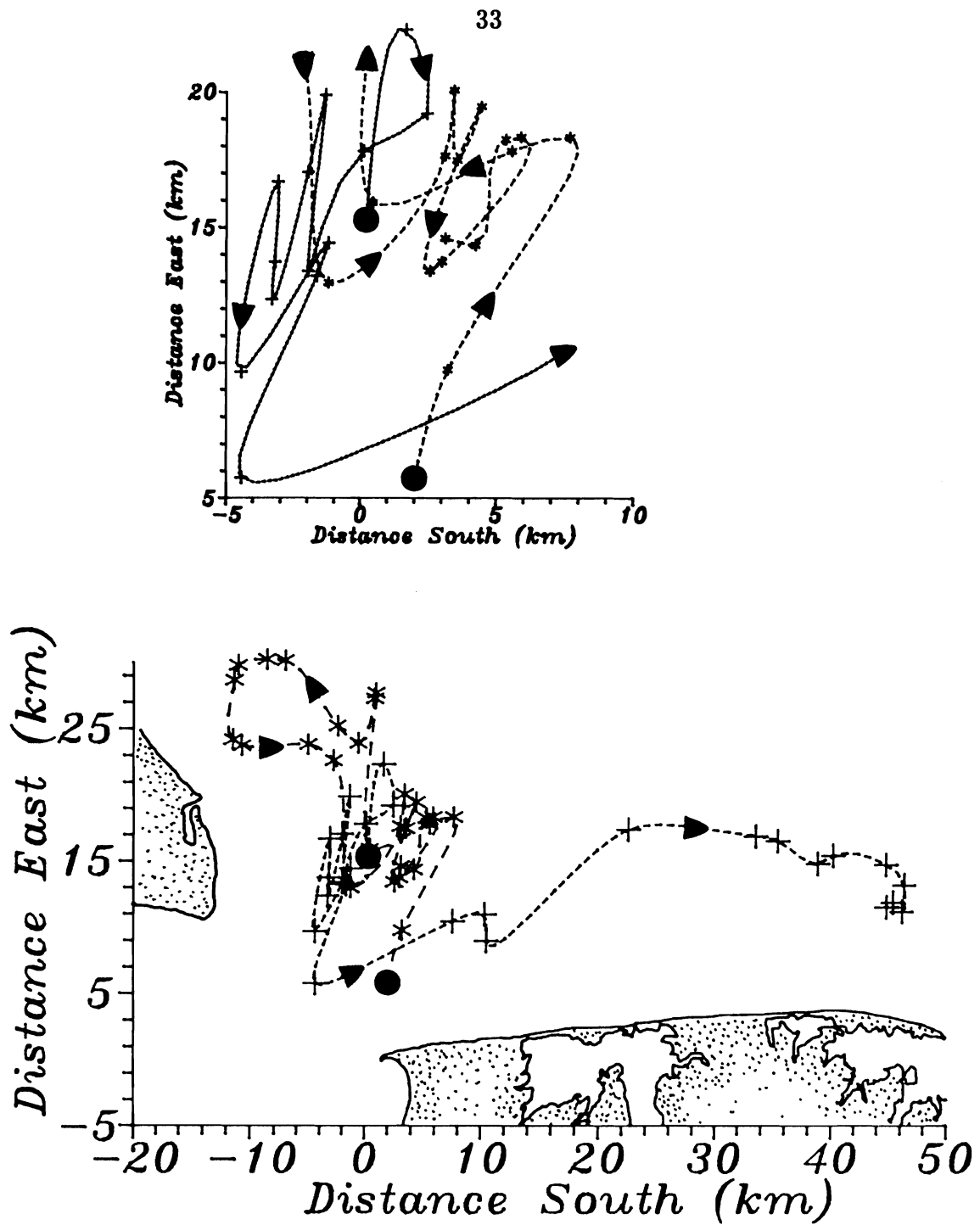


Figure 3.4. Two drifter trajectories in the source region. The ARGOS tracked drifter were deployed in the source region, the exact location I indicate by filled circles. We tracked the drifters for 4 days. The upper part is an enlargement of trajectories near the center of the mouth of the estuary. Different symbols represent satellite fixes for different buoys. The lines are spline interpolations to these fixes.

CTD data collected in June of 1990 and reproduce them in fig. 3.5. The data are from transects landward (figs. 3.5a and 3.5c) and seaward (figs. 3.5b and 3.5d) of the shoals that separate the estuary from the shelf near New Jersey. I select these as they appear particularly clear. On the shelf three distinct water types appear (fig. 3.5b), namely warm and fresh estuarine water ($T \sim 19^\circ \text{C}$, $S \sim 28 \text{ psu}$), cold and saline bottom shelf water ($T \sim 13^\circ \text{C}$, $S \sim 32 \text{ psu}$), and warm and saline surface shelf water ($T \sim 19^\circ \text{C}$, $S \sim 31 \text{ psu}$). Inside the estuary (fig. 3.5a) I find only two water types, namely warm and fresh estuarine water ($T \sim 20^\circ \text{C}$, $S \sim 25 \text{ psu}$) and cool shelf water ($T \sim 15.5^\circ \text{C}$, $S \sim 30.5 \text{ psu}$). It appears as if the latter water mass is a mixture of estuarine and bottom shelf water. Surface shelf waters then neither enter the estuary nor mix with estuarine waters. The data of figs. 3.5a and 3.5b, however, originate from single transects and are certainly aliased by tides (Wong and Münchow, 1991). Next, however, I present T-S diagrams from transects that we sampled over at least one tidal cycle to resolve the tidal signal properly.

I depict the T-S diagrams from two transects across the mouth of the Delaware Estuary (see fig. 3.1a, p.28, for station locations) in figs. 3.5c and 3.5d. Apart from the scatter that originates from tidal advection and mixing, the T-S relations are remarkably similar to those in fig. 3.5a and 3.5b. Again, landward of the shoals I distinguish only two water types, while seaward of the shoals I again find three. From this analysis one will thus anticipate that the subtidal density distribution of the two transects will

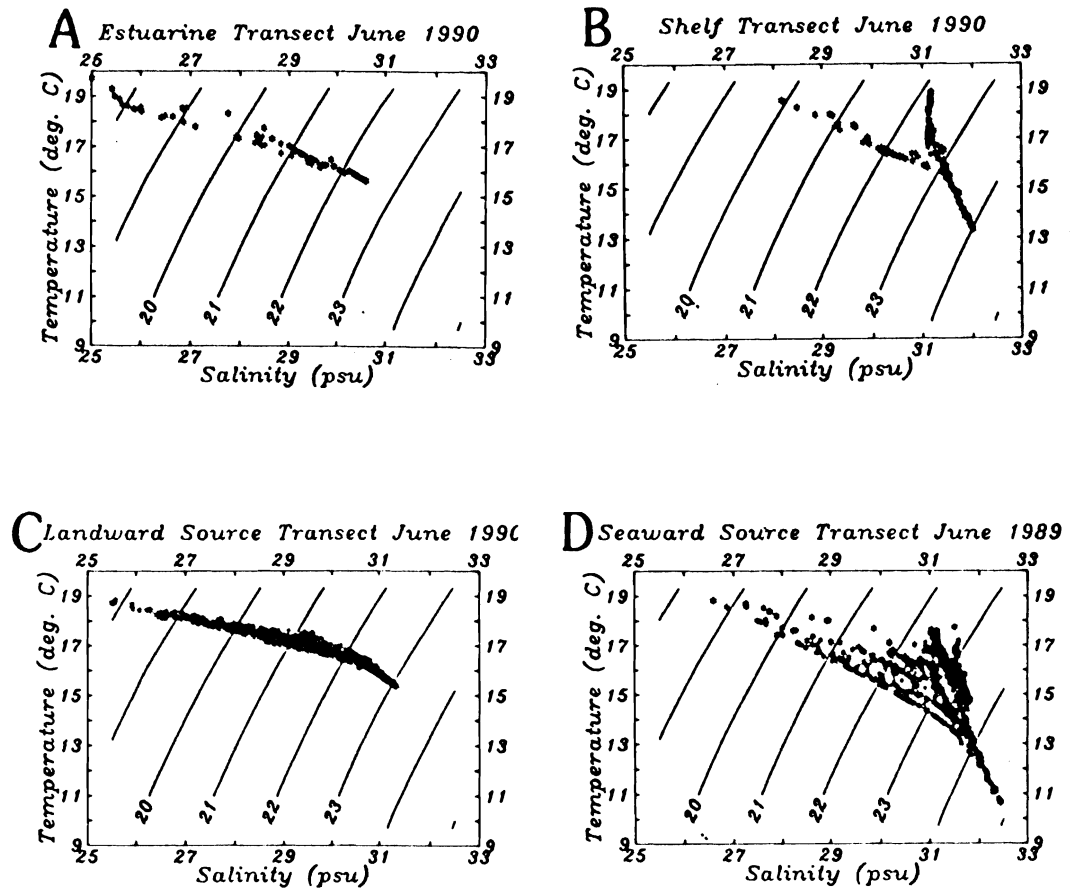


Figure 3.5. Temperature–Salinity diagrams: (a) Transect inside the estuary, 10 km landward of transect B ; (b) transect on the shelf, 5 km seaward of transect B; (c) transect CC (landward of the shoals); (d) transect B (seaward of the shoals). Only the data in (c) and (d) have been collected for at least a tidal cycle. See fig. 3.1 (p.28) for locations.

reflect estuarine conditions landward and shelf conditions seaward of the shoals, respectively.

Fig. 3.6 confirms this notion. It shows the subtidal density anomaly for all source region transects (see fig. 3.1, p.28, for locations). While the particular values of the densities shall not concern us here, the general pattern does. In figs. 3.6a, 3.6b, and 3.6c I show the subtidal density distribution for transect B for March, April, and June of 1989, respectively, while fig. 3.6d depicts that of transect CC in June of 1990. A seasonal signal emerges from March to June as the vertical stratification changes from winter to summer conditions. In June, however, the differences between transect B (fig. 3.6c) and CC (fig. 3.6d) are profound: upstream of the shoals fresher water is on both sides of the estuary, but seaward I find fresher water concentrated on the Delaware side only. The two transects are only 7 km apart, but the density stratification changes from the vertical to the horizontal. The seaward transition from one regime to the next is dramatic.

3.4 Flow Field Observations

Garvine (1991) and Münchow et al. (1991a) describe the flow field in the source region by analyzing data from moored current meters. Here I briefly summarize their results along with data from a shipboard ADCP. Processing details of the ADCP data one finds in Münchow et al. (1991b) and Wong and Münchow (1991).

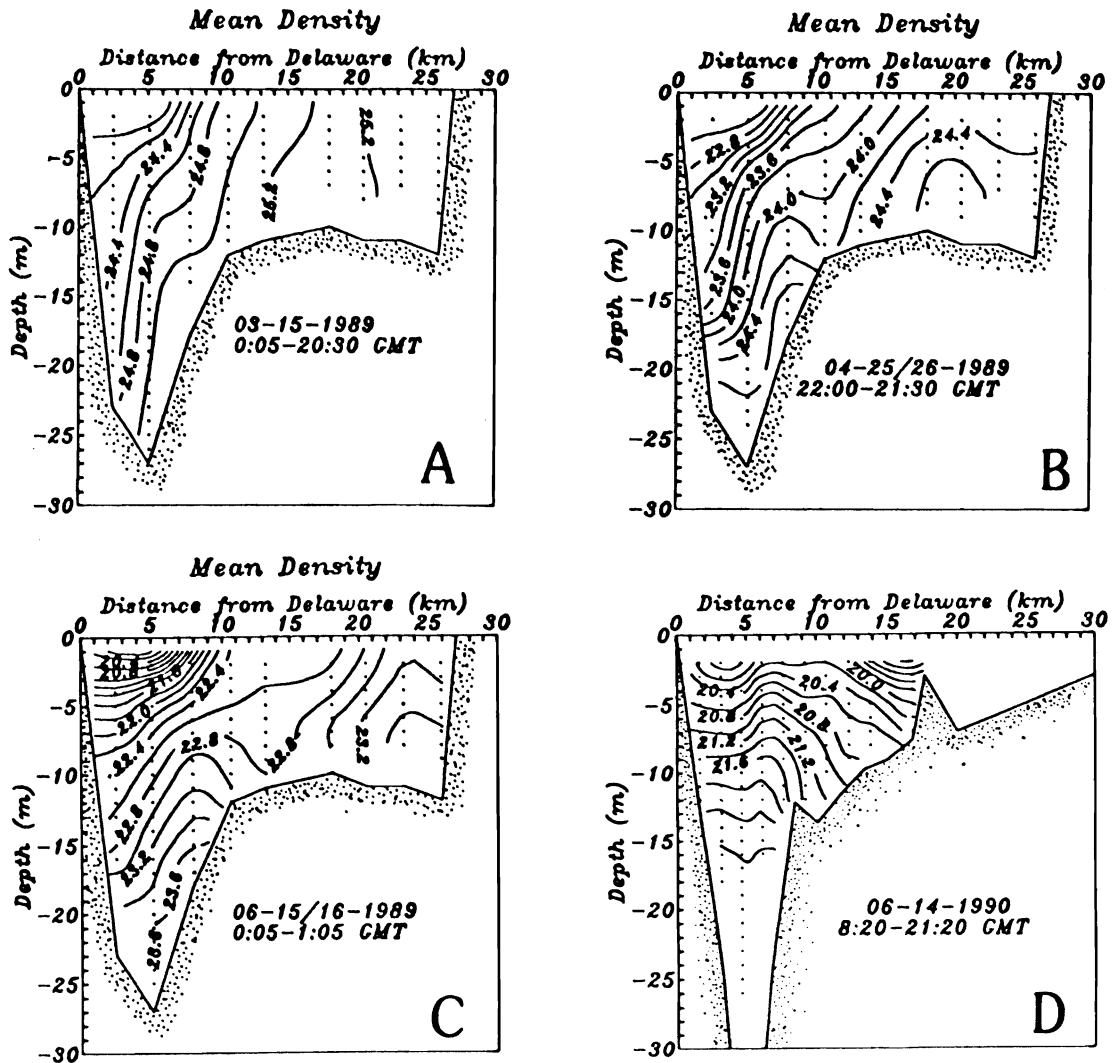


Figure 3.6. Subtidal transects of density anomaly. The transects are across the mouth of the estuary: (a) March 1989, transect B; (b) April 1989, transect B; (c) June 1989, transect B; (d) June 1990, transect CC. Note that only (d) shows light water on both sides of the estuary.

Tidal currents are almost rectilinear and decrease in amplitude from about 90 cm/s near the surface over the deep channel to less than 40 cm/s at depth and over the shoals (see fig. 3.1a, p.28, for station locations). Currents turn from ebb to flood about an hour earlier off New Jersey than they do over the deep channel. The horizontal distribution of M_2 tidal current ellipses near the surface (fig. 3.7) indicates that currents are directed along the estuary axis. Hence they cross isobaths over the shoals but follow them over the deep channel. Intense tidal mixing in the vertical over the shoals is thus a prime mechanism to maintain a vertically homogeneous water column there (Münchow et al., 1991a).

The horizontal distribution of vertically averaged subtidal currents, however, tells a very different story (fig. 3.8; see also Münchow et al., 1991b). In March, April, and June of 1989 I observe over the deep channel a seaward flowing jet with vertically averaged speeds of about 15 cm/s. Coincident with the region of large transverse density gradients (fig. 3.6b) is a region of large transverse current shear. A 10 cm/s landward flow lies beside a 15 cm/s seaward flow. Both mean inflow and outflow are affected by the topography, e.g., station B2 (outflow) is connected by a deep channel to the estuary, while station B3 (inflow) is connected by a deep channel to the shelf. A sand bank separates the two channels, and it is here that I often find the front separating shelf from estuarine waters. The inflow at station B3 (fig. 3.8) represents part of the seaward supply of the landward

*M₂ Tidal Ellipse from
ADCP Profiling
04-25/26 and 06-14/15-1989*

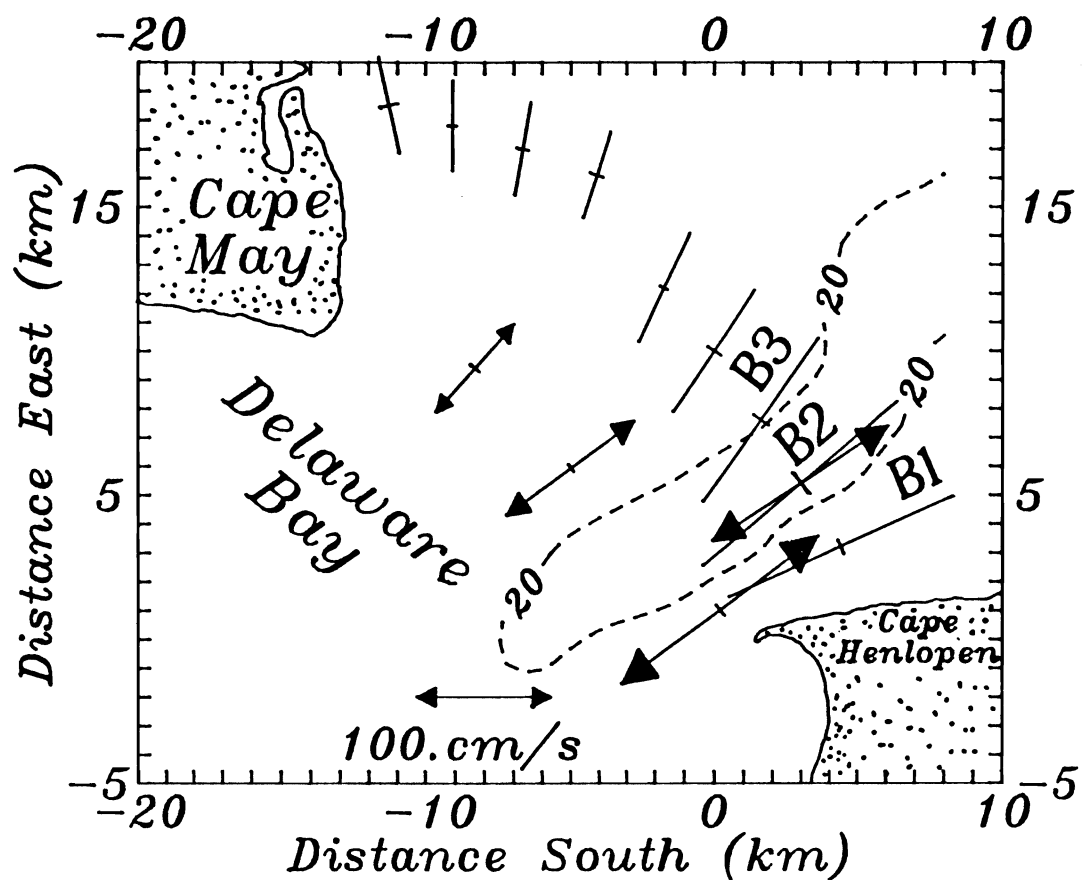


Figure 3.7. Principal axes for the M_2 surface currents. Data are from moored current meters (closed arrow heads) and ADCP profiling (from Münchow et al., 1991b).

*Depth Averaged Currents
from ADCP Profiling
04-25/26-1989*

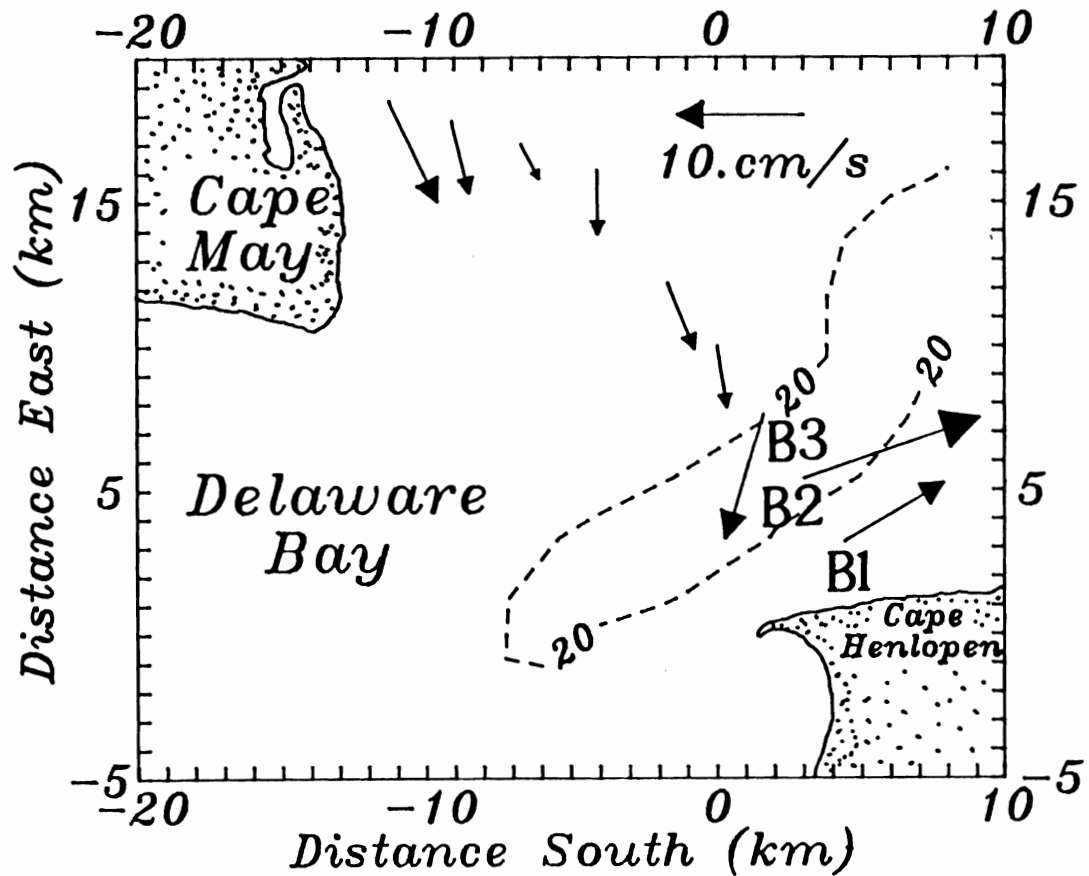


Figure 3.8. Subtidal currents from ADCP profiling. Depth averaged current vectors are from April 1989 (from Münchow et al., 1991b). Note the strong horizontal shear near the edge of the deep channel. It is there that I frequently observe the front (see fig. 3.2).

gravitational circulation (Pape and Garvine, 1982) while the outflow of fresher water at station B2 constitutes part of the buoyancy source for the coastal current on the shelf. Subtidal currents near the shoals are along isobaths and flow toward the deep channel (fig. 3.8). The fresher water landward of the shoals (fig. 3.6d) thus apparently crosses over toward the deep channel where it joins the seaward flowing source for the coastal current. Directly seaward of the shoals we observe fresher waters only once (Wong and Münchow, 1991) out of 6 experiments. Brackish, buoyant waters thus tend to exit the estuary on the shoreward side of the ancestral channel just off Delaware.

3.5 Buoyancy Fluxes

In order to estimate the buoyancy flux across a transect one needs a sufficient number of synoptic density and current measurements. Here I use data from our repeated CTD and ADCP transects. I will first estimate synoptic density and velocity distributions over transect B (see fig. 1.1, p. 8, for location) for a tidal and a subtidal signal. I will then compute, plot, and list the buoyancy fluxes at tidal and subtidal frequencies. In conclusion I will compare the buoyancy fluxes at the mouth of the estuary with those 35 km downstream (transect C, see fig. 1.1, p.8, for location) and find that the mean downstream buoyancy flux across the two transects agrees to within 30%. Hence most of the buoyancy which leaves the estuary will subsequently pass a transect downstream.

In order to quantify the buoyancy forcing which the estuary exerts on the inner shelf I will estimate buoyancy fluxes normal to transect B (see fig. 3.1, p.28, for locations). The horizontal buoyancy flux b_h per unit area is the reduced gravity of the fluid multiplied by the velocity component normal to the transect, i.e.,

$$b_h(y,z) = \frac{\rho_0 - \rho(y,z)}{\rho_0} g q_n(y,z)$$

where g is the gravitational acceleration, (y,z) are the lateral and vertical co-ordinates, while ρ is the density of the fluid. The reference density ρ_0 I take here as 1025.5 kg/m^3 , the density of ambient shelf waters (see fig. 3.5, p.35). The velocity component normal to the transect is q_n . The integral of this property over the transect area then gives the bulk buoyancy flux which measures the amount of forcing the shelf receives from the estuary. In the following positive fluxes are seaward while negative ones are landward.

For about 2 tidal cycles we collected density and velocity data with profiling instruments at the fixed stations of transect B. During 24 hours we completed a total of 8 transects which were always dominated by strong tidal currents that mix and advect estuarine and shelf waters. In order to estimate the synoptic distribution of density and velocity within the transect I fitted the following harmonic model to the data at each point in the transect:

$$\psi(y_i, z_j, t) = \psi_0(y_i, z_j) + \psi_1(y_i, z_j) \cos[\omega t + \theta(y_i, z_j)]$$

where ψ is a dependent variable representing density or a velocity component, (y_i, z_j) is a discrete point in the transect, and ω is the semi-diurnal M_2 tidal frequency. The model parameters are ψ_0 , ψ_1 , and θ to be determined from the data by the method of least squares. The subtidal variability I thus express by ψ_0 , and a tidal amplitude and phase by ψ_1 and θ , respectively. Münchow et al. (1991b) discuss this method when applied to ADCP data. Knowing the three model parameters I can then construct synoptic maps of density, velocity, and thus buoyancy flux at any time within the tidal cycle.

Fig. 3.9 compares the prediction of $\psi(y, z, t)$ against the data from which it has been derived. There I plot ρ , q_n , and b_h at a point over the deep channel 5 m below the surface as a function of time. Time, however, I refer to the stage of the first predicted M_2 high water in 1984 at the mouth of the Delaware Estuary. Zero phase then corresponds to M_2 high water. The dashed line represents the prediction of a variable for an experiment in June, while the solid line represents that for an experiment in April. The symbols are data points. The tidal amplitudes and phases of velocity in April and June (fig. 3.9b) do not compare well, but the respective deviations of the actual measurements from the fit are small (<10 cm/s). A second semi-diurnal constituent, which is not resolved here, is the most likely source of the discrepancy. The phase and amplitude of the density (fig. 3.9c), by

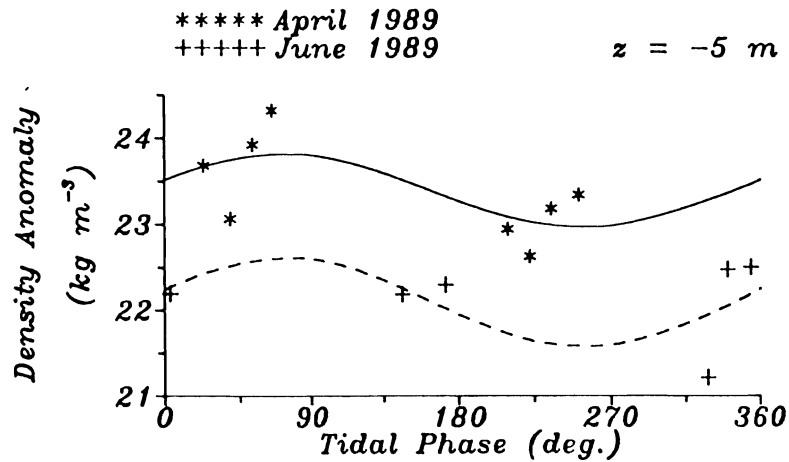
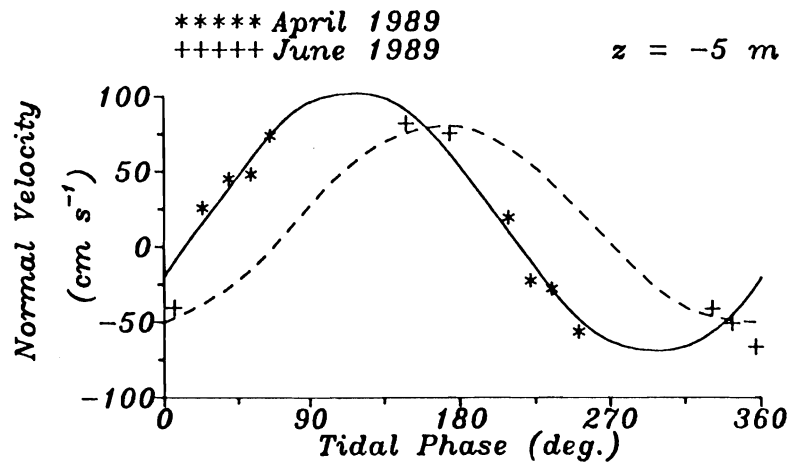
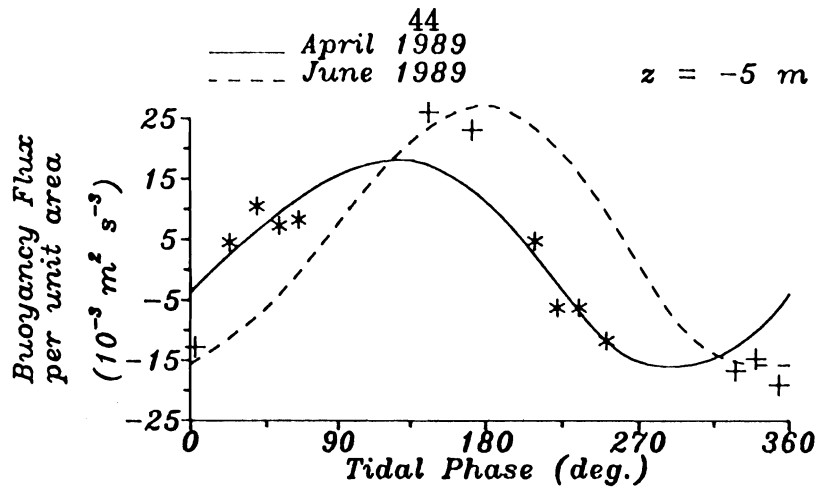


Figure 3.9. Tidal density, speed, and buoyancy fluxes at B2. I show properties through an M_2 tidal cycle 5 m below the surface. (a) Buoyancy flux per unit area; (b) speed along the channel; (c) density anomaly. Seaward is positive.

contrast, are very similar, but the scatter of the data can be as large as the tidal signal. The different "mean" density in April and June reflects different freshwater run off conditions in the two months.

Buoyancy fluxes (fig. 3.9a) reach about $25 \times 10^{-3} \text{ m}^4/\text{s}^3$ and occur just prior (April) and at the time (June) of local low water (phase of 180 degrees). Münchow et al. (1991b), however, argued that the phase estimation of velocity data is no better than about 20 degrees. For a discussion of the error estimation technique in least squares models I refer to Münchow et al. (1991a). In any case, data and least squares fit agree reasonably well and in the subsequent analysis I will use the subtidal signal ψ_0 only.

In fig. 3.10 I present the subtidal buoyancy flux per unit area for the April and June experiments. While the two experiments are 6 weeks apart and the absolute magnitude of the buoyancy fluxes are different, their spatial pattern is remarkably similar indeed. Over the deep channel buoyancy fluxes per unit area are seaward (positive) and reach $3 \times 10^{-3} \text{ m}^2/\text{s}^3$. Most notable, however, is the strong transverse gradient of the fluxes near both edges of the deep channel. Over the shoals fluxes are uniform, small, and landward. The main difference between the two transects is in the absolute magnitudes over the shoals. In April they are close to zero, but in June they are about $-1 \times 10^{-3} \text{ m}^2/\text{s}^3$. One will thus anticipate that the integral over the transect in April and June will reflect this difference also.

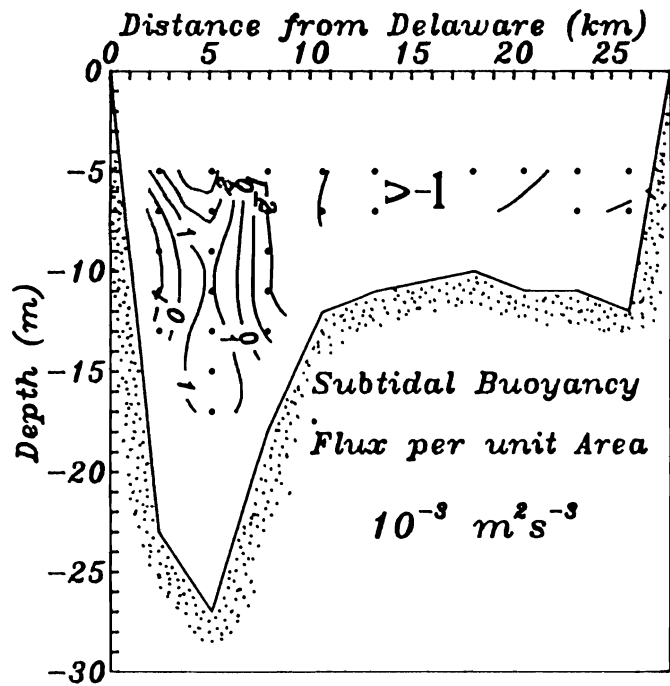
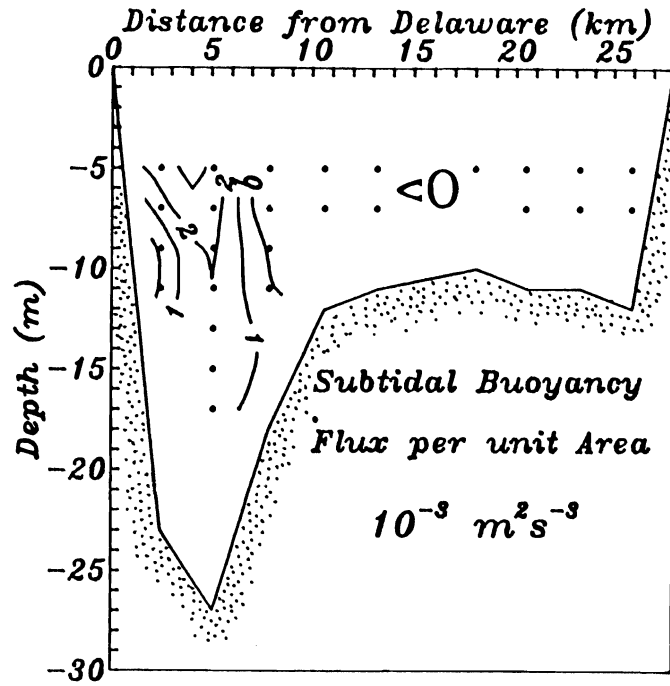


Figure 3.10. Subtidal buoyancy flux per unit area. Positive fluxes across transect B are positive. Data for (a) April 1989; and (b) June 1989.

In table 3.1 I list the net buoyancy flux which is indeed seaward and landward for April and June, respectively. I argue, however, that the circulation and water masses over the shoals are distinct from those over the deep channel. The waters over the shoals are ambient shelf waters from offshore. The waters over the channel, on the other hand, are buoyant waters from the estuary. A front (see fig. 3.6, p.37) separates the two water masses. In table 3.1 I thus list subtidal buoyancy fluxes separately for seaward and landward flowing waters. Now the seaward fluxes in April and June agree to within $50 \text{ m}^4/\text{s}^3$ or 50%.

The above estimates are order of magnitude estimates only. The ADCP does not measure currents near the surface or bottom. Therefore, the cross-sectional integral of b_h misses a substantial part of the entire transect, about 30%. I expect, however, that I under- rather than over-estimate the total buoyancy flux, as the estuary probably exports more buoyancy to the shelf near the surface than it imports from the shelf near the bottom.

For comparison, I also computed the fluxes of buoyancy across a shelf transect (fig. 3.11) about 35 km downstream from the mouth (see fig. 1.1 on p.8 for locations). In April the buoyancy flux to the shelf and downstream on the shelf are very similar, i.e. 110 and $70 \text{ m}^4/\text{s}^3$, respectively. In June, however, the agreement is less striking. Averaging the two downstream flux estimates from April and June together, the mean buoyancy flux on the shelf is about $115 \text{ m}^4/\text{s}^3$ (table 3.1) which compares well with the

Table 3.1. Subtidal buoyancy flux across transects. See fig. 1.1 (p.8) for locations. Time Δt refers to the time lag between the profiling of transect B and transect C. Positive fluxes are seaward. Units are (m^4/s^3)

Transect:	Total		Seaward		Landward		Time Δt (hrs)
	B	C	B	C	B	C	
April	70	60	110	70	40	10	40
June	-80	160	60	160	140	0	20
Mean	-5	110	85	115	90	5	

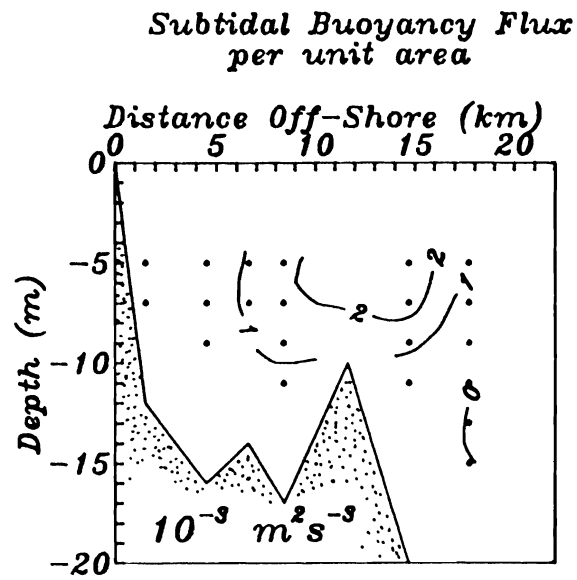
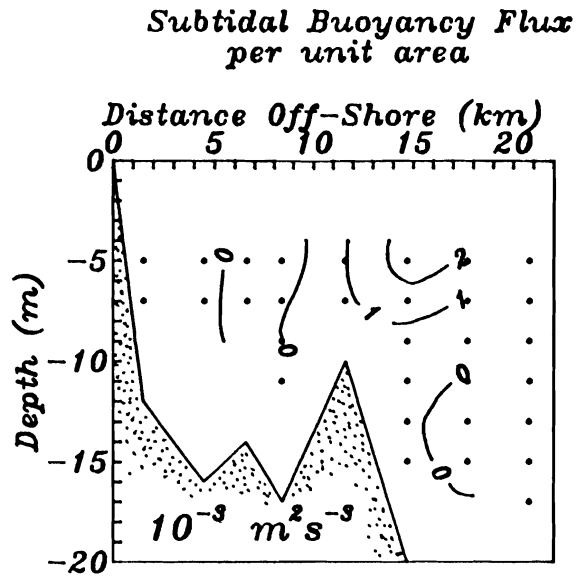


Figure 3.11. As for fig. 3.10, but for the shelf transect C. See fig. 1.1 (p.8) for locations.

$85 \text{ m}^4/\text{s}^3$ which exits the estuary. I thus conclude that the source and plume transects resolve the same buoyant waters which the coastal current transports downstream. This buoyancy flux drives the coastal current.

I explain the agreement in April as well as the disagreement in June with the time lag between profiling the transect at the mouth and downstream. We always profiled the mouth of the estuary first. The time lag, however, between the profiling of the two transects was 40 and 20 hours in April and June, respectively. Assume a particle which moves directly from the estuary to the downstream transect at a speed of 20 cm/s. This particle needs about 45 hours of transit time to reach the shelf transect 35 km downstream. From this simple scaling I conclude that in April we observe the same buoyant waters near the mouth and 35 km down-shelf, but in June we do not. Hence, I imply that the flux of buoyancy varies from one day to the next, most likely as a consequence of wind forced motions (Garvine, 1985). Winds were light ($< 1 \text{ m/s}$) in April while they were strong and upwelling favorable in June ($> 5 \text{ m/s}$).

In summary, the deep channel at the mouth of the Delaware Bay provides the site for the bulk of the subtidal buoyancy flux from the estuary to the shelf downstream. A subtidal flux of about $100 \text{ m}^4/\text{s}^3$ drives the coastal current on the shelf. The tidal modulation of this flux is an order of magnitude larger in the source region than it is 35 km downstream.

3.6 Dynamics

I diagnose the dynamics of the source region in three different ways. First, I test the hypothesis that the thermal wind balance holds, i.e., the flow along the channel is in geostrophic balance with the across-channel distribution of mass. As this particular balance fails to explain the observed current shear, I search for terms in the depth averaged across-channel momentum balance that could balance the dominant Coriolis acceleration. As only the baroclinic pressure gradient is large enough to balance the Coriolis force, however, I conclude that this term and the not measured across-channel pressure gradient of a sloping free surface balance the Coriolis force. The across-channel balance is then geostrophic. Finally, I present the vorticity distribution across the mouth of the estuary and find that relative and planetary vorticities are of the same order. The potential vorticity, however, is not uniform in the source region. All results are internally consistent if I assume a semi-geostrophic flow that is nonlinear and inertial along its axis but geostrophic perpendicular to it.

Before I enter the dynamical analysis I here define my co-ordinate system. It is always right handed and counts the vertical co-ordinate z positive up. Generally, I choose x in the direction of Kelvin wave phase propagation. In the estuary and at its mouth this definition is ambiguous. Hence I specify that x is normal to the transect B (see fig. 3.1a, p.28, for

location) counting the seaward direction as positive. The y co-ordinate then increases toward New Jersey.

An inviscid, geostrophic flow in balance with its mass field would allow me to compute its along-shore velocity component relative to some level from a density transect across the shelf alone. This diagnostic thermal wind balance I test here for the source region and later for the plume region. The geostrophic velocity due to the internal mass field is

$$u_g = \int_{z_0}^z \frac{g}{\rho f} \partial_y \rho dz + u_g(z_0).$$

At the reference level z_0 I have to prescribe the velocity and choose

$$u_g(z_0) = u_a(z_{\min})$$

where $z_0 = z_0(y)$ and u_a are the depth and velocity, respectively, of the ADCP bin closest to the bottom.

Here I study vertical current shears not currents and compare in fig. 3.12 the observed shear with that I obtain from thermal wind. The geostrophic shear varies only between 0 and $2 \times 10^{-2} \text{ s}^{-1}$ while the shear from the ADCP scatters between $-4 \times 10^{-2} \text{ s}^{-1}$ and $4 \times 10^{-2} \text{ s}^{-1}$. Most of the observed vertical shears are thus smaller than their geostrophic counter parts

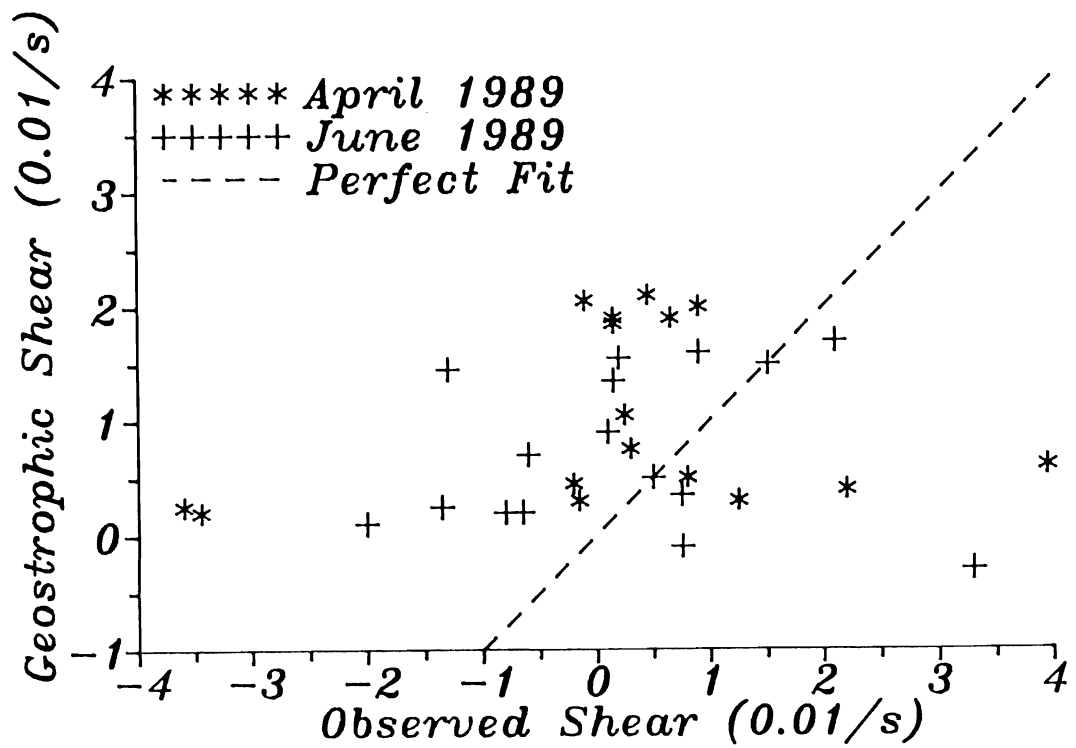


Figure 3.12. Observed vs. geostrophic vertical current shear. The observed current shears are from ADCP profiling, geostrophic shears originate from the thermal wind equation, and the dashed line represents the perfect fit.

(fig. 3.12). Indeed, Münchow et al. (1991b) find that the subtidal ADCP velocity field is vertically almost uniform. In contrast, geostrophy and the density field of fig. 3.6 (p.37) imply a vertically sheared current that I do not observe. Hence, the test of geostrophy from thermal wind is not conclusive. I cite as a first reason that the ADCP measures only the central part of the water column away from boundaries. Further, complex bottom topography and shallow water imply frictional forces that act upon the flow, too. And finally, at the mouth of the estuary the coastline bends by almost 90 degrees, and I therefore expect an inertial turning region there (Garvine, 1987).

Next, I will estimate the respective strength of such forces. The approach here is not to find an exact dynamical balance, but to obtain rough estimates of the magnitude of potentially important terms in the depth averaged across-channel momentum balance. I write the conservation of momentum across the channel as

$$\underbrace{\partial_t v}_{(a)} + \underbrace{u \partial_x v}_{(b)} + \underbrace{v \partial_y v}_{(c)} + \underbrace{fu}_{(d)} + \underbrace{g \partial_y \eta}_{(e)} + \underbrace{g/(\rho_0 H) \int_{-H}^0 \int_{z'}^0 \partial_y \rho \, dz dz'}_{(f)} - \underbrace{C_d v^2/H}_{(g)} +$$

$$\underbrace{\langle U \partial_x V \rangle}_{(h)} + \underbrace{\langle V \partial_y V \rangle}_{(i)} + \underbrace{\langle V \partial_t \eta_T \rangle/H}_{(j)} = 0$$

where (u,v) and (U,V) represent subtidal and tidal velocities, respectively, while η and η_T denote subtidal and tidal sea level perturbations. The terms are local acceleration (a), nonlinear advection (b,c), Coriolis acceleration (d),

barotropic (e) and baroclinic (f) pressure gradient, bottom friction (g), and tidal Reynold stresses (h,i,j). The bottom friction coefficient I take as 2.5×10^{-3} . With the data on hand I cannot estimate terms (a), (b), (e), or (h). All other terms I estimate from ADCP data, normalize each term with the Coriolis term (d), and average each estimate over the transect.

I list the size of different terms in table 3.2 and plot them with error bars in fig. 3.13. I compute the errors $\delta\psi$ of each term according to

$$\delta\psi(\alpha_i) = \left| \frac{\partial \psi}{\partial \alpha_i} \right| \delta\alpha_i,$$

where ψ is a term to be estimated and depends on measurements of the variable $\alpha_i \pm \delta\alpha_i$. This is clearly an upper bound of the error.

From table 3.2 and fig. 3.13a I infer that friction and nonlinear inertial forces are less than 10% of the Coriolis acceleration. They thus do not account for the failure of the thermal wind diagnostic which ignores both these terms. The two terms representing tidal rectification (Nihoul and Ronday, 1975) are larger than inertial and frictional forces, but they, too, are small relative to the Coriolis term. Münchow et al. (1991a) found that tidal rectification is an important process at the mouth of the estuary, as spatial gradients of tidal currents are large. The results, however, are only marginally significant as the error bars indicate. Only the baroclinic pressure gradient approaches the size of the Coriolis acceleration as the ratio of these

Table 3.2. Across-channel momentum balance. Absolute magnitude of terms in the across-channel momentum balance as estimated from CTD and ADCP data on transect B. All terms are scaled by the Coriolis acceleration. All symbols I explained in the text. I omitted the limits of the integrals of the baroclinic pressure gradient (term 3) in order to avoid clutter. In the text term numbers 2, 3, 4, 5, and 6 are referred to by the letters c, f, g, i, and j, respectively. The same term numbers are used in fig. 3.13 also.

	All	Channel	Shoals
	B1...B9	B1,B2,B3	B3,...,B9
Term 2 $v\partial_y v$	0.11±0.09	0.04±0.06	0.15±0.12
Term 3 $g/(\rho H)\iint \partial_y \rho dz dz'$	0.53	2.65	0.29
Term 4 $C_D v^2/H$	0.12±0.04	0.04±0.02	0.20±0.06
Term 5 $\langle V\partial_y V \rangle$	0.29±2.91	0.18±3.46	0.26±2.85
Term 6 $\langle V\partial_t \eta_T \rangle/H$	0.12±0.08	0.08±0.05	0.16±0.11

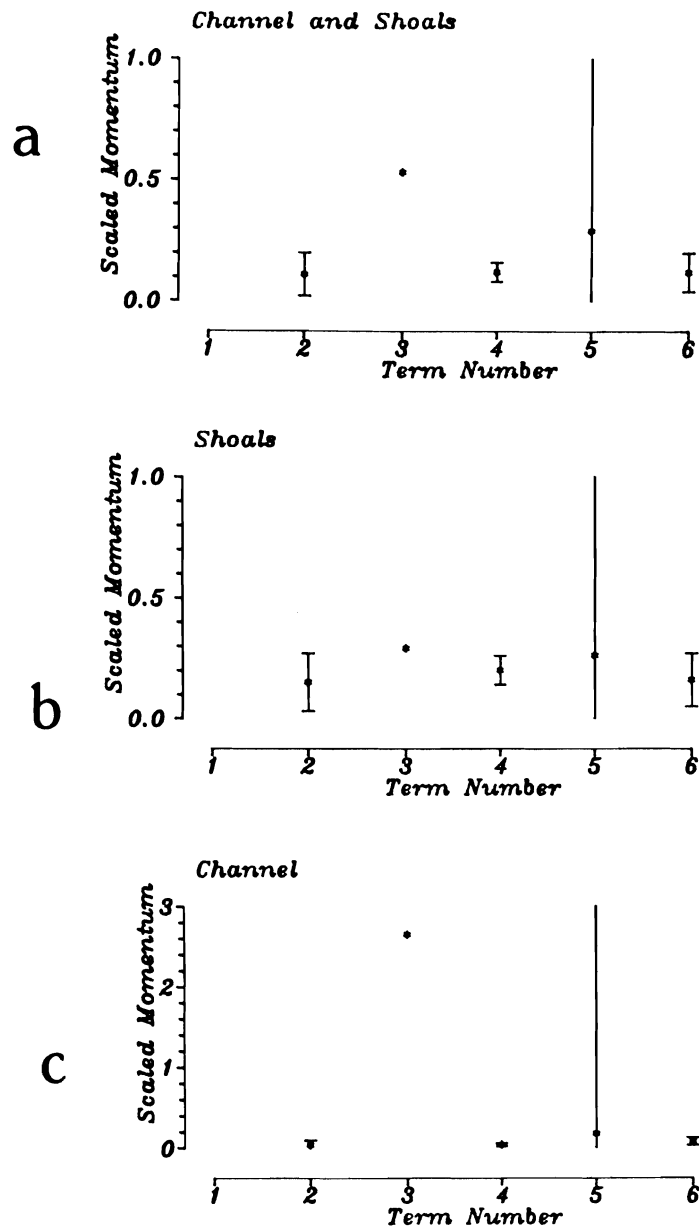


Figure 3.13. Subtidal momentum balance across the source region. Data from subtidal ADCP and CTD observations on transect B: (a) averages over all stations B1,B2,...,B9; (b) averages over station near the shoals only, i.e., B3,B4,...,B9; (c) averages over stations near the channel only, i.e., B1,B2,B3. Note the change in scale from (b) to (c) because of the dominance of term 3 (baroclinic pressure gradient) over the channel where the outflow is concentrated.

two terms is about 0.5. The pressure gradient due to the horizontal density gradient thus is a major term in across-shelf momentum balance at transect B.

As I discussed in section 3.2 a density front separates different water masses and flow regimes in the source region. I thus repeat the above analysis, but now interpret data from stations near the deep channel (B1, B2, and B3) as distinct from the data from stations near the shoals (B3, B4, etc.). For the location of stations I refer to fig. 3.1a (p.28). I present the estimates for each regime in figs. 3.13b and 3.13c (see also table 3.2). Over the shoals both bottom friction and nonlinear advection are sizable and tidal stresses contribute too (fig. 3.13b). Nevertheless, no single term alone balances the Coriolis acceleration in the across-channel momentum balance there. I thus conclude that near the shoals many terms contribute to the across-channel momentum balance. Over the deep channel, in contrast, the balance is nearly geostrophic. While both bottom friction and nonlinear advection are negligible, the baroclinic pressure gradient exceeds the Coriolis acceleration by a factor of 2.5. Hence a barotropic pressure gradient which I cannot measure is needed to oppose the large baroclinic pressure gradient. Hence I speculate on a three term balance over the deep channel: a sea surface slope and Coriolis acceleration act in concert to balance a large baroclinic pressure gradient. The outflow along the channel, I speculate, is then in geostrophic balance across the mouth of the estuary. Garrett and

Petrie (1981) find a similar balance across the Strait of Belle Isle, Canada. The same authors also review earlier related literature.

If nonlinear inertial forces were unimportant in both x and y directions, I would expect the relative vorticity $\partial_x v - \partial_y u$ to be much smaller than the planetary vorticity f (Pedlosky, 1986, p. 345). I assume $\partial_x v \ll \partial_y u$; therefore the lateral shear of the along-channel velocity measures the relative vorticity. In fig. 3.14 I plot the ratio of relative to planetary vorticity $\partial_y u/f$ as a function of y for both the April and the June experiment. Even though freshwater discharge rates are different, even though the bulk buoyancy and volume fluxes are in opposite directions, even though the winds over the shelf are weakly onshore and strongly alongshore for April and June, respectively, nevertheless, the distribution of lateral shear is nearly the same. The strong shear is thus a robust feature of the flow in the source region. At about 8 km from the Delaware coast the lateral shear is almost as large as the Coriolis parameter f , i.e., the relative vorticity is of the same order as planetary vorticity. I thus conclude that nonlinear inertial forces are an important part of the dynamics of the source region. As they are negligible in the across-shore momentum balance, I further conclude that they enter the along-channel momentum balance only.

The success of the relative vorticity estimation warrants further investigation such as how the potential vorticity is distributed in space. Many analytical and numerical models require ad hoc assumptions on the

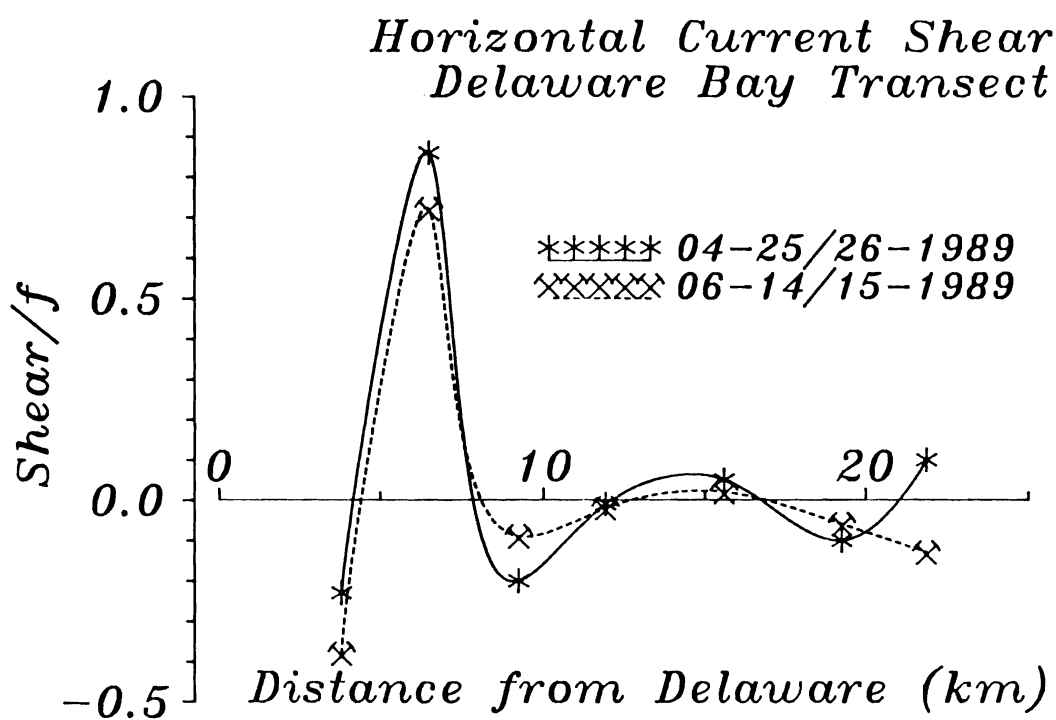


Figure 3.14. Horizontal current shear across transect B. I show data from both April and June 1989. The shear is scaled by the planetary vorticity (Coriolis parameter) f .

distribution of potential vorticity. Here I just mention two. Modeling channel flows, Whitehead (1989) assumes a reservoir of constant potential vorticity. The model correctly predicts the horizontal density differences and the position of a front at the mouth of the Chesapeake Bay. Powerful numerical tools such as contour dynamics (Stern and Pratt, 1985; Stern, 1989; Send, 1989) crucially depend on the assumption of locally homogeneous regions of potential vorticity in barotropic flows. With my estimation of potential vorticity I test if the above models can be applied to the outflow from the Delaware Estuary. As I demonstrate next, they cannot.

The potential vorticity or angular momentum of the fluid at a location y I define as

$$\Pi(y) = (\xi(y)+f) \partial_z \rho(y) / \rho_0.$$

The relative vorticity ξ I approximate as $-\partial_y u$ while I estimate the vertical density gradient $\partial_z \rho$ from a linear least squares fit to vertical density profiles from CTD casts. In fig. 3.15 I then present the distribution of potential vorticity across the source region. At each station I averaged the results from the experiments in March, April, and June together. This mean $\bar{\Pi}$ and the standard deviation $\sigma = (\Pi - \bar{\Pi}) / (n-1)$ I show as the solid curve and the error bars in fig. 3.15, respectively. The number of samples "n" is three. The mean potential vorticity varies considerably across the mouth of the estuary, and especially within 10 km from the Delaware coast. The frontal

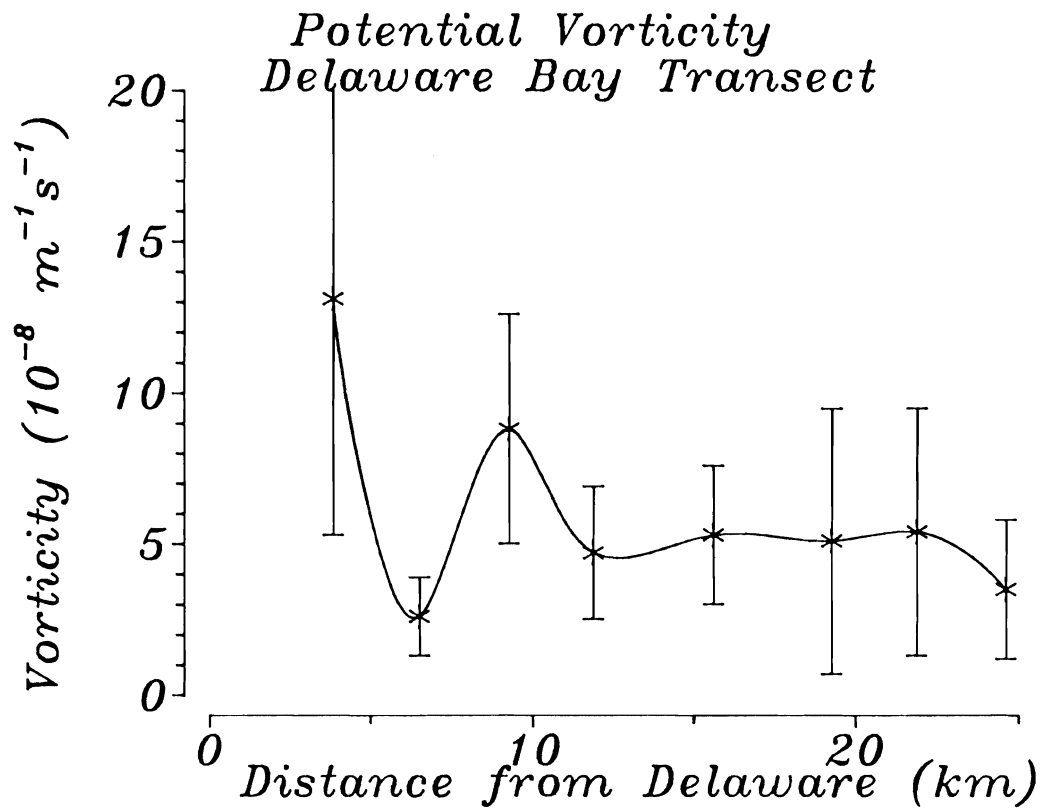


Figure 3.15. Potential vorticity across transect B. The symbols represent the mean value from the March, April, and June 1989 experiments. Error bars represent one standard deviation from the mean.

character of the source region shows here as the minimum of potential vorticity which coincides with the minimum of relative vorticity (maximum shear). Note, that the error bars are smallest at this location, i.e., the magnitude of potential vorticity at $y=6$ km is almost the same in March, April, and June. As the potential vorticity exhibits this minimum so consistently, I conclude that one may not apply uniform potential vorticity models to the outflow from the source region. A piecewise uniform potential vorticity model, however, may be applicable.

3.7 Discussion, Scales, and Parameters

In the source region a sharp front frequently separates buoyant estuarine and ambient shelf waters. I identified both an outflow channel that guides the seaward transport of estuarine waters onto the shelf and an inflow channel that guides the landward transport of bottom shelf waters toward the estuary. The width of the mouth of the estuary exceeds the internal deformation radius L_D by a factor of three and the buoyant outflow separates from one coast. The outflow lies beside, not above, the inflow. A surface front between the inflow and outflow thus separates different regimes. Every variable that I studied in this chapter reflected the frontal character of the source region. I analyzed the density and flow fields, the buoyancy fluxes, and relative as well as potential vorticities. Always the region near the deep channel is distinct from those near the shoals.

As I will discuss in the next chapter, the front weakens in the downstream (seaward) direction. The next region I term the "plume region" and the front there transforms into a region of enhanced gradients. The main difference between the source and plume region is the scale associated with the large horizontal property gradients. In the source region the frontal scale is about 100 m and is much smaller than any of the other length scales of the motion. The width L of the buoyant outflow I estimate from density transect data such as that of fig. 3.6 (p.37). During each of our three experiments L reached about 8 km. This scale matches the internal deformation radius L_D well and the Burger number S is then $O(1)$. The inertial radius $L_i=U/f$, however, is smaller than L and the Rossby number ϵ calculated from the velocity scale of the outflow then becomes 0.15. The source region is a frontal region, however, and the velocity shear across the front, which approximates the relative vorticity, provides a better estimate of the nonlinearity of the flow. The measured ratio of relative to planetary vorticity is $O(1)$ in the source region. This implies that both rotation and nonlinear advection are important. Finally, I find Froude numbers that are always smaller than 1, i.e., the flow is always subcritical. Hence the model of Garvine (1987) does not apply here as it requires an inviscid, steady, and supercritical flow. All the above scales and parameters I list in table 3.3.

In summary I conclude that fronts, rotation, and nonlinear inertial forces all affect the dynamics of the source region. I speculate that the across-channel balance is nevertheless geostrophic, as a baroclinic pressure

Table 3.3. Scales and parameters for the source region.

	March	April	June	Mean
L_D (km)	4.4	6.3	7.3	6.2
L_i (km)	0.8	1.1	1.0	1.0
L (km)	8.0	8.0	8.0	8.0
S	0.30	0.64	0.93	0.62
F	0.17	0.17	0.13	0.16
ϵ	0.09	0.14	0.13	0.12
ξ/f	0.5	0.9	0.7	0.7
Discharge (m^3/s)	150	350	700	400
Wind (m/s)	3	1	5	

gradient may balance a free surface slope and the Coriolis acceleration of the along-channel flow. Nonlinear inertial forces then enter the along-channel momentum balance only. The distribution of potential vorticity across the buoyant outflow is not uniform.

CHAPTER 4: THE PLUME REGION

4.1 Introduction

We studied the plume region downstream of the source region during four separate experiments in 1989 and two in 1990. The temporal and spatial variability is immense and at times it seems naive to ascribe any simplifying or conceptual characteristics to the plume region. In the mean, however, the flow is downstream in the direction of Kelvin wave phase propagation. Principal axes of subtidal variability are closely aligned with the local topography (see fig. 2.5, p.19). The width of the current increases from one to several internal deformation radii in the downstream direction away from the source. The plume waters generally extend from the surface to the bottom, though in June I observed the plume detaching from the bottom as it responded to strong upwelling favorable winds. Fronts in the plume region are often weaker than they are in the source region, but large horizontal velocity and density gradients persist. Meanders and eddies, however, disrupt the plume region frequently.

In Fig. 4.1 I depict the wind, discharge, and surface current time series for a 3 month period from March to June 1989. For the ease of viewing I applied a Lanczos low-pass filter with a cut-off period near 5 days

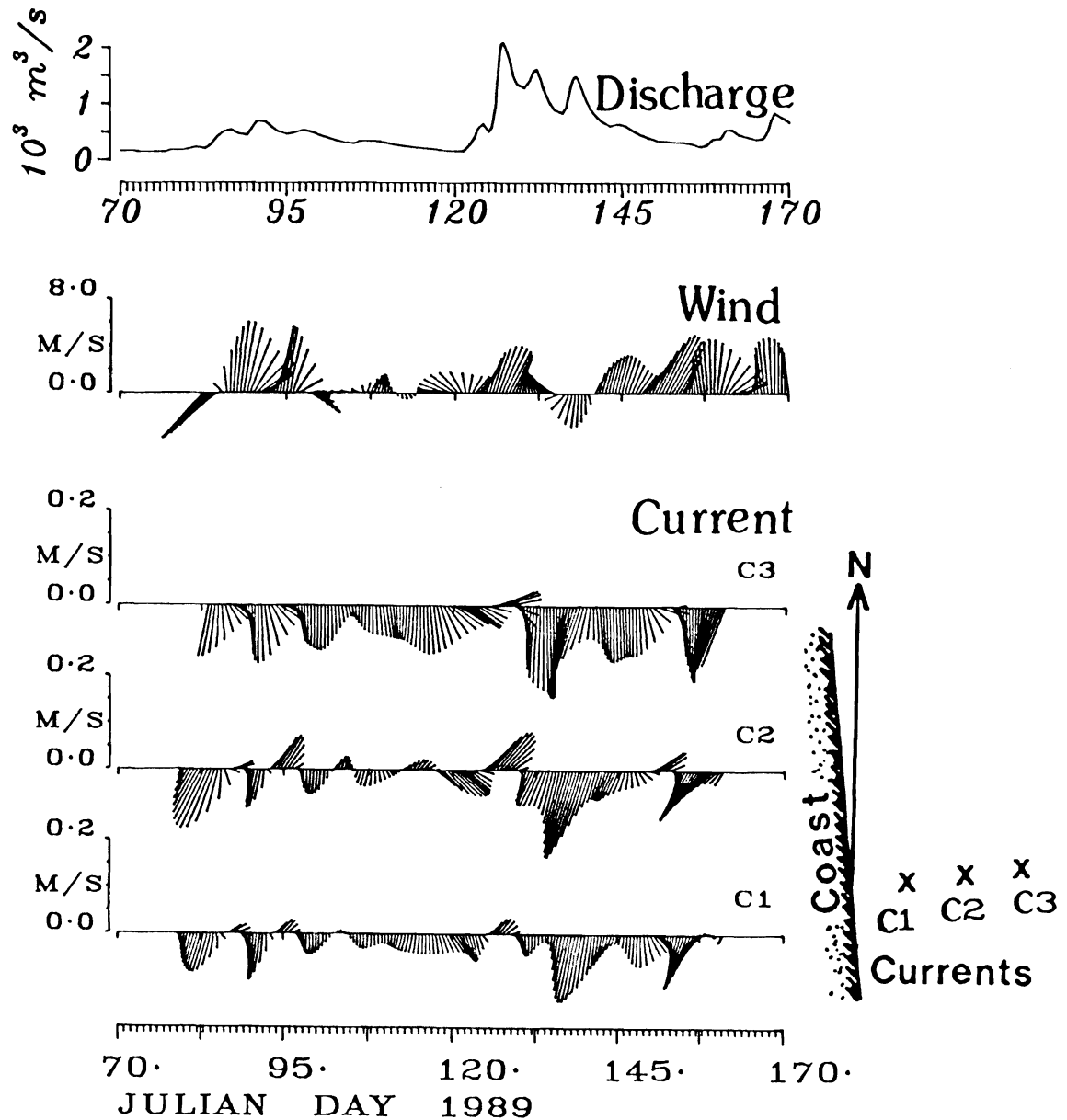


Figure 4.1. Discharge, wind, and current time series. Shown are freshwater discharge of the Delaware River, off-shore winds at EB9, and currents off the coast of Delaware 6 m below the surface (see fig. 1.1, p.8, for locations). I label times of shipboard experiments with letters a through e.

to the data in fig. 4.1. Most of the time I observe indeed a downstream flow opposing the local winds. I further indicate in fig. 4.1 the periods of shipboard experiments and drifter deployments. Table 4.1 summarizes the data sources for the experiments, all of which covered the plume region. I list pertinent details of each experiment, too, and note where in this dissertation one finds detailed discussions of each event.

This chapter is organized as follows. First I introduce the hydrography in order to emphasize the main characteristics of what I define to constitute the plume region (section 4.2). The statistical analysis of moored current meter data in section 4.3 will then reveal the temporal structure of the flow field in the plume region and how it differs from that of ambient shelf waters. I will find that the flow at wind dominated time scales (days) is little different from the shelf. At lower frequencies (weeks), however, the response to wind and buoyancy forcing varies on along-shore scales of about 100 km, while I observe the same variability on across-shelf scales of about 10 km. Focusing then on the smaller spatial scale, I utilize drifter data to describe the very low frequency flow field in section 4.4. Even though the data are Lagrangian, I construct Eulerian averages which compare well with those from moored current meters. The dispersion of drifters I address in section 4.4.4. The interaction of wind and buoyancy forcing is the subject of section 4.5 where I explain vertical current profiles. Section 4.6 then diagnoses the horizontal current structure. I will find that the flow field dynamics is linear and approaches geostrophic balance across

Table 4.1. Summary of experiments and data sources. I list only shipboard experiments downstream of the Delaware Estuary. The column "text" indicates the page number in the text where I discuss the respective events in detail.

Map Date	CTD	ADCP	S4	Buoys	AVHRR	Text
	Transects				Image	
(a) 03-12/13-1989	2	yes	yes	0	no	none
(b) 04-28/29-1989	2	yes	yes	0	yes	p.165
(c) 05-25-1989	2	no	yes	7	no	p.88
(d) 06-13/14-1989	2	yes	yes	4	yes	p.107
(e) 06-16/17-1989	2	yes	yes	4	yes	p.107
(f) 05-24/25-1990	3	yes	no	0	no	p.134
(g) 06-13/14-1990	6	no	no	0	no	p.134

the shore. The last section 4.7 concludes this chapter with a discussion of scales and parameters.

4.2 Hydrography

Salinity is an excellent tracer of estuarine waters on the shelf. In our study area density varies almost linearly with salinity. I will next present 7 maps of the salinity field and augment each with a transect across the shelf. Since buoyant plume waters extend to the bottom, surface salinity maps catch most features of the plume region.

The thermosalinograph aboard the ship continuously pumps water from 0.5 m below the surface, measures temperature and conductivity, and computes its salinity. The sampling time is 30 s, but here I block average data for 5 minutes along the ship track. These irregularly spaced data I interpolate onto a rectangular grid with respective across- and along-shore resolutions of 2 and 4 km. Finally, a spatial low-pass filter removes numerical, instrumental, and physical variability below scales of about 6 km and 20 km across and along the shore, respectively. Each map I augment with a vertical salinity transect.

The seven maps of surface salinity in fig. 4.2 exhibit important similarities and differences. I always find brackish waters downstream, but only once (fig. 4.2f) upstream of the source. The width of low salinity water

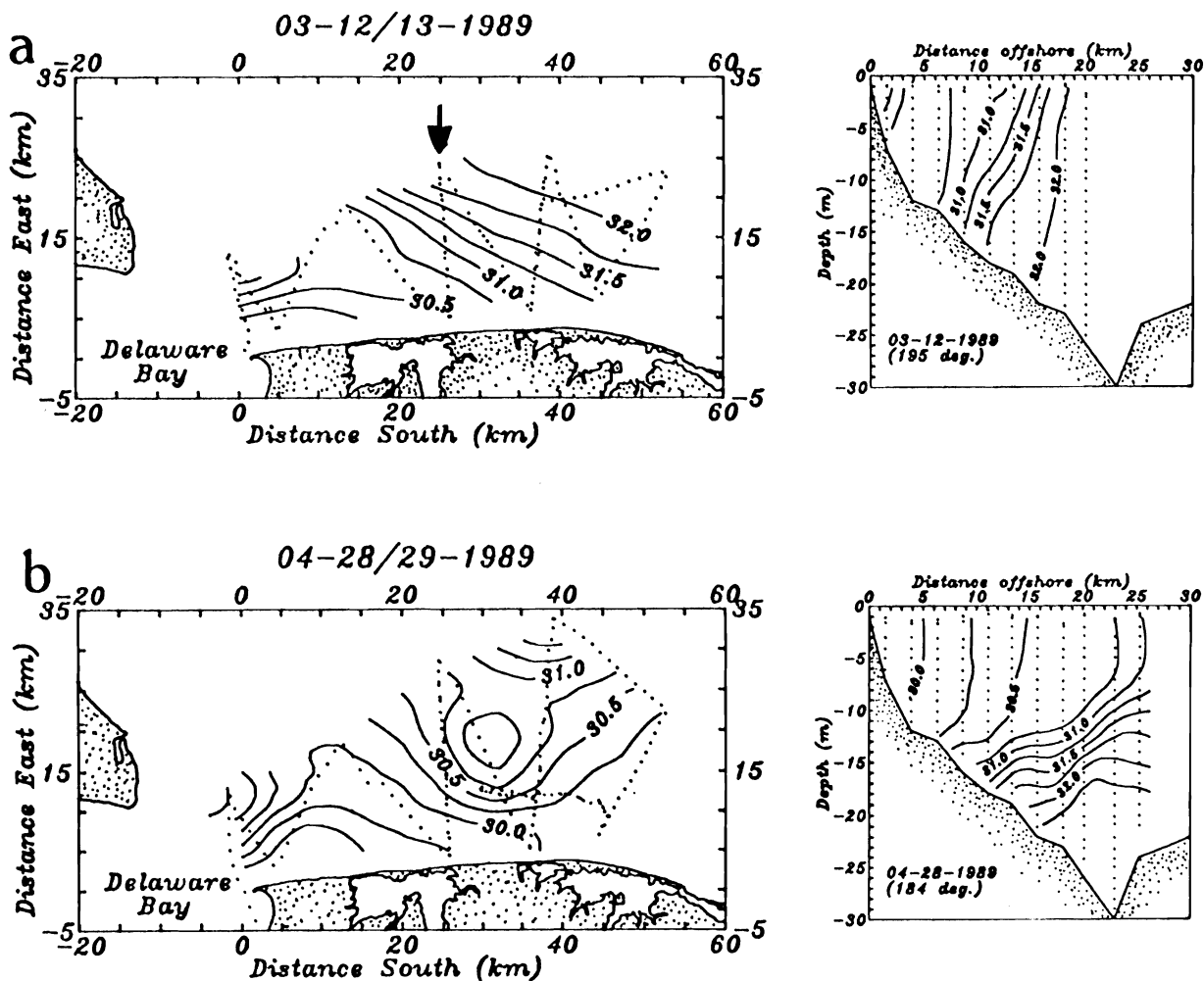


Figure 4.2. Seven maps of surface salinity for the plume region. Dotted lines indicate the ship track along which the data were collected. To the right of each map I depict a transect which shows the vertical distribution of salinity. The transect location I indicate in fig. 4.2a. For time series data during experiments in 1989 (a through e) see fig. 4.1 (p.68).

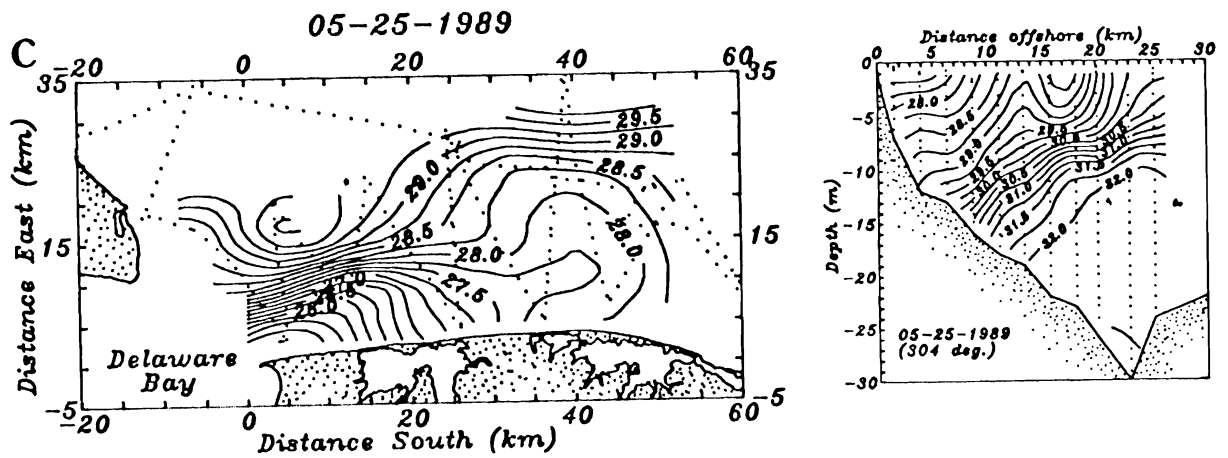


Figure 4.2. Seven maps of surface salinity for the plume region. Dotted lines indicate the ship track along which the data were collected. To the right of each map I depict a transect which shows the vertical distribution of salinity. The transect location I indicate in fig. 4.2a. For time series data during experiments in 1989 (a through e) see fig. 4.1 (p.68).

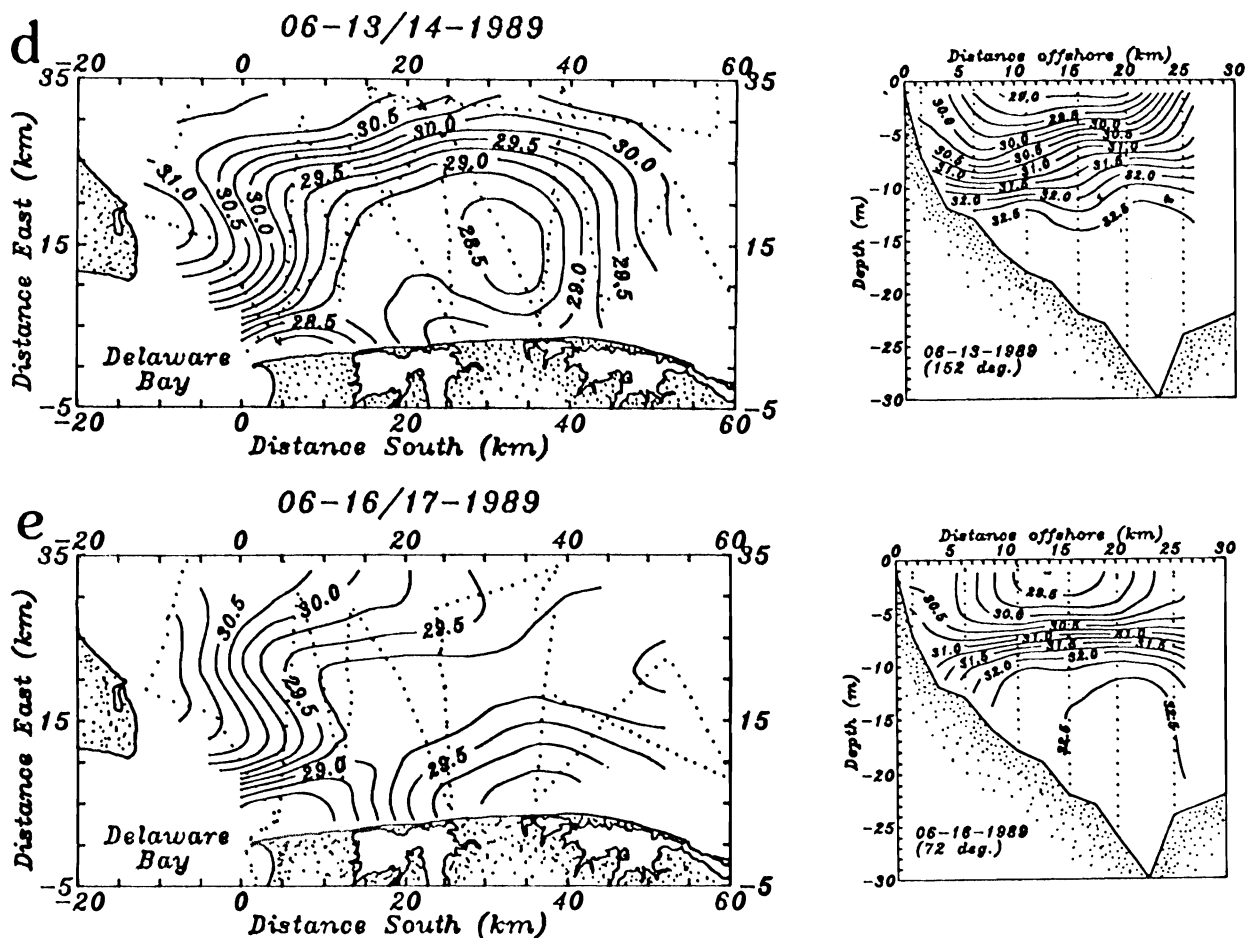


Figure 4.2. Seven maps of surface salinity for the plume region. Dotted lines indicate the ship track along which the data were collected. To the right of each map I depict a transect which shows the vertical distribution of salinity. The transect location I indicate in fig. 4.2a. For time series data during experiments in 1989 (a through e) see fig. 4.1 (p.68).

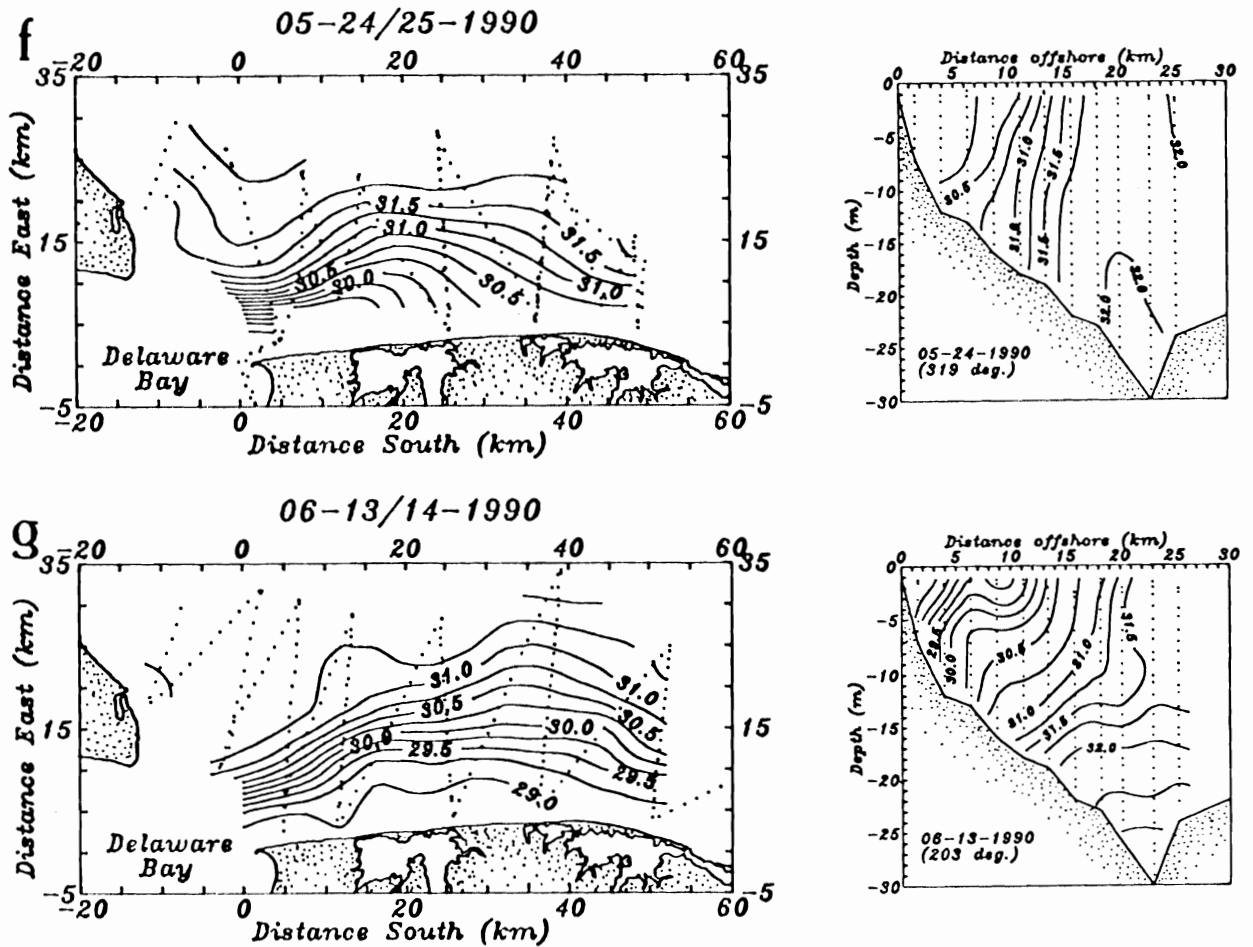


Figure 4.2. Seven maps of surface salinity for the plume region. Dotted lines indicate the ship track along which the data were collected. To the right of each map I depict a transect which shows the vertical distribution of salinity. The transect location I indicate in fig. 4.2a. For time series data during experiments in 1989 (a through e) see fig. 4.1 (p.68).

increases from the source downstream in all cases. Near the mouth of the Delaware Estuary the outflow is about 8 km wide while 30 km downstream the plume has widened by a factor between 2 (fig. 4.2f) and 5 (fig. 4.2c). Further downstream yet, contours approach the coast again, thus indicating a narrowing of the current which transports buoyant waters downstream. In most of the maps, however, we do not resolve this feature very well, but I believe it is there and provide fig. 4.3 as a vivid example (Wong and Münchow, 1991). The surface salinity is the same as that in fig. 4.2f, but I overlay subtidal ADCP current estimates from 6 m below the surface. The plume first spreads before narrowing about 45 km from the source as the result of strong onshore currents. Downstream the buoyant region is only 8 km wide. Modeling studies by Chao and Boicourt (1986), Garvine (1987) and O'Donnell (1990) all predict the widening of a buoyant discharge before a narrow coastal current forms downstream. I refer to the narrow region downstream as the coastal current region, but defer a discussion to the next chapter.

The phrase "plume region" is meant to be a dynamical, not a geographical one. In March and April of 1989, when freshwater discharge rates were low, the plume region was closer to the mouth of the estuary (figs. 4.2a and 4.2b). Even then, however, I observed an initial widening of buoyant waters away from the source and a subsequent narrowing. In chapter 6 I will show that especially in April (fig. 4.2b) the coastal current is very much present. In fig. 4.2c I show the plume region of the coastal

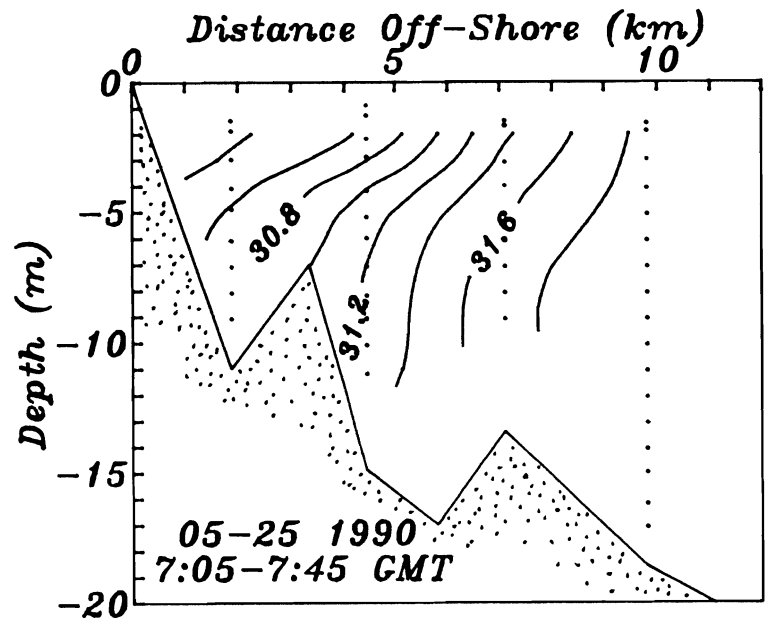
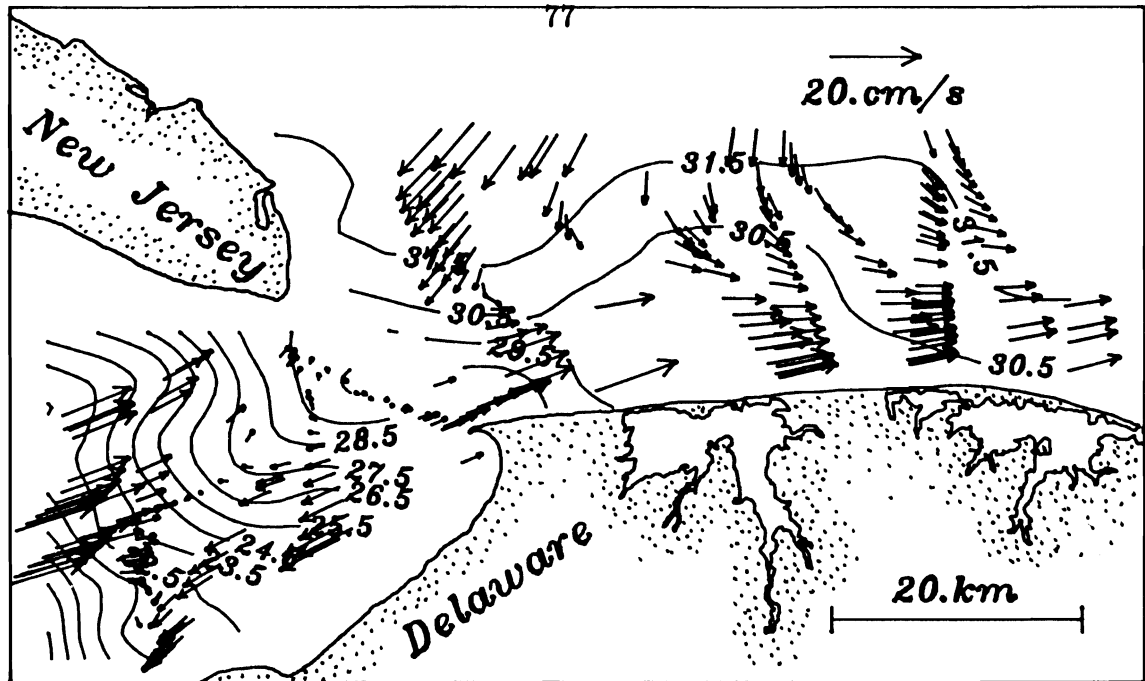


Figure 4.3. Subtidal current vectors on salinity map in May 1990. Note the onshore flow about 20 km from the shore and the narrowing salinity field about 40 km from the mouth of the estuary (from Wong and Münchow, 1991).

current after a surge of fresh water from the Delaware River (see fig.4.1, p.78) floods the shelf. Horizontal salinity gradients exceed 0.3 psu/km for more than 10 km along the shore near the source, only to weaken somewhat as the plume reaches a maximum width of 30 km about 40 km from the mouth of the estuary. The plume then resembles the head of a gravity current, but a topographic deflection of the coastal current or moderate upwelling favorable winds (see also fig. 4.8b, p.92 for drifter trajectories during this event) may explain the feature as well. Figs. 4.2d and 4.2e describe the temporal evolution of the plume region under strong upwelling favorable winds. Plume waters in fig. 4.2e appear to flood the shelf. Nevertheless, the outflow at the mouth of the estuary still turns clockwise, i.e., downstream. In 1990 I find a plume region much narrower than 1989 (figs. 4.2f and 4.2g) which is the result of weak to moderately downwelling favorable winds. The plume still widens, however, until about 35 km from the source before narrowing again some 20 km further downstream.

In order to convince the reader that the buoyant plume waters generally contact the bottom, I present in fig. 4.2 the salinity as a function of depth and off shore distance. For each map I show a transect at 25 km south whose exact location I indicate in fig. 4.2a. Except for the strong upwelling event (figs. 4.2d and 4.2e) isohalines intersect the bottom and the surface. The most saline waters often appear over the offshore remnant of the deep Delaware ancestral channel about 24 km offshore. This is ambient shelf water as it is drawn toward the estuary.

4.3 Eulerian Current Statistics

4.3.1 Introduction

Long time series of velocity data from moored current meters allow me to analyze the temporal variability of currents on the shelf. In the time domain I compute cross-correlations with winds and freshwater discharge rates, while in the frequency domain I estimate the coherence of currents at different locations. The analysis will reveal that wind and buoyancy forcing dominate processes at different time scales and that the core of the low frequency (<0.1 cycles/day) buoyancy driven coastal current is about 15 km from the coast. The results of this section shall also provide the statistical background for the events that I discuss in later sections.

The first step in any statistical analysis is to determine the effective degrees of freedom of the data on hand. Determining them is often a tricky question with immense consequences to the subsequent statistical analysis. Many authors interpret the first zero crossing of the auto-correlation function as an estimate of the decorrelation time scale (Mayer et al., 1979; Masse, 1988). I here, however, adopt the method proposed by Poulain and Niiler (1989) who integrated the auto-correlation function to the first zero crossing. The decorrelation time scale is then an upper bound of the integral time scale which has a first maximum at the first zero crossing.

The ratio between the record length T and the decorrelation time T_D sets the number of the independent observations N in the record, i.e., $N=T/T_D$. In table 4.2 I list T , T_D , and N for all current meters I will be using in this chapter. Also in table 4.2, I give the directions which I define as along-shore for each instrument. This orientation I took as the inclination from true East (positive counter clockwise) of the major axis of the Reynolds stress tensor

$$R_{ij} = \overline{q_i q_j},$$

where $i,j=1,2$ and q_1 and q_2 are the east and north component of the current deviations from the mean (\bar{u}, \bar{v}) , i.e.,

$$u(t) = \bar{u} + q_1(t)$$

$$v(t) = \bar{v} + q_2(t)$$

and the overbar represents a time average. The analysis techniques are standard (Sokal and Rohlf, 1981, p.594; Kundu and Allen, 1976) and not repeated here. The mean current vector (\bar{u}, \bar{v}) and the principal axes of R_{ij} I presented earlier (fig. 2.5, p.19). In this section I concentrate on the correlation of the current fluctuations q_i with wind, fresh water discharge, and currents measured at other locations. First, I present such correlations in the time domain before switching to the frequency domain.

Table 4.2. Results of time domain statistics. T is the record length, T_d the decorrelation time scale, N the degrees of freedom, θ the along-shore direction in degrees from true East (positive counter-clockwise), and q and θ_q are the record mean speed and direction, respectively. An asterisk "*" behind q or θ indicates that the value is not significant at the 95% confidence level.

Label	T (days)	T_d (hrs)	N	θ (deg)	q (cm/s)	θ_q (deg)
C1	92	20	111	258	3.9±1.6	-67±18
C2	92	26	85	250	3.2±2.8	-59±28
C3	87	20	106	250	8.4±2.2	-66±10
C1B	46	16	71	280	2.2±2.0	-87±30
C2B	41	28	41	259	3.1±3.6*	-59±36*
A1	95	22	105	243	1.7±2.1*	±180*
A2	49	20	60	239	1.6±2.8*	±180*
A3	50	21	80	229	1.0±2.3*	±180*
A1B	95	15	153	253	3.1±1.3	-169±18
A2B	41	15	72	248	1.9±1.1	-179±22

4.3.1 Time Domain

The lagged cross-correlation between along-shore currents with along-shore winds (fig. 4.4a) mirrors the results of previous studies on inner shelves (Csanady, 1978; Pettigrew, 1981; Hopkins and Swoboda, 1986). The response of currents is almost instantaneous (peak correlation at about 6 hours lag), barotropic, and about 0.6 ± 0.15 , i.e., the wind explains about $60\% \pm 15\%$ of the along-shore current fluctuations. The 15% uncertainty represents a standard error (Barlett, 1978) that assumes zero true correlation between the two variables. In fig. 4.4a I shaded correlations that differ significantly from zero. The response of the cross-shelf flow component to the same along-shore wind, however, I show in fig. 4.4b. Maximum correlation still occurs at about 6 hour lag, but while the correlations near the surface are barely significant and negative, i.e., downwelling favorable winds correlate with onshore flow, the correlation near the bottom is much stronger (0.5 ± 0.15) and positive, i.e., downwelling favorable winds correlate with an offshore flow. The somewhat weaker correlation near the surface I explain with stronger buoyancy forcing there. I present a more complete verification of this "Ekman like" circulation in water barely 20 m deep in section 4.5 (p.107) with ADCP and CTD data.

The final cross-correlation that I present is between the along-shore current and the freshwater discharge rates of the Delaware River. Correlations are weaker than they were for the wind (0.3 ± 0.15) and

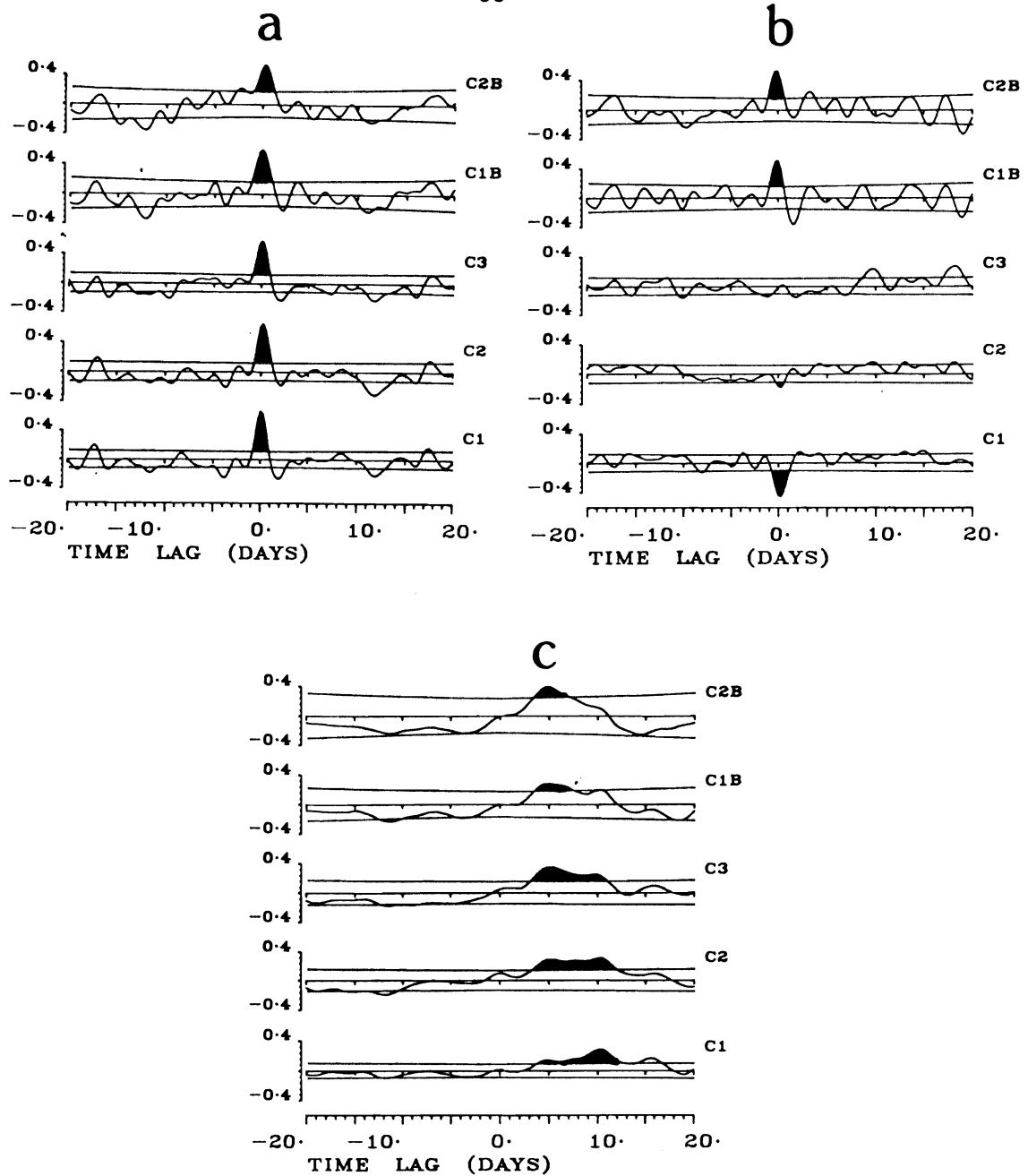


Figure 4.4. Lagged cross-correlations. (a) Along-shore winds and along-shore currents; (b) along-shore winds and across-shore currents; (c) freshwater discharge and along-shore currents. Correlations that are significant at the 95% confidence level are shown in black. C1B and C2B refer to data from near the bottom at locations C1 and C2, respectively (see fig. 1.1, p.8, for locations).

maximum lag occurs between 5 and 10 days (fig. 4.4c). Hence it takes almost 10 days for the run-off signal to reach the shelf. Garvine (1991) reported positive correlation between these two variables in this region at lags between 8 and 20 days with a peak (0.5 ± 0.23) at 14 days. His result is thus similar to the ones I report here. In fig. 4.4c I notice that the lag time of surface currents close to the shore at C1 exceeds the lag time at C3 which is located 15 km from the coast. Surface currents there respond to changes in freshwater discharge first. Also, I often find the zone of largest horizontal density gradients and largest current speeds at this location. In the next section I argue that the core of the coastal current lies near the offshore edge of the plume region.

4.3.2 Frequency Domain

In this section I seek to convince the reader that the core of the buoyancy driven coastal current lies more than 8 km from the shore. The argument will utilize frequency domain coherence analysis, i.e., I assume a linear system between input and output (Bendat and Piersol, 1980) of currents 6 m below the surface. The input time series is always the along-shore velocity component at C1 (see fig. 4.5) which is located 5 km off the coast of Delaware. The output time series are the along-shore velocity component from moorings that are located 70 km upstream (A1) of C1, 3 km offshore (C2) of C1, and 10 km offshore (C3) of C1. Fig. 4.5 depicts the locations of all current meter moorings and the results of the coherence

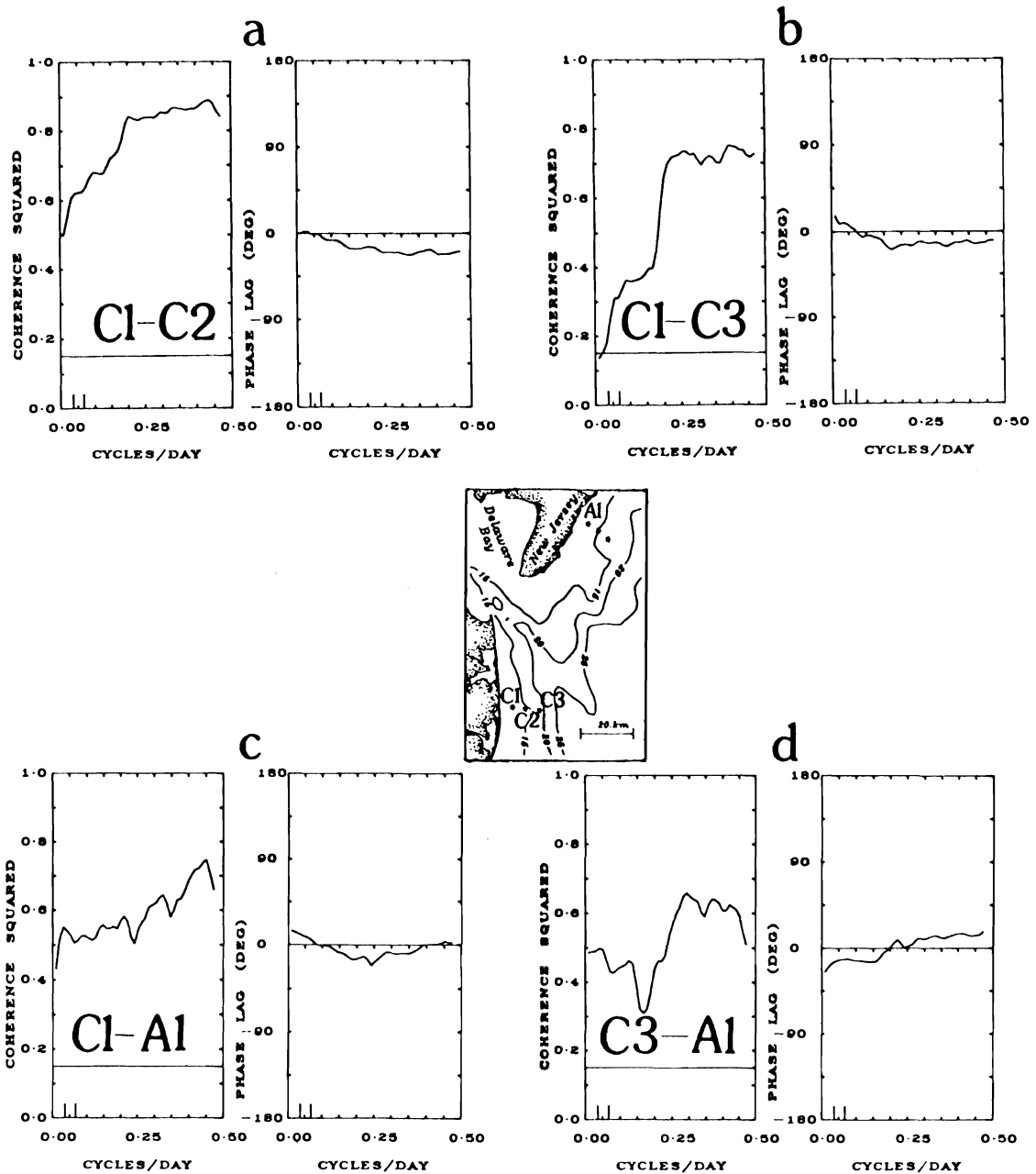


Figure 4.5. Coherencies of along-shore surface currents. The spatial separations are (a) 3 km across-shore off Delaware; (b) 10 km across-shore off Delaware; (c) 70 km along-shore; (d) 75 km along-shore. The map near the center shows the location of the data sources.

analysis in frequency space. For comparison I also compute the coherence between currents at C3 and A1, the locations where I often find the largest currents.

Fig. 4.5a shows the coherence of current between C1 and C2. The station separation is only about 3 km and consequently 90% ($\Gamma^2 \approx 0.9$) of the surface currents at C1 correlate with those at C2 at high frequencies (>0.25 cpd). At low frequencies (<0.1 cpd), however, the coherence drops to about 0.5. The phase indicates that currents at C1 lead those at C2 with a constant time delay of a few hours. Across the shelf in the plume region the coherence between currents at C1 and C3 exhibits contrasting behavior at low frequencies (fig. 4.5b). The coherence drops dramatically at low frequencies, i.e., at 0.1 cpd only 20% of the variance inshore (C1) correlates with that 10 km further offshore (C3). The phase indicates little difference. Finally, I correlate currents off Delaware with those 70 km upstream off New Jersey (figs. 4.5c and 4.5d). In comparison with coherencies across the plume region I find lower coherencies at high frequencies ($\Gamma^2 \approx 0.6$), but higher coherencies at low frequencies that always exceed 0.4. All results are significant at the 95% confidence level as all coherencies exceed 0.17. In summary I conclude that currents in the plume region at periods larger than 10 days are more coherent 70 km along the shelf than 10 km across it.

What is the cause for this very different coherence along and across the shelf? I argue that in different parts of frequency space different

processes dominate, i.e., the wind dominates only on the ambient shelf at all frequencies. In the plume region, however, winds dominate at high frequencies (>0.2 cpd) only, while buoyancy dominates at low frequencies (<0.1 cpd). Further, I argue that while the buoyancy forcing varies spatially in the across-shore direction, the winds are spatially uniform. Applying these hypotheses to fig. 4.5 can explain the observed variability. Within 5 km of the coast at C1 and A1 buoyancy forcing is weak, thus currents correlate well along the shelf at all frequencies. Comparing currents 5 km from the shore with those 15 km from it, in contrast, I find high correlations at high frequencies because the winds are spatially uniform and dominate the circulation. At low frequencies, however, I find low correlations because the buoyancy forcing dominates at these frequencies at 15 km but not at 5 km from the coast.

In a geostrophic current that is in thermal wind balance I expect largest currents where lateral density gradients are largest. Largest density gradients I observe more than 15 km from the coast (see fig. 4.2, p.72). Therefore it is no surprise that buoyancy forcing dominates over wind forcing 15 km from the shore but not 8 km from the shore. Additionally, lateral and vertical friction will retard currents close to the shore more than it will farther offshore. I thus conclude that the core of the buoyancy driven coastal current is located away from the coast.

4.4 Lagrangian Perspective

4.4.1 Introduction

In recent years oceanographers have utilized buoys as moving current meters (Richardson, 1983) and dispersing particles. Davis (1991) reviews the history of oceanic drifter application and underlying dynamical concepts. The same author pioneered the instrumental and experimental design of coastal drifter studies (Davis 1985a; Davis 1985b). Since our drifter and drogue design followed his closely, I omit a detailed discussion here, but mention that we drogued our drifters 3 m below the surface, tracked them for 2 to 4 days with the ARGOS system, and retrieved, checked, and redeployed them again further upstream. This way we collected 96 drifter data days in the plume region between Julian day 128 and 168. Fig. 4.6a shows the deployment locations while fig. 4.6b depicts the deployment periods along with wind, freshwater discharge, and current meter measurements during the experiments. Winds were generally upwelling favorable, thus opposing the buoyancy driven coastal current which was close to its annual peak during these experiments. For most drifter deployments I have complementary shipboard data (thermosalinograph, ADCP, and CTD), but these I discuss in a different context elsewhere (see table 4.1, p.70). Here I will first describe trajectories qualitatively (section 4.4.2) before computing Lagrangian velocities which I then analyze statistically (section 4.4.3). I will find that the drifters in the plume region respond to both wind and buoyancy

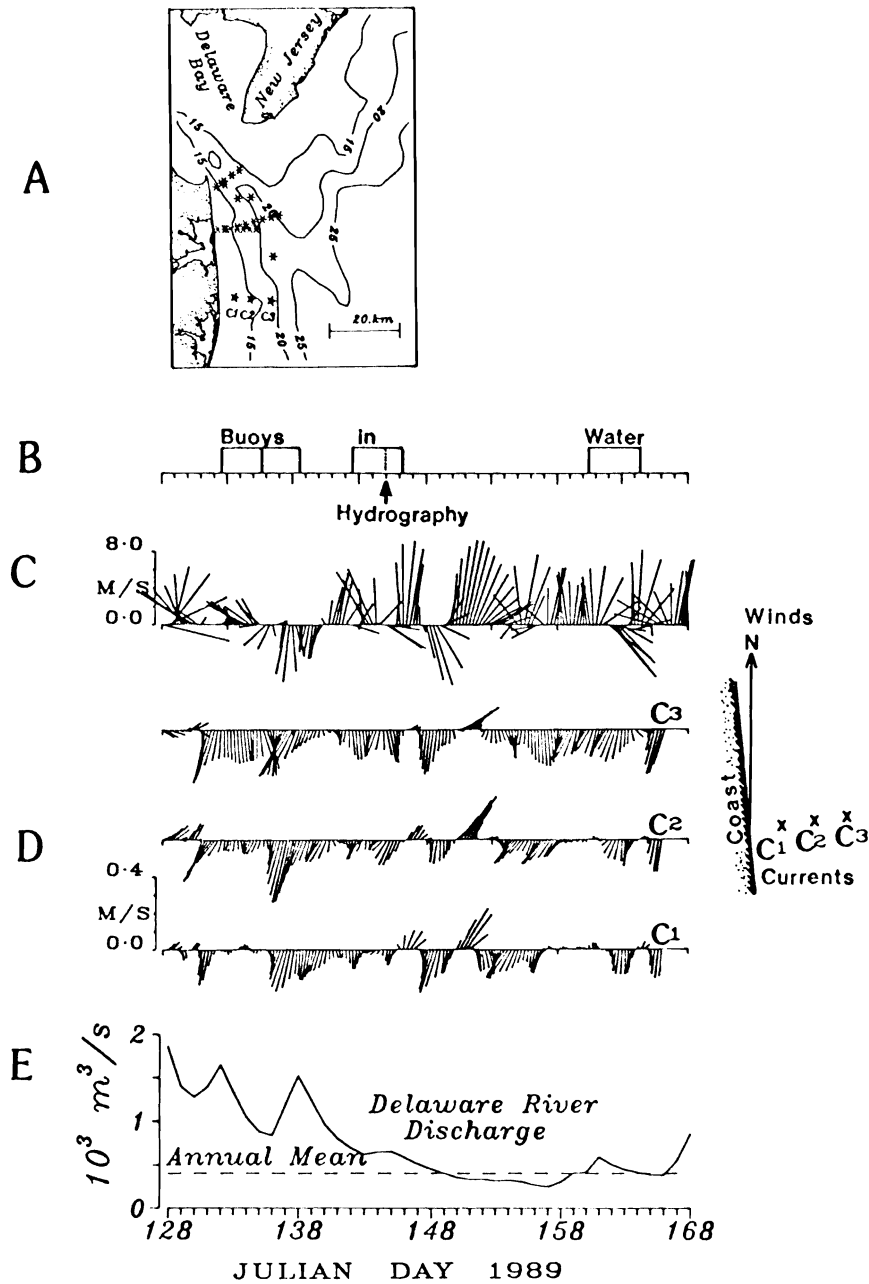


Figure 4.6. Locations and periods of drifter deployment. Also shown are time series (c) wind, (d) currents, and (e) freshwater discharge rates during the drifter deployments.

forcing, that mean currents and time scales agree well with their Eulerian analogs, and that horizontal diffusivities are about $2000 \text{ m}^2/\text{s}$ and $400 \text{ m}^2/\text{s}$ along and across the shelf (section 4.4.4), respectively.

4.4.2 Trajectories

The ARGOS satellite system provides between 6 and 8 positions per day for each drifter with an accuracy of better than 350 m. To each trajectory I fit a cubic spline and subsample position data every 3 hours. I show in fig. 4.7 all trajectories. The apparent disorder in this "spaghetti diagram" (Riser and Rossby, 1983) becomes more orderly and coherent when I separate the data from different deployments by the respective wind direction. In fig. 4.8 I thus redraw the trajectories during downwelling, upwelling, and transitional winds, respectively. Common to all experiments is the downstream displacement. About 20 km from the coast the offshore velocity component becomes dominant. Inshore, however, surface currents are frequently against the wind due to strong buoyancy forcing. When winds are downwelling favorable (fig. 4.8a) the downstream displacement is swift, since then wind and buoyancy act in concert on the shelf. Drifters then either ground on the local beaches or leave the plume region within a day. Speeds reach 50 cm/s .

I observe much smaller displacements and speeds during upwelling favorable winds (fig. 4.8b), but inshore currents are still downstream with an

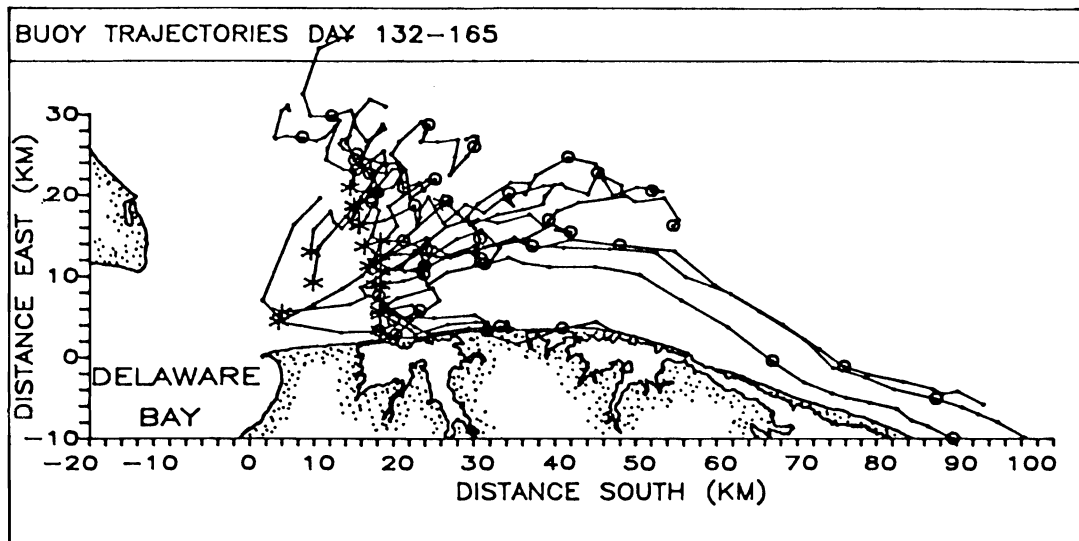


Figure 4.7. Trajectories of all drifters. I added open circles every 24 hours after each drifter's deployment.

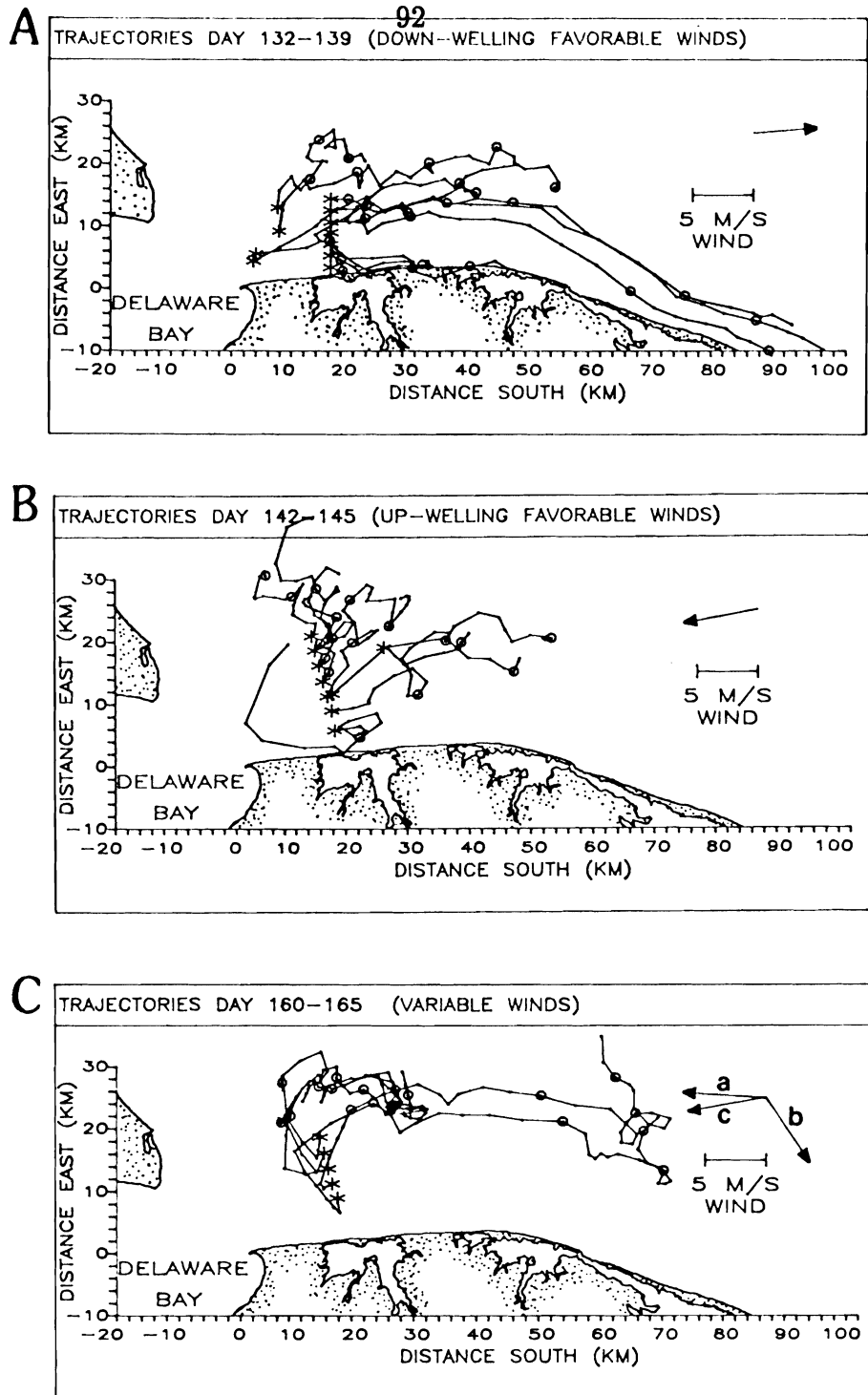


Figure 4.8. Drifter trajectories sorted by wind direction. (a) downwelling favorable winds; (b) upwelling favorable winds; (c) transitional winds. The wind vector and scale appears on the right of each figure. I added open circles every 24 hour after each drifter's deployment.

offshore velocity component that increases in the offshore direction. The resulting divergence must be compensated by upwelling. Qualitatively, this is consistent with an "Ekman" layer like response to winds superposed on a downstream buoyancy driven coastal current. Ekman (1905) predicts a surface displacement of less than 10 degrees clockwise from the wind direction (see fig. 4.15, p.116) for water only 20 m deep. Csanady (1976) predicts a flow in the direction of the wind as he postulates a balance between surface and bottom stresses in the coastal boundary layer. Neither is the case here. Instead, I interpret the trajectories as a linear superposition of buoyancy and wind forced motion. Within the plume region buoyancy dominates over wind forcing, while offshore the reverse holds.

The most inshore drifter in fig. 4.8b warrants some special attention. It apparently either enters the surf zone and moves upstream with the wave generated along-shore current, or it enters a recirculation eddy behind a shoal (Hens and Chickens Shoal, see fig. 3.1b, p.28) near the source region. Tidal currents inject the drifter back into the estuarine outflow where it follows the "normal" path, downstream and offshore.

Finally, in fig. 4.8c I show trajectories from a deployment 4 days long. Winds change rapidly from one day to the next from upwelling favorable to downwelling favorable and back to upwelling favorable. This experiment thus combines effects of figs. 4.8a and 4.8b. Initially drifters move offshore, again at an angle about 60 degrees to the right from the wind,

before turning anti-cyclonically and swiftly racing downstream. Finally, the drifters again adjust to the now upwelling favorable winds by moving offshore. Note that the response to the wind is rapid, consistent with results from the last section. There I reported wind response times of about 6 hours.

Comparing all three experiments in fig. 4.8 I stress the apparent transverse current shear of the flow. This is a feature of the coastal current rather than the wind, as I will show in the next section. In summary, however, winds impose an important but not dominant perturbation onto the buoyancy driven coastal current. While upwelling favorable winds remove estuarine material efficiently from the estuary (Garvine, 1985) and transport them offshore, downwelling favorable winds will cause the same material to be stranded just as efficiently on beaches downstream of the estuary.

4.4.3 Currents

In order to remove tidal and inertial variability from the drifter data, I subject the 3-hour subsampled position data to a fifth order polynomial which acts as a low-pass filter. Subtidal velocity estimates I then obtain by center differencing buoy positions at different times. Two different mean velocities can be computed from drifter data. Averaging velocity data observed near a fixed point (spatial bin) constitutes an Eulerian average. Averaging velocity data of drifters deployed near a point (spatial bin) constitutes a Lagrangian average. Here I compute Eulerian averages

only, except for the following discussion of the Lagrangian auto-correlation.

The Lagrangian auto-correlation can be used to estimate the degrees of freedom in the data set. The auto-correlation $R(\tau)$ I define as

$$R(\tau) = \frac{\langle u'(t) u'(t+\tau) \rangle}{\langle u'^2(t) \rangle}$$

where

$$u(t) = \langle u \rangle + u'(t)$$

and

$$\langle u \rangle = \lim_{T \rightarrow \infty} \frac{1}{T} \int_0^T u(t) dt \approx \frac{1}{N} \sum_{i=1}^N u(t_i)$$

N represents the number of observations of an individual drifter and all properties are Lagrangian. Krauss and Böning (1987) describe the practical evaluation of the $R(\tau)$ and related properties. In fig. 4.9 I present $R(\tau)$ for the along- and across-shore velocity component. Following Brink et al. (1991) and Poulain and Niiler (1989) I take the integral of $R(\tau)$ to the first zero crossing as an estimator of the decorrelation time scale T_D which then is about a day. This time scale is similar to those which I estimated above for Eulerian current meter data.

In the following I present the spatial distribution of Eulerian mean currents and deviations thereof. I thus use the drifters merely as "moving

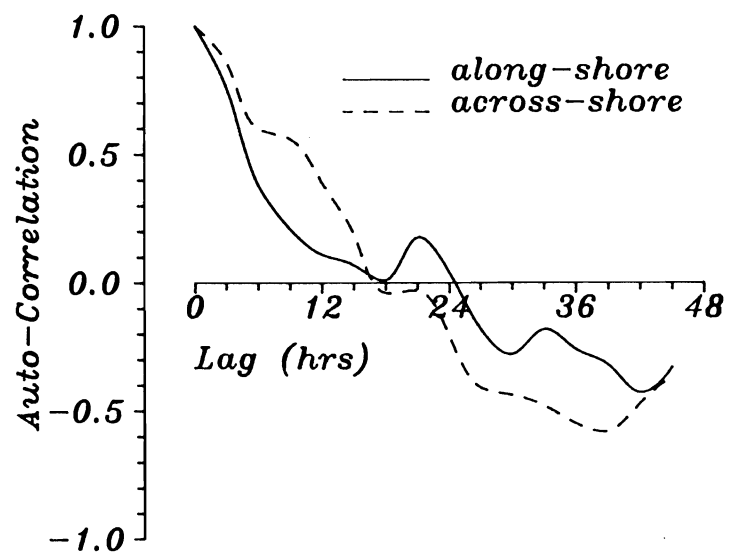


Figure 4.9. Lagrangian auto-correlation function. Note the deep side lobes that are suggestive of an oscillatory current.

current meters." In order to obtain statistically significant results I average all velocity data into spatial bins 10 and 20 km wide in the across- and along-shelf directions, respectively. I require the mean currents to have a preferred direction and thus apply the Raleigh test (Mardia, 1972) for non-uniform directional distribution of the data. The underlying assumption of this test is the von Mises probability distribution which is the equivalent to the Gaussian normal distribution on a unit circle. Further, I require at least 8 degrees of freedom of any bin averages. The latter condition assures that data from different experiments enters the average. I use only data passing both criteria in the subsequent analysis.

In table 4.3 I summarize the results that I plot in fig. 4.10 and discuss next. All mean currents (fig. 4.10a) are highly directional as the 95% confidence levels for direction indicate. Mean currents beyond 20 km south are strong (~ 20 cm/s) and downstream. They describe the coastal current when the buoyancy forcing reaches its annual peak. The location of each vector corresponds to the "center of gravity" (Kirwan, 1988) of drifters whose velocity enters the average. Also in fig. 4.10 I give the results from current meters moored 6 m below the surface and label them C1, C2, and C3. The mean currents from drifter and mooring data have different magnitudes and slightly different directions near the shore. Drifter speeds reach 20 cm/s while speeds from current meters never exceed 12 cm/s. Remember that the buoys are drogued 3 m below the surface, while the current meters are moored 6 m below the surface, and that the water is always shallower than

Table 4.3. Eulerian statistics from drifters and current meters. Data in A (Drifter) and B (current meter) for time period between Julian day 128 and 168. (x,y) denotes the position in km south and east, respectively; N represents the degrees of freedom, q the mean current, and θ its direction from true east (positive counter-clockwise); R_{maj} and R_{min} are the principal axes of the velocity deviations, ψ the orientation of R_{maj} from true east, and R_{em} is the ratio of "eddy" to "mean" kinetic energy.

(x,y) km	N	$q \pm \Delta q$ cm/s	$\theta \pm \Delta \theta$ deg	R_{maj}	R_{min}	ψ	R_{em}
				cm/s		deg	
(A) Drifters							
(12.4,26.5)	15	6.6 \pm 5.4	-16 \pm 48	10.7	7.4	74	3.6
(20.8,9.7)	10	19.0 \pm 14.8	-79 \pm 27	13.2	9.0	120	0.6
(20.6,19.0)	19	10.8 \pm 8.1	-31 \pm 32	10.8	7.3	87	2.1
(18.6,26.1)	19	6.3 \pm 9.0	-44 \pm 48	13.5	6.9	54	5.5
(26.5,10.5)	7	15.7 \pm 9.2	-68 \pm 15	6.4	3.9	97	0.2
(29.6,19.0)	16	13.7 \pm 6.5	-80 \pm 20	10.9	6.0	81	0.8
(B) Current meters							
(36.5,8.1)	41	5.9 \pm 1.3	-94 \pm 22	8.3	2.6	82	2.1
(36.9,12.2)	28	6.4 \pm 2.9	-93 \pm 25	10.1	2.9	69	2.6
(37.6,18.2)	33	11.4 \pm 3.2	-77 \pm 15	9.0	3.3	76	0.7

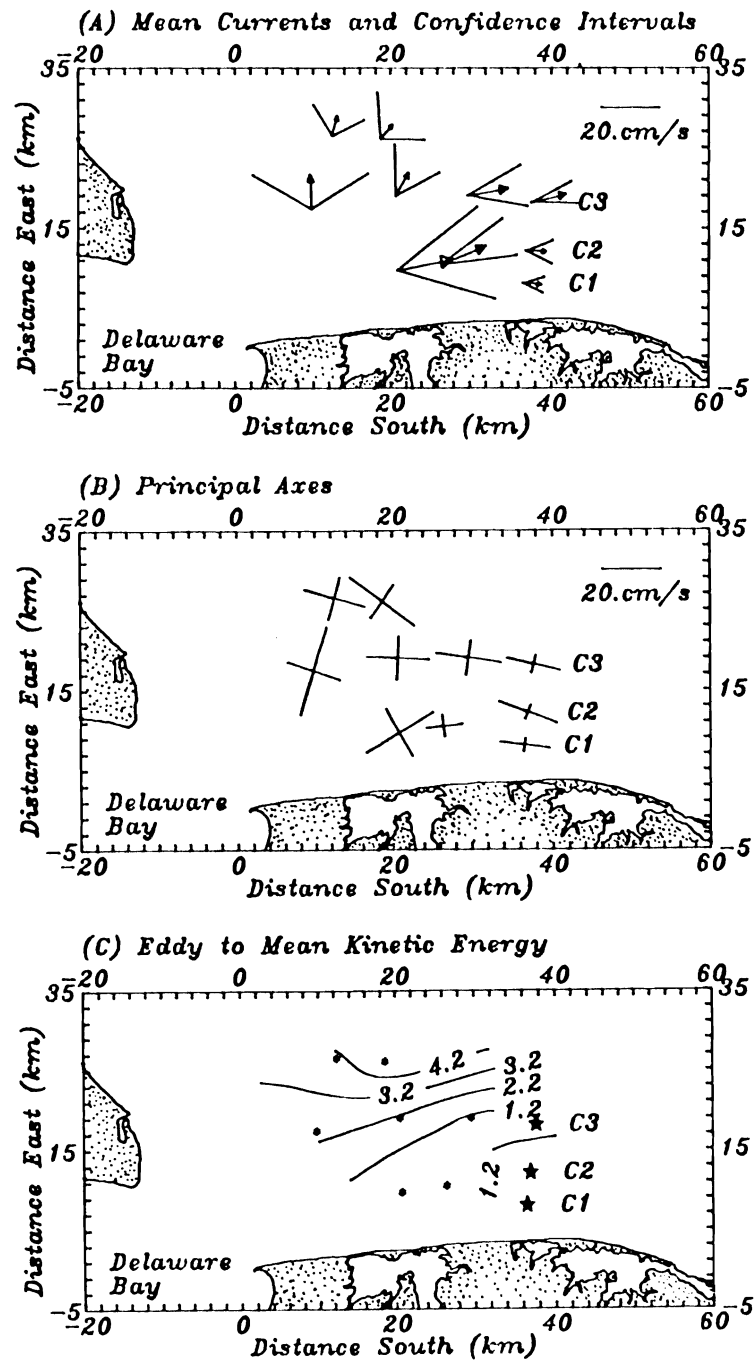


Figure 4.10. Eulerian statistics from drifter and current meter data. The latter data I label as C1, C2, and C3: (a) mean currents and 95% confidence intervals for speed and direction; (b) principal axes of the deviations from the mean; (c) ratio of eddy to mean kinetic energy.

20 m. Forcing due to buoyancy increases from the bottom toward the surface where it is strongest and I expect currents 3 m below the surface to be stronger than those 15% further down in the water column. Also, the centroid for each computed current vector from drifter data is closer to the source of the buoyancy and experiences stronger forcing. Farther offshore mean currents weaken as the result of smaller horizontal density gradients (see fig. 4.2, p.72). In summary, I interpret fig. 4.10a as a strong manifestation of the two main characteristics of the plume region: baroclinicity and transition.

The principal axes in fig. 4.10b represent the deviations from the mean currents of fig. 4.10a. These axes are the square root of the eigenvalues of the Reynolds stress or covariance tensor (Freeland et al., 1975; Kundu and Allen, 1976). Close to the source region the major and minor axes are of similar magnitude, while farther downstream the deviations become more elliptical and aligned with the local topography. The magnitude of the major axis is about 10 cm/s and spatial variations are smaller and less organized than those of the mean currents. As a result, the ratio R_{em} of eddy (eke) to mean (mke) kinetic energy

$$R_{em} = \frac{eke}{mke} = \frac{\langle u'^2 + v'^2 \rangle}{\langle \bar{u}^2 + \bar{v}^2 \rangle}$$

is dominated by the mean current (\bar{u}, \bar{v}) . Fig. 4.10c shows this ratio and one might select the $R_{em}=2$ contour as the offshore boundary of the coastal

current. Farther offshore mean currents are weak, but the fluctuating currents are fairly uniform throughout the domain; hence R_{em} increases offshore. The core of the coastal current I identify as $R_{em} < 1$, which includes the mooring location C3.

Finally, I wish to add a cautionary note and a physical interpretation of the results of this section. The time scale for the "mean" currents of fig. 4.10a is only somewhat larger than a month. The "mean" thus represents subtidal variability at periods comparable to those of the buoyancy forcing. One can then view the "mean" as a snapshot of monthly variability. The fluctuations, on the other side, represent subtidal processes at higher frequencies which the wind dominates. Therefore, my discussion of mean vs. eddy motion (fig. 4.10c) is more accurately one of subtidal variability at different frequencies. A meaningful separation between the two time scales, i.e., a meaningful "mean", is possible only if a clear spectral gap separates the daily (wind) from the monthly (buoyancy) time scale.

Another aspect of the coastal current is its transverse shear $\partial_y \bar{u}$ which I take as an order of magnitude estimate of the relative vorticity. After averaging velocities from drifter data along the entire plume region in across-shore bins 3.5 km wide, I obtain the lateral velocity profile (fig. 4.11). Again I trust only data which have preferred directions at the 95% confidence level and at least 8 degrees of freedom. The linear fit to the mean along-shore velocities (fig. 4.11) explains 99% of the variance and the slope

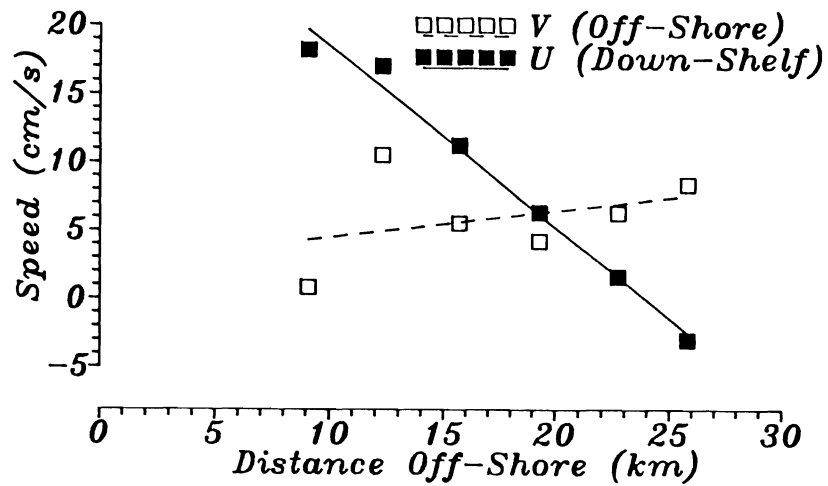


Figure 4.11. Across-shore current profile from drifter data. Data averaged in bins 40 km (along-shore) and 3 km (across-shore) wide. Note the almost linear decrease of the down-shelf velocity component toward off-shore.

implies a ratio of $\partial_y \bar{u}/f$ of about 0.14. The relative vorticity is thus not quite 15% of the planetary vorticity. This finding contrasts with that for the source region where I estimated that relative vorticity is about 80% of the planetary vorticity and $\partial_y u$ was not constant there as it is here in the plume region.

The constant mean shear will partly facilitate the analysis of dispersion in the next section. There one of the many assumptions is that the turbulence of the flow is homogeneous, i.e., the current shear of the mean has to be constant at most (Monin and Yaglom, 1975, p.53). The across-shelf velocity component, however, is not nearly as homogeneous as the along-shore one.

4.4.4 Dispersion

While the last section presented Eulerian flow fields from drifter data, I concentrate here on the mixing which the fluctuating motion causes. Hence, I now view the drifters as quasi-Lagrangian particles and will describe how they disperse. In order to perform such an analysis one must assume that the turbulence of the flow is stationary and homogeneous. Stationarity of the flow field is essential, since only then can I replace ensemble averages by time averages (Chatwin and Allan, 1985). With homogeneous turbulence I mean that the velocity field is locally homogeneous, i.e., the mean velocity shear is constant (Monin and Yaglom,

1975). Both assumptions must be tested. Freeland et al. (1975) for example found that drifters from the Mid-Ocean-Dynamics-Experiment (MODE) described an inhomogeneous eddy field. Thus they could not rationally apply the theory of Taylor (1921) to describe the mixing of drifting particles in the ocean (Brink et al., 1991). Colin de Verdiere (1983) and Krauss and Böning (1987) released drifters in the North-Atlantic and found that Taylor's theory described their dispersion well. They then computed dispersion coefficients which quantify the mixing the eddy field causes. Davis (1985b) and Garrett et al. (1985) estimated mixing coefficients for the coastal ocean off California and Labrador, respectively. In the following I will closely follow the analysis of the above authors and refer the reader to them for a discussion of the method. I will, however, briefly sketch out the theory, in as much as it is necessary for the discussion of the results. I conclude with dispersion coefficients for the coastal current.

The mean square variance of a drifter displacement for a stationary and homogeneous turbulent flow field is (Hinze, 1975, p.48)

$$\langle x'^2 \rangle = 2 \langle u'^2 \rangle \int_0^t (t-\tau) R(\tau) dt$$

where

$$x = \langle x \rangle + x'$$

$$u = \langle u \rangle + u'$$

are displacement and velocity components, respectively. The averaging

symbol $\langle \bullet \rangle$ denotes a Lagrangian ensemble average, i.e., one over many drifters deployed in a spatial domain. The Lagrangian auto-correlation function $R(\tau)$ refers to the correlation of the velocity of a given drifter at time t since deployment and some time τ later (see section 4.3.1, p.95). The dispersion of drifters will resemble a random walk for a time t long after the deployment. "Long" means here long relative to the integral time scale $T_L = \int_0^\infty R(\tau) d\tau$, i.e., for $t \gg T_L$. In analogy with Fickian diffusion one defines a constant dispersion coefficient K as

$$K = \frac{1}{2} \frac{d \langle x'^2 \rangle}{dt} = \langle u'^2 \rangle T_L$$

In fig. 4.12a I present the time evolution of the variance or dispersion $\langle x'^2 \rangle$ for the along- and the across-shore component of the displacement. After about 25 hours the dispersion indeed varies linearly with time, and the slope then determines K to be 1800 and 230 m^2/s in the along- and across-shelf direction, respectively. The last relation depends crucially upon the mean having been removed accurately from the velocity data. One way to test this requirement is to compare the translation of the "center of gravity" $\langle x \rangle$ of the entire cloud of particles with the translation due to the ensemble and time averaged current $\overline{\langle u \rangle} t$. The overbar indicates the time average. Both translations I compare in figs. 4.12b and 4.12c. Indeed, for about 45 hours the mean cluster location moves with the mean current. I thus feel confident that the results up to that time are statistically robust, while those beyond are not. The number of degrees of freedom for $t < 45$ hours is larger than 50.

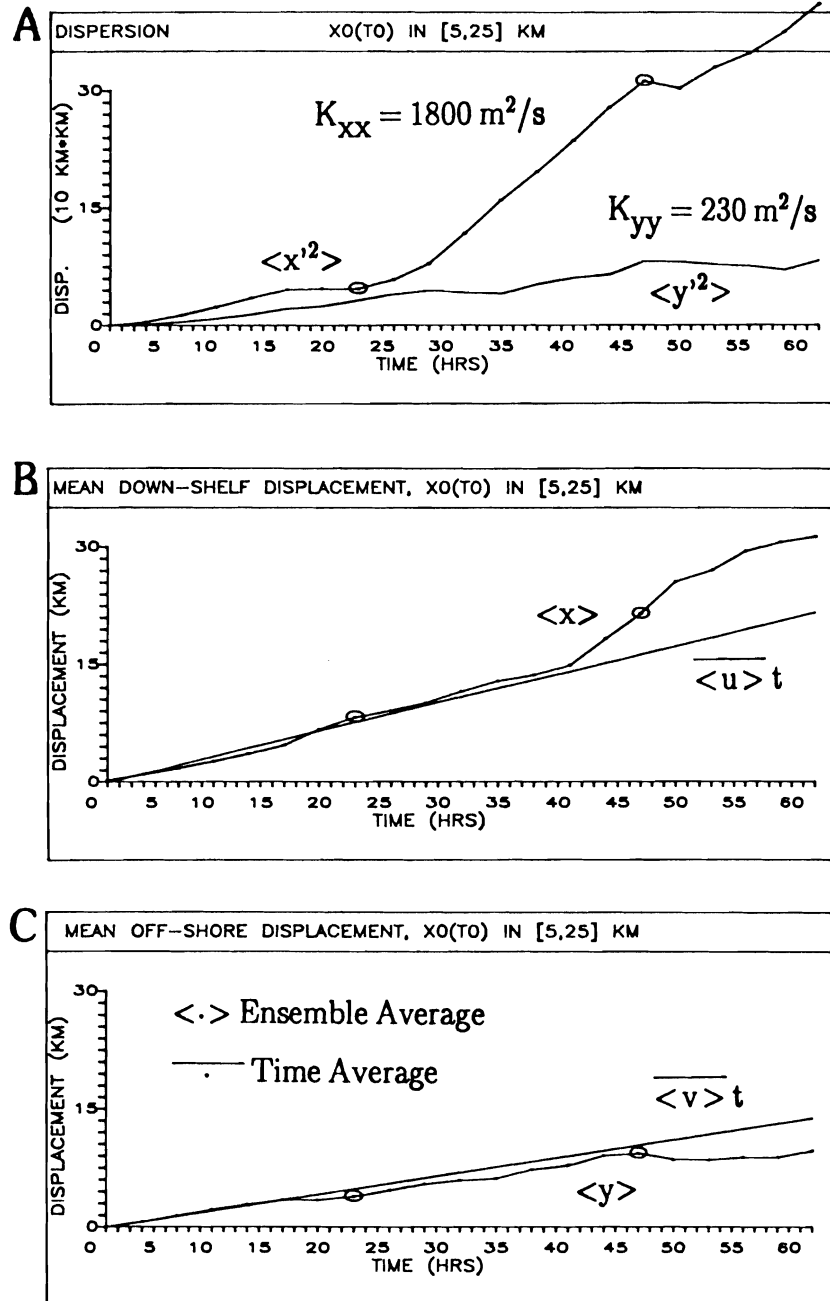


Figure 4.12. Results of drifter dispersion. (a) Drifter dispersion as a function of time after deployment and the derived dispersion coefficient in the along-shore (K_{xx}) and across-shore (K_{yy}) directions, respectively; (b) mean along-shelf displacements of drifter ensembles with time after deployment; the straight line is the displacement due to the time and ensemble averaged speed; (c) as (b) but for the across-shore displacements. The statistics are robust for about the first 40 hrs.

An approximation T_D of the Lagrangian integral time scale T_L appeared twice in the above discussion. The decorrelation time scale T_D that I used above to determine the degrees of freedom is not the Lagrangian integral time scale T_L (Tennekes and Lumley, 1972; Davis, 1985b) which is the integral of $R(\tau)$ over all lags τ . The large sidelobes of $R(\tau)$ in fig. 4.9 are suggestive of oscillatory flow (Krauss and Böning, 1987; Garvine et al., 1989) and prevent me from computing T_L directly. Since I now know the dispersion coefficient K , however, I can estimate T_L from

$$T_L = \frac{K}{\langle u'^2 \rangle} = (24, 3) \text{ hours}$$

for the along- and across-shelf directions. While the very short across-shore time scale is probably a result of the poor estimation of the across-shelf dispersion coefficient, the Lagrangian integral time scale along the shelf agrees well with the Eulerian time scale. Following Davis (1985b) I can then conclude that the flow field is linear, since Eulerian and Lagrangian integral time scales are similar.

4.5 Ekman Dynamics

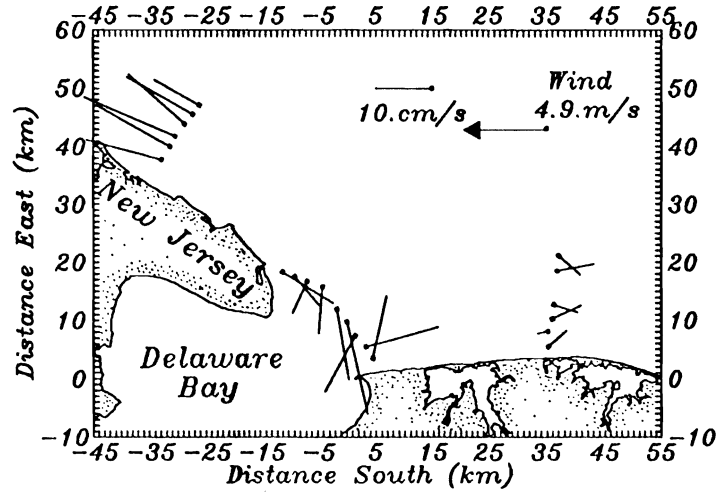
In June 1989 we profiled the inner continental shelf with shipboard instruments during strong upwelling favorable winds. I will here study the response of the coastal ocean to these winds. Upstream of the estuarine mouth buoyancy forcing is weak and the local winds dominate the dynamics.

Downstream, however, both the wind and estuarine buoyancy fluxes induce circulation.

The difference in the flows upstream of the estuary (off New Jersey) and downstream (off Delaware) is striking (fig. 4.13). Despite the winds being similar, currents near the surface upstream and downstream of the estuary move in the opposite direction along-shore. In the absence of buoyancy forcing (off New Jersey) the flow 5 m below the surface is along-shore in the direction of the wind. Speeds reach 20 cm/s. In the presence of buoyancy forcing (off Delaware) the flow at the same depth is along-shore also, but opposes the wind. Speeds never exceed 5 cm/s. The flow 9 m below the surface differs as well for the upstream and downstream regions. Upstream the current vector rotates counter clockwise with depth and the flow is onshore. Downstream no rotation of current vectors with depth is apparent, but the along-shore current against the wind strengthens with depth. Below, I explain these features with Ekman dynamics due to surface and bottom stresses in the presence or absence of a buoyancy driven coastal current.

The ADCP measures currents from 5 m below the surface downward. Hence, in water only 20 m deep we obtain no current information from the top 25% of the water column. Successive mapping of the surface salinity field, however, indicates advective processes near the surface. During the strong winds we profiled the plume region twice. The

109
Currents at $z=-5$ m
ADCP Profiling
Julian Day 166-169



Currents at $z=-9$ m
ADCP Profiling
Julian Day 166-169

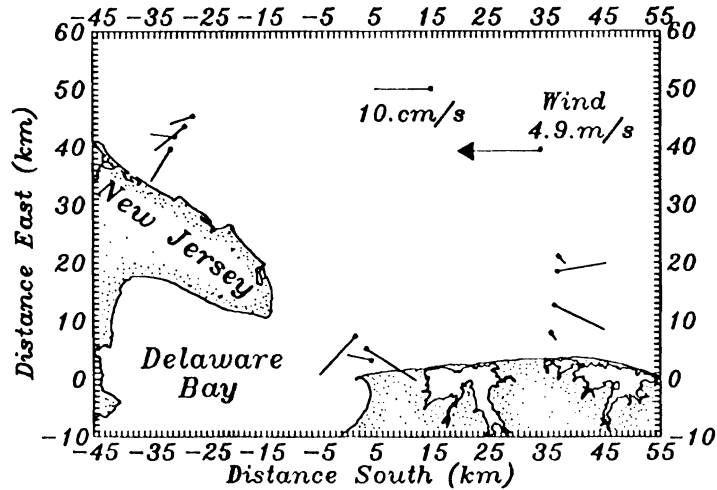


Figure 4.13. Maps of ADCP surface and bottom current vectors. Subtidal currents in June 1989 are from at 5 m and 9 m below the surface. Off New Jersey note the cyclonic turning of current vectors toward the bottom. Off Delaware currents oppose the wind. Wind vector is shown in upper panel.

first map represents the salinity field at the onset of the upwelling favorable winds, while the second map we completed 3 days later near the conclusion of the same wind event. The first map (June 13/14, fig. 4.2d, p.74) shows an almost rectangular plume with across- and along-shore dimensions of 30 km and 40 km, respectively. A vertical section across the plume (fig. 4.14a, see fig. 1.1, p.8, for the location of transect C) shows higher salinities near the surface close to the shore. I find buoyant waters at depths above 15 m. Below this depth I find ambient shelf waters. Three days later (June 16/17, fig. 4.2e, p.74) buoyant plume waters ($S < 29.5$ psu) appear to fill the entire study area near the surface except near the shore where I observe the highest surface salinities of the study area. Comparing the two maps I conclude that the near shore plume waters moved offshore as they responded to the surface currents. Inshore they are then replaced by heavier waters from either downstream or the bottom. I exclude an upstream source of salty waters as there the buoyant outflow always dominates the circulation (see fig. 4.2, p.74). The second salinity transect (fig. 4.14b) shows that deeper, ambient shelf waters ($S > 32$ psu) do not reach the coast but apparently mix with the plume waters. Consequently, I now find the strongest slopes of isolines below a depth of 10 m. There I now observe the strongest downstream currents (fig. 4.13b). This implies that the current adjusts to the internal mass field (thermal wind). Thus the wind homogenizes only the top 5 m but leads to an increase in the vertical stratification below that depth as an "Ekman" like current response tilts isolines into the horizontal.

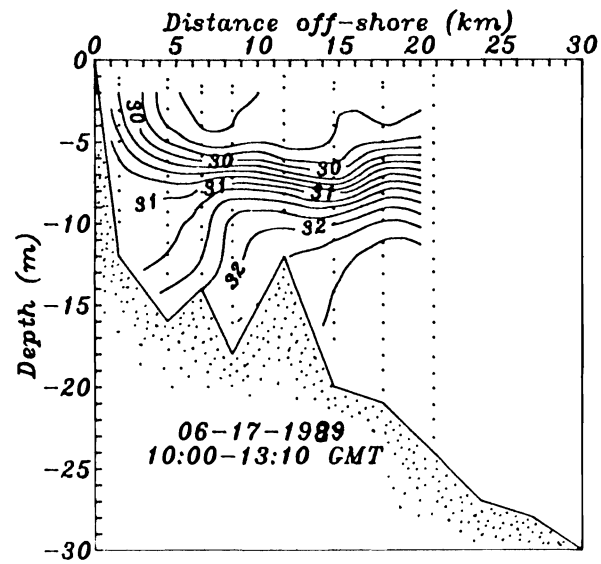
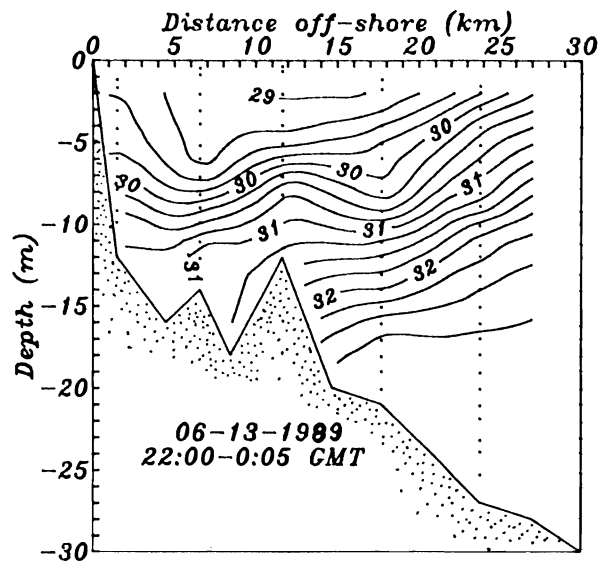


Figure 4.14. Salinity distribution on transect C. See fig. 1.1 (p.8) for location. Data are from near the onset of upwelling favorable winds (06-13-1989) and near their conclusion (06-17-1989).

In the absence of buoyancy forcing (off New Jersey) the winds force an onshore flow at depth and thus bring cold and saline shelf waters toward the coast (fig. 4.13). Not so off Delaware where buoyancy forcing is strong. Some mixing of plume and ambient shelf waters at depth, though, is the most likely cause of the strongly sloping isohalines (and thus currents) at depth. Next I will focus on the dynamics more directly by computing velocity profiles from Ekman theory.

Pedlosky (1986, p.361) states that stratification can be ignored in Ekman layer dynamics as long as

$$E_v = \left(\frac{\delta_e}{D} \right)^2 < O\left(\frac{\epsilon}{S} \right)$$

where the vertical Ekman number E_v is the squared ratio of the Ekman layer depth δ_e and the water depth D , while ϵ and S are the Rossby and Burger numbers of the flow. In the plume region both ϵ and S are much smaller than 1 (section 4.7, p.129), i.e., the flow is linear, rotation is important, and the internal deformation radius is smaller than the geometric length scale of the flow. The ratio of ϵ and S , however, varies between 0.5 and 3 and is thus always $O(1)$. Hence, as long as $\delta_e < D$ I can ignore density effects in the Ekman layer dynamics.

Following Ekman (1905) I assume a homogeneous fluid of constant depth which is set into motion by a surface wind stress. In the presence of a

coast an across-shelf pressure gradient is likely to result. To accommodate the pressure gradient I assume with Ekman (1905) a constant surface slope across the shelf. This is not unreasonable if one considers the dynamics of a small fraction of the shelf only, say the inner shelf between the 30 m isobath and where $\delta_e < D$. I further assume that the velocity field consists of the sum of a surface Ekman layer flow (u_s, v_s) due to the wind stress and a bottom Ekman layer flow (u_b, v_b) due to the geostrophically balanced surface slope and bottom stresses, i.e.,

$$(u, v) = (u_s, v_s) + (u_b, v_b).$$

I indicate vertical derivatives by a prime dash •'. I write the governing equations (Ekman, 1905) for simplicity in a co-ordinate system where the y-axis is the direction of both the coast and the wind, i.e.,

$$\begin{aligned} f u_s &= A v_s'' & -f v_s &= A u_s'' \\ f u_b &= A v_b'' & -f v_b &= A u_b'' + g \tan(\alpha) \end{aligned}$$

where α is a constant across-shelf surface slope that is undetermined at this point. As boundary conditions I choose at the surface $z=0$

$$\begin{aligned} u_s' &= v_b' = u_b' = 0, \\ v_s' &= \tau / (A\rho) \end{aligned}$$

and at the bottom $z=-D$

$$u_s = v_s = u_b = v_b = 0$$

where A is a constant eddy viscosity, f the Coriolis parameter, g the gravity acceleration, and τ the surface wind stress. The requirement of zero flux perpendicular to the coast, i.e.

$$\int_{-D}^0 u \, dz = 0,$$

however, will determine the slope α .

The analytical solution is quite complicated algebraically (Ekman, 1905) and is not repeated here. Mitchum and Clarke (1986) relax the boundary conditions at the bottom by allowing $(u_b, v_b) = -(u_s, v_s)$ at $z=-D$. The same authors provide solutions for water depth, eddy viscosity, and pressure gradients that vary across the shelf. Then, however, they have to resort to Fourier transform methods after applying many approximating assumptions. In order to keep the discussion as simple as possible, I here consider vertical variations only.

In solving the above equations I actually allow, as Ekman (1905) did, the coast and the wind stress to be inclined at any angle. During our

ADCP profiling, however, the direction was only 6° toward offshore relative to the coastline. The wind stress on June 18, 1989 reached 0.1 N/m^2 . The water depth I take as 15 m. In fig. 4.15 I depict the solution off the New Jersey coast for E_v equal to 0.4, 0.6, and 0.8. I show the velocity profiles for each component with depth (figs. 4.15a and 4.15b) as well as the hodograph (fig. 4.15c). The latter includes a sketch of the coast and the wind vector. Current magnitude and direction of model and data are similar. Even though the surface stress drives the system, the weak counter-clockwise rotation with depth indicates that bottom friction dominates in the sense that the surface stress acts mainly to set up a pressure gradient force. The model fails, however, to explain the strong onshore flow at depth even though the shape of the curve for $E_v=0.4$ appears similar to that of the data. Hence I observe a barotropic onshore flow of about 5 cm/s which I cannot explain with Ekman layer dynamics alone. In chapter 5 (p.133) I will return to this onshore flow in a different context. There I find an along-shore pressure gradient that can explain the onshore flow.

In summary, even though the agreement between model and data is poor, the predicted vertical current structure agrees at least qualitatively with observations. This is remarkable considering the simplicity and vintage of the model. The Ekman numbers I used imply vertical viscosities between $40 \text{ cm}^2/\text{s}$ and $80 \text{ cm}^2/\text{s}$.

Repeating the calculation for the currents off Delaware (slightly

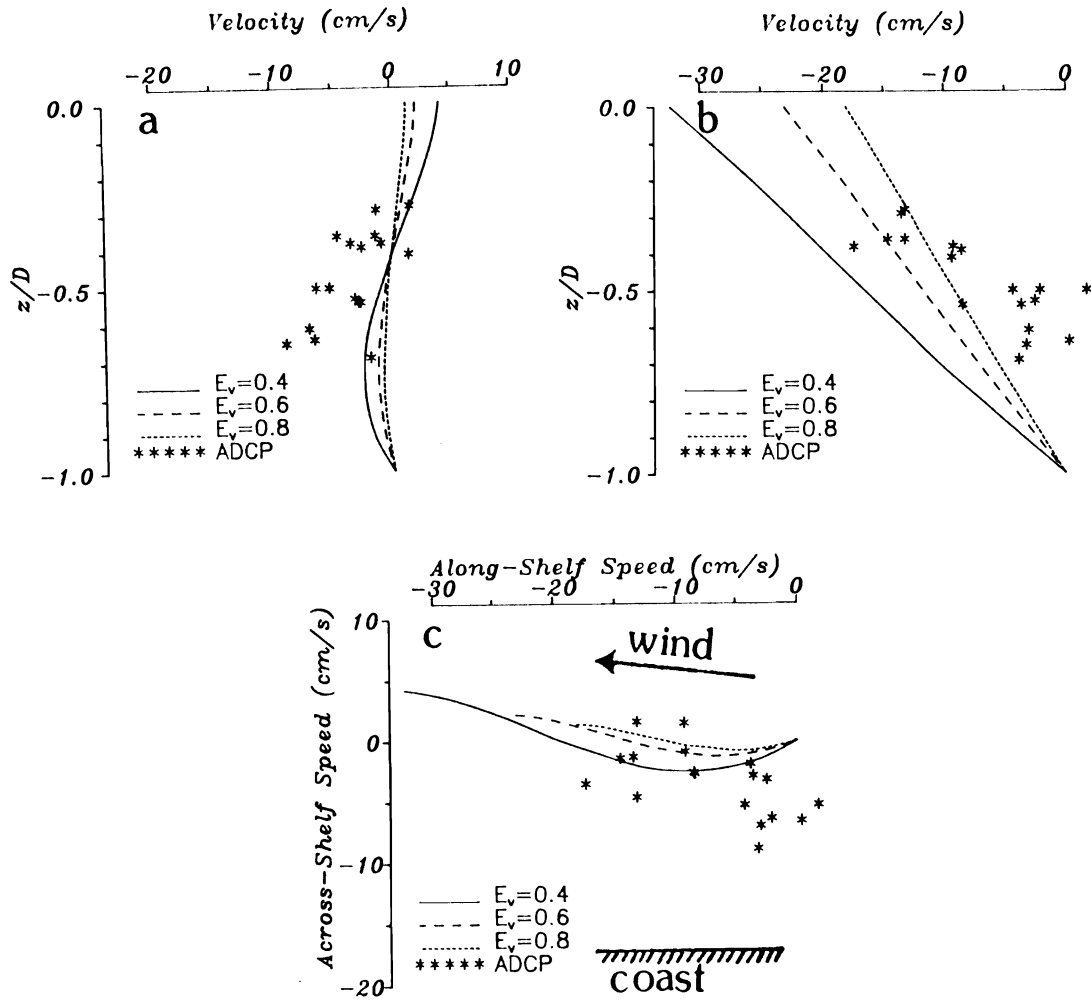


Figure 4.15. Comparison of Ekman with ADCP currents. Observations are from ADCP stations off New Jersey. The predicted velocity profiles from Ekman dynamics I show for three different Ekman numbers, namely $E_v = (0.4, 0.6, 0.8)$. (a) Across-shore velocity component; note that the onshore ADCP currents are about 5 cm/s stronger than predicted; (b) along-shore speed; (c) current hodograph, wind direction, and sketch of the coastline.

different wind and inclination of the coast) for $E_v=0.6$, and subtracting the solution from the ADCP currents, I arrive at fig. 4.16. This figure now represents the vertical profile of the along-shore buoyancy driven coastal current. As one expects for a baroclinic current which is almost in geostrophic balance, largest downstream currents occur near the surface and decrease with depth. Comparing this profile with ADCP currents in April, when the along-shore winds were light (<1 m/s), I find similar current magnitudes and vertical shears (fig. 4.16). I conclude that Ekman dynamics explains much of the observed variability of the coastal current due to wind forcing.

In this section I first discussed observations of the inner shelf response to strong upwelling favorable winds. In the absence of buoyancy forcing classical Ekman dynamics explains much of the vertical current structure. Currents are offshore near the surface, upstream at mid-depth, and onshore at depth. The Ekman layer depth δ_e is comparable to the total water depth, i.e., $E_v=O(1)$, but smaller than 1. In the plume region where buoyancy forcing is strong, ADCP current profiles in the absence of wind forcing (April) compare favorably with those during strong winds (June) when the Ekman currents are subtracted from them. The success of this very simple model implies that buoyancy and wind forced motion superpose linearly in the plume region. Vertical eddy viscosities of the flow in waters 15 m deep appear to be about $50 \text{ cm}^2/\text{s}$, i.e., δ_e is about 10 m.

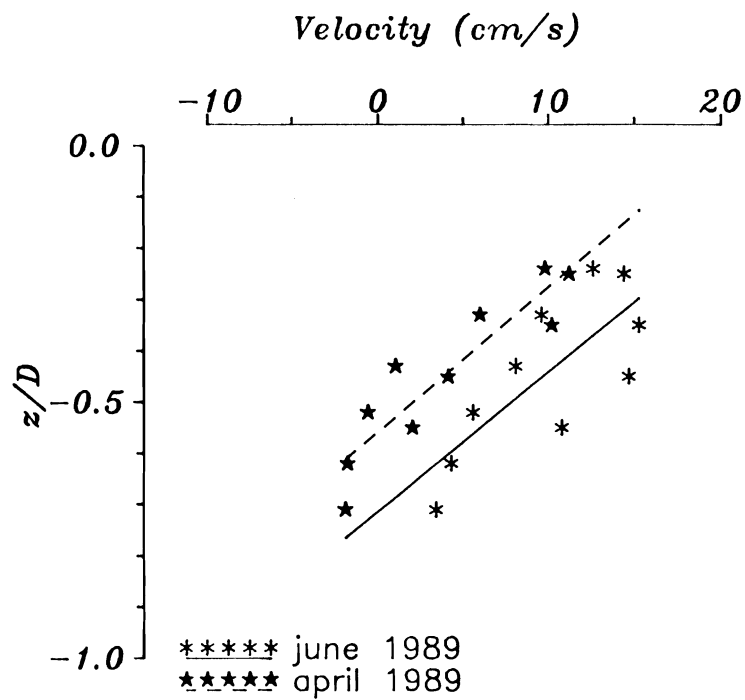


Figure 4.16. Vertical current profiles from ADCP data. Data collected in April and June 1989. Ekman currents have been removed ($E_v=0.6$) from the June data. I show only the along-shore velocity component.

4.6 Semi-Geostrophic Dynamics

The purpose of this section is to firmly establish that the flow in the plume region approaches a semi-geostrophic balance. Hoskins (1975) coined the phrase "semi-geostrophic" to describe dynamics that are geostrophic in one direction only. Such balances are common on continental shelves where along-shore scales often exceed across-shore ones. I will find that the across-shelf momentum equation is almost geostrophic while many terms contribute to the along-shelf momentum balance where pressure gradients as well as surface and bottom stresses are important.

In fig. 4.17a I show the subtidal density distribution of transect C (see fig. 1.1, p.8, for location) for April and June. From these I compute geostrophic (thermal wind) speeds (fig. 4.17b) in order to compare them with the observed ADCP currents (fig. 4.17c). All properties I first deduced by the method outlined in section 3.5 (p.41). The integration constant for the thermal wind relations I choose as the ADCP velocity estimate closest to the bottom. The agreement of currents as well as their horizontal and vertical distribution is remarkable in the absence of wind (April) and reasonable in its presence (June). Both the location of the jet and its speed are very well reproduced by the thermal wind calculations of currents in April. In summary I conclude that the internal mass field balances the along-shore current shear through geostrophy.

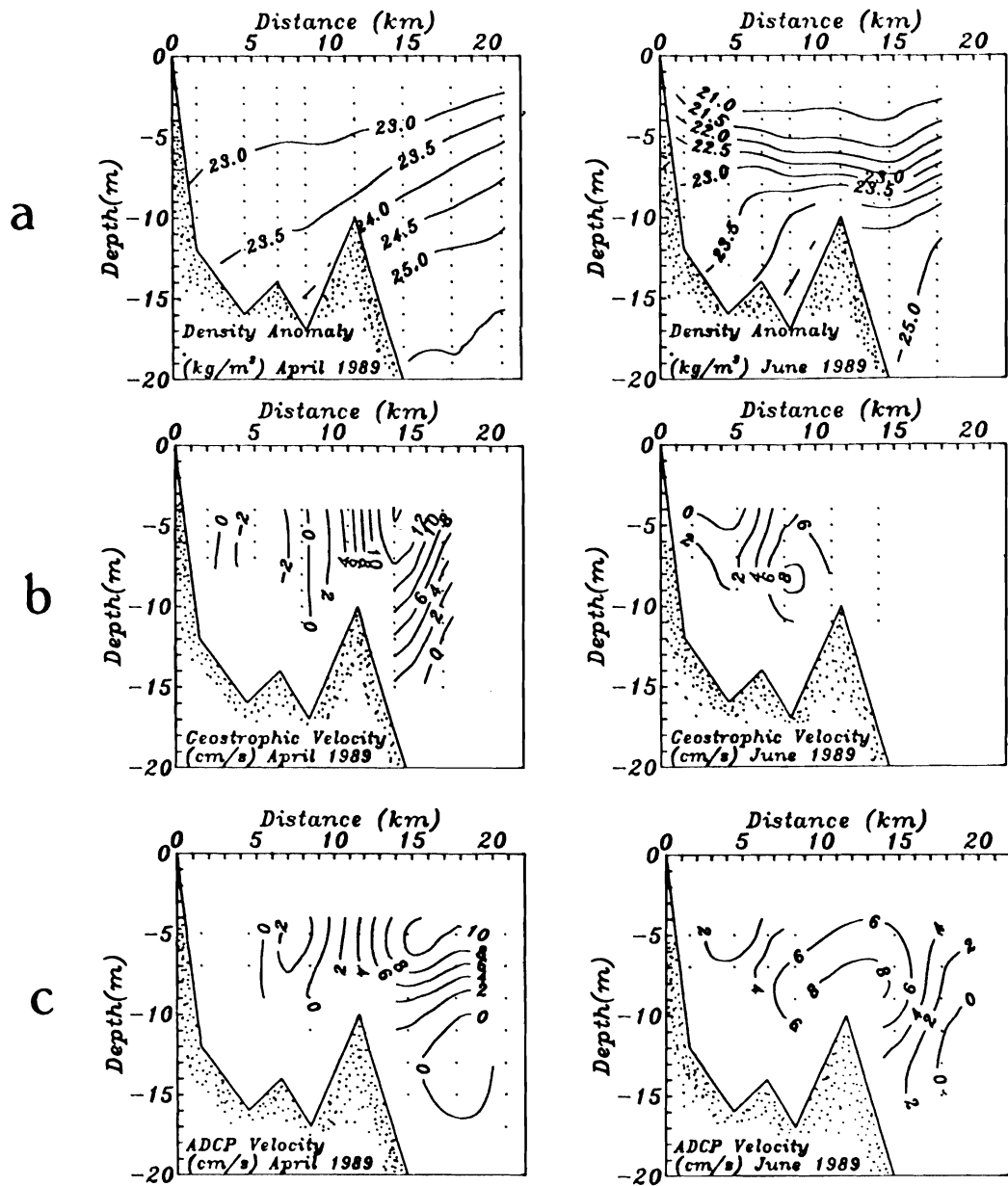


Figure 4.17. Thermal wind diagnostics for April and June 1989. (a) Density anomaly; (b) thermal wind speeds normal to the transect; (c) ADCP speeds normal to the transect.

Along-shore winds, however, impose forcing too. Next I analyze this by estimating terms in the along-shore momentum balance from time series data. After introducing an approximate, depth-averaged form of the momentum equation, I discuss the difficulties of estimating the terms in it, present my results, and conclude that pressure gradients, surface stresses, and bottom stresses all contribute to the along-shelf momentum balance.

The depth averaged along-shore momentum balance reads

$$\partial_t u - fv + g \partial_x \eta - \tau_s / H + u / H \left\{ \begin{array}{c} r \\ C_D |u| \\ C_d(t) |u| \end{array} \right\} = 0$$

where the terms that I will estimate are local acceleration, Coriolis force, pressure gradient, and surface and bottom stress. The last term (bottom stresses) I present in three different forms that become clear below. In estimating the above terms I borrow from work by Masse (1988) and refer to that study for a careful discussion on the estimation techniques. I neglect nonlinear advective terms and a baroclinic pressure gradient. Further below I will present a momentum balance from shipboard data where I find that nonlinear advection is negligible. The baroclinic pressure gradient, however, can become sizable when instabilities disrupt the plume region.

The only term that I measure and estimate without difficulty is the local acceleration $\partial_t u$, but ironically, this term is generally small and often

negligible. Estimation of the Coriolis term $-fv$ appears straight forward, but is not. This term depends crucially on the definition of the across-shore direction. Here I chose the orientation of the semi-minor principal axis as that direction.

The along-shore pressure gradient term $\partial_x \eta$ (or $\delta\eta/\delta x$ in finite difference form) is most troublesome to measure, especially without bottom pressure sensors. I here utilize data from coastal tide gauges to approximate pressure gradients. Then, however, one does not know the absolute or mean pressure gradients and I thus use only band-pass filtered data in the analysis. Another more serious problem relates to the computation of gradients that involve differencing along the shelf. Which finite distance δx is the best one to estimate $\delta\eta/\delta x$ from noisy sea level records? Often an implicit scale assumption enters instead of a clear answer to that question (Lentz and Winant, 1986). Here I follow Masse (1988) who fitted a polynomial to many coastal sea level observations along 1000 km of coastline with the method of least squares. She then differentiated the polynomial at each time step at the point of current observations and thus obtained good and smooth estimates of $\partial_x \eta$. As suggested by Masse (1988) I use a third order polynomial to reduce the noise in the pressure gradient estimation.

The surface stress term τ_s/H incorporates the exchange of momentum between the atmosphere and the ocean at the air-sea interface. Here I estimate the surface stress from oceanic observations of wind speed

and direction as well as from the temperature difference between the air and the sea. The air-sea temperature difference incorporates the effects of thermal stratification on the exchange of momentum (Smith, 1988) from the atmosphere to the ocean.

The last term in the momentum balance, the bottom stress, always depends on poorly known drag coefficients. I study three different frictional "laws," namely a linear and a quadratic one with constant coefficients r (in cm/s) and C_D , respectively, and a sophisticated scheme that implies a time dependent drag coefficient $C_d(t)$. The time dependent drag coefficient $C_d(t)$ represents wave-current interactions (Grant and Madsen, 1979). Surface gravity waves in shallow water impose orbital wave velocities near the bottom that enhance the bottom roughness for the low frequency current. Grant and Madsen (1979) devised an iterative algorithm to compute the enhanced bottom stresses. Ideally, one needs the dominant wave height, period, and direction of propagation. As I have time series of only the former two variables, I assume that the waves and the currents are collinear.

Close to the shore off New Jersey I collected a 3 month long record of currents 3 m and 7 m above the bottom in water that is 13 m deep. I choose the data from this mooring (A1, see fig. 4.5, p.85, for location) for the subsequent analysis because the record is long, I have two current meters in the vertical, and buoyancy forcing is generally weak. The following discussion is then more typical of the ambient shelf and I expect the

dynamics to be somewhat simpler than it is in the plume region where buoyancy forcing contributes at all times. As it will turn out, however, even in the absence of a permanent coastal current the momentum balance remains unclear, as I cannot find a closed balance in the along-shore direction.

I first compute root mean square (RMS) values from the time series data as a qualitative measure of the respective size of terms. I list in table 4.4 the RMS values of each term for three different frequency bands and friction "laws." For any experiment the residual, unbalanced momentum term constitutes about 25% of the sum of the absolute magnitudes of all terms entering the balance. Only the balance that uses Grant and Madsen's (1979) friction "law" performs consistently worse, as the residual is 40% of the total momentum. The major conclusion, however, is the same for each friction "law." Pressure gradient and surface stresses are the largest terms followed by bottom friction and Coriolis forces. The residual, too, is always a major term, i.e., the balance never closes. In a similar study nearby Masse (1988) describes similar results and uncertainties.

For a more quantitative analysis of two particular balances I depict in fig. 4.18 the time series of all terms as well as the residual. The data are band-pass filtered with cut-off periods near 5 and 10 days. I choose the bottom drag coefficient $C_D=0.0025$ (fig. 4.18a) and the bottom resistance coefficient $r=0.05$ cm/s (fig.4.18b). The dominant terms in fig. 4.18a

Table 4.4. Along-shelf momentum balance off New Jersey. I analyse the data from station A1 at three different frequency bands and distinguish between motions at periods larger than 10 days (T_1), between 5 and 10 days (T_2), and between 1 and 5 days (T_3). The table gives the root mean square values for each term and the residual as averaged over the entire time series. All units are 10^{-5} m/s^2 , $r=0.05 \text{ cm/s}$, $C_d=0.0025$, $H=13 \text{ m}$, and GM79 stands for Grant and Madsen (1979).

		$T_1 > 10 \text{ days}$	$T_2 > 5 \text{ days}$	$T_3 > 1 \text{ day}$	
$-\tau_s/H$		0.22	0.10	0.27	
$g \partial_x \eta$		0.31	0.13	0.39	
τ_b/H	{	(a) ru/H	0.18	0.13	0.22
	{	(b) $C_d u^2/H$	0.08	0.04	0.13
	{	(c) GM79	0.18	0.15	0.56
$\partial_t u$		0.01	0.03	0.17	
$-fv$		0.09	0.04	0.15	
Residual	{	(a) ru/H	0.20 (25%)	0.10 (23%)	0.29 (24%)
	{	(b) $C_D u^2/H$	0.17 (24%)	0.08 (24%)	0.26 (23%)
	{	(c) GM79	0.30 (37%)	0.17 (38%)	0.62 (40%)

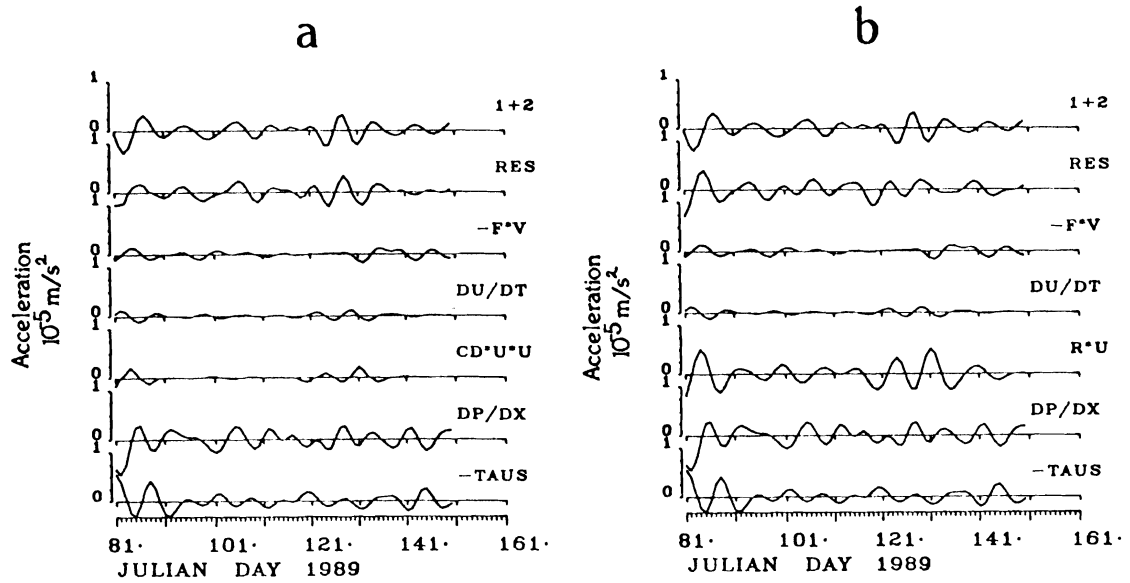


Figure 4.18. Time series of depth averaged along-shelf momentum. For the current meter mooring location A1 see fig. 4.5 (p.85). (a) Quadratic friction with $C_d=0.0025$; (b) linear friction with $r=0.05$ cm/s. From bottom to top the terms (and their labels) are:

1. surface stress ($-TAUS$),
2. pressure gradient (DP/DX),
3. bottom friction ($CD*U*U$ in (a), $R*U$ in (b)),
4. local acceleration (DU/DT),
5. Coriolis acceleration ($-F*V$),
6. residual (RES), and
7. the sum of surface stress and pressure gradient ($1+2$).

(quadratic bottom friction) are the surface stress and the pressure gradient. Both terms balance each other to some extent. All other terms, however, are small, but, except for the local acceleration term, are not negligible. The principal response then is the set-up of an along-shore slope by the local winds. Small imbalances between these two terms drive a flow that is balanced mainly by bottom friction and Coriolis forces. The momentum balance with $r=0.05$ cm/s (linear bottom friction) of fig. 4.18b tells a different story: bottom friction is now a dominant term in the balance besides surface stresses and pressure gradients. Local and Coriolis acceleration are small and negligible. The residual, however, remains as large as any of the three principal terms. Neglecting bottom stresses and small terms altogether does not affect the residual much. This result as well as the drastically different interpretations of figs. 4.18a and 4.18b are most troublesome. I will next argue that the approach of finding closed momentum balances is flawed.

As a summary of this section, I here critically discuss observational attempts to find closed momentum balances. Over the last decade many researchers attempted to estimate the balance of forces from time series of current, wind, and pressure observations (Pettigrew, 1981; Noble et al., 1983; Thompson and Pugh, 1986; Lentz and Winant, 1986; Hill and Simpson, 1988; Masse, 1988). Nevertheless, each study failed to find a closed balance, i.e., a balance where the residual is much smaller than any of the terms estimated. Most studies instead conclude that more data are

needed to close the balance, that better vertical current resolution is needed to get better estimates of depth averaged flows, that near bottom currents are needed to better compute bottom stresses, that more and better pressure sensors are needed to better compute pressure gradients, etc. But instead of also lamenting how insufficient my data are to find a closed balance, I here argue against the approach itself.

The deployment of a mooring array always implies a spatial scale assumption. Motion at scales smaller than twice the separation of two moorings will alias the observations spatially. Motion at the scale of the mooring separation will most likely occur in conjunction with pressure gradients at the same scales. These, however, are never resolved. And finally, unresolved scales are usually parameterized through empirical coefficients that can never replace the physics that affect them, that one does not understand properly, but whose effects one wishes to include nevertheless. As an example, I mention the exchange of momentum at horizontal boundaries such as those at the sea surface and the bottom. I found in this section a major balance between an along-shore pressure gradient, surface stress, and possibly bottom friction. The residual of the former two terms is as small as the residual from a balance that actually involves a flow. In closing I then argue that my momentum balance in the absence of a current is as good as in its presence. The problem is not the lack of data; the problem is the lack of understanding of relevant processes.

4.7 Discussion, Scales, and Parameters

The buoyant outflow from the Delaware Estuary forms a distinct pool of light water off the coasts of Delaware, Maryland, and beyond. A zone of enhanced lateral density gradients separates this pool from heavier ambient shelf waters. The zone of enhanced lateral density gradients extends from the surface to the bottom. I find that the distance from the coast to the maximum of this density gradient near the surface increases in the downstream direction. Both features, i.e., the zone of large density gradients and the downstream widening of the plume, distinguish the plume from the source region. In the latter I observed strong fronts and a narrow outflow. It thus appears that in the plume region diffusive processes mix ambient shelf waters with buoyant source ones. Indeed, surface drifters reflect dispersion and I generally find that while the buoyancy driven coastal current advects the drifters downstream, a wind driven, often upwelling favorable Ekman circulation displaces the same surface drifters toward offshore. Ekman numbers are $O(1)$, but are smaller than unity, i.e., Ekman layers are smaller but of the same order as the total water depth. I interpret the variable wind field as a mixing agent for buoyant waters on the shelf. Analysis of drifter trajectories in the plume region gave horizontal dispersion coefficients that are about 2000 and $200 \text{ m}^2/\text{s}$ along and across the shelf, respectively.

The temporal Eulerian mean surface flow indicates a downstream current that reaches its maximum speed of 20 cm/s about 10 km from the

coast. Current speeds decrease almost uniformly toward both the coast and off-shore. From ADCP profiling I obtain a mean subtidal volume transport of about 0.01 Sv ($10^4 \text{ m}^3 \text{ s}^{-1}$) perpendicular to a transect across the shelf. On the same transect I observe current shears $\partial_y u$ of about 0.1 f, 0.15 f, and 0.2 f as estimated from current meter, surface drifter, and ADCP profiling, respectively. The Coriolis parameter f is a measure of the planetary vorticity while, as in the last chapter, I interpret $\partial_y u$ as a good approximation of the relative vorticity. The ratio of relative to planetary vorticity is much smaller than unity in the plume region, and I therefore hypothesize that the flow there is linear and geostrophic. ADCP and CTD profiling on a transect across the plume region indeed confirms this postulate. The internal mass field balances the Coriolis force of the along-shore current, and both vertical and lateral current profiles are very well predicted by the thermal wind relations. From observations I thus conclude that in the plume region the along-shore flow is nearly in geostrophic balance with the pressure field. I argue, however, that the flow is not quasi-geostrophic, since both isopycnal displacements and topographic variations are of the same order as the water depth.

As in the last chapter I summarize the plume region in terms of nondimensional parameters. Table 4.5 lists the Froude, Rossby, and Burger numbers as well as velocity and length scales for each experiment separately and as the average over all experiments. Similar to the source region, the flow is always subcritical ($F < 1$), but in contrast both the Rossby and the

Table 4.5. Scales and parameters for the plume region.

	March	April	June	Mean
L_D (km)	1.8	6.3	10.0	6.0
L_i (km)	1.0	0.8	0.5	0.7
L (km)	10	25	25	20
S	0.03	0.06	0.06	0.05
F	0.57	0.12	0.05	0.25
ϵ	0.10	0.03	0.05	0.06
Discharge (m^3/s)	150	350	700	400
Wind (m/s)	3	1	5	

Burger numbers are much smaller than unity. In the absence of friction small Rossby numbers indicate that the flow is linear and geostrophic. They are internally consistent with the observed small ratio of relative to planetary vorticity. Small Rossby numbers are also consistent with the finding that Eulerian and Lagrangian integral time scales are similar. As the Burger number, however, is not $O(1)$, the dynamics is not quasi-geostrophic, but appears to be closer to frontal geostrophic (Cushman-Roisin, 1986; Gent and McWilliams, 1983).

CHAPTER 5: THE COASTAL CURRENT REGION

5.1 Introduction

The Hudson, Delaware, and Chesapeake estuaries impose important forcing on the inner continental shelf of the Mid-Atlantic Bight by generating buoyant outflows that evolve into plumes and coastal currents. Coastal currents may then often dominate the circulation of the inner shelf all along the Mid-Atlantic Bight from Sandy Hook, NJ, to Cape Hatteras, NC. Here I discuss the Delaware Coastal Current and the Hudson Coastal Current as observed about 80 and 150 km from their respective sources. Mixing of these buoyant waters with ambient shelf water is most likely facilitated by frequent instabilities; I introduce these below, but discuss details in the next chapter.

Our 1989 experiments seldom covered the Delaware Coastal Current region, since we underestimated its strength and along-shore extent. ARGOS-tracked drifters and satellite imagery, however, provide a first impression of the Delaware Coastal Current downstream of the plume region. This flow is the subject of the next section 5.2; it will briefly introduce the narrowness of the flow and its instabilities. Wong and Münchow (1991) describe similar data when they tracked buoyant waters more than 80 km

downstream from the mouth of the Delaware Estuary. That study, however, only speculates on the conditions upstream of the Delaware Estuary. In section 5.3 I will study the density and flow field near Atlantic City, NJ, as I observed remnants of the Hudson Coastal Current on two occasions. The buoyant water must have traveled more than 150 km downstream from its source in the Hudson/Raritan Estuary. I will discuss the morphology of this buoyant region as well as some statistics of particular events. I conclude with a discussion of scales and dynamical parameters which remain uniform along the shelf in the coastal current region.

5.2 Delaware Coastal Current

During moderately downwelling favorable winds in May 1989 we deployed a cluster of 7 ARGOS-tracked drifters. Three drifters beached within the first day, and rough seas prevented a fellow graduate student from retrieving the remaining 4 buoys. Hence they left our study area. Nevertheless, I present in fig. 5.1 the trajectories of these escaping floats. They apparently trace a strong coastal current that extends some 90 km from the source. A clear AVHRR thermal image near the end of the deployment (fig. 5.2) pictures the coastal current as a band of warm water. All drifters (fig. 5.1) we deployed within this current. Initially, speeds (not shown) are about 30 cm/s, but they increase after the current passes the slight bend in the coastline near Ocean City, MD. There speeds reach almost 50 cm/s. As in the plume region, transverse shear is such that within the

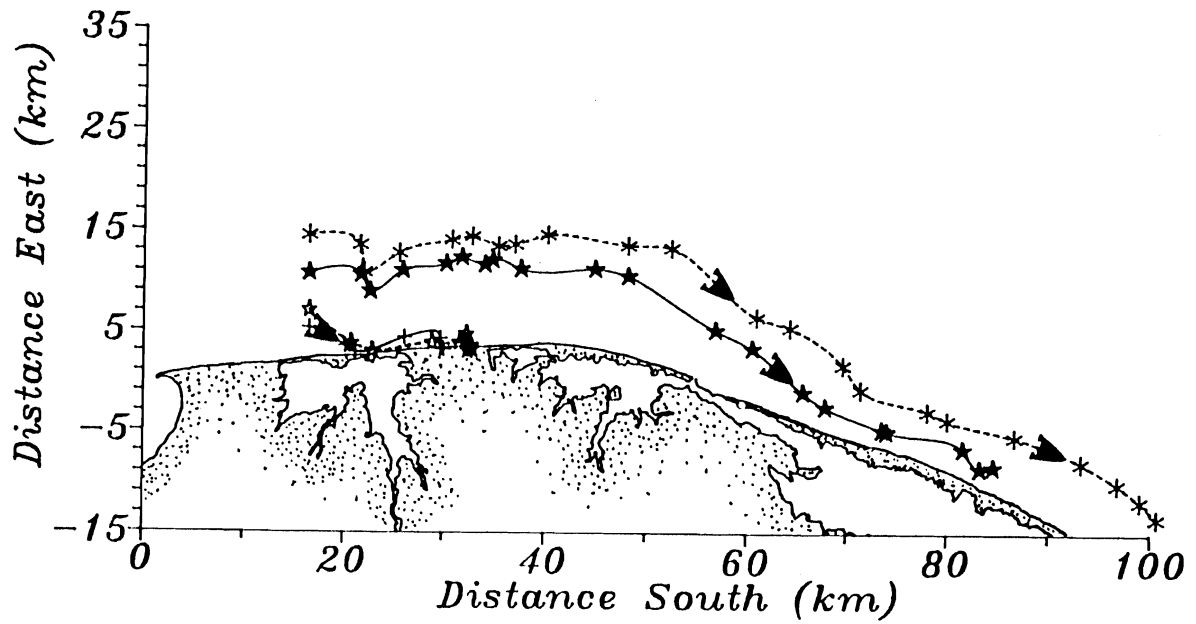


Figure 5.1. Trajectories of 4 drifters. These were deployed and retrieved during downwelling favorable winds between Julian day 136 and 139. Two inshore drifters beached the first day. The other two drifters traced the Delaware Coastal Current more than 100 km from the Delaware Bay.

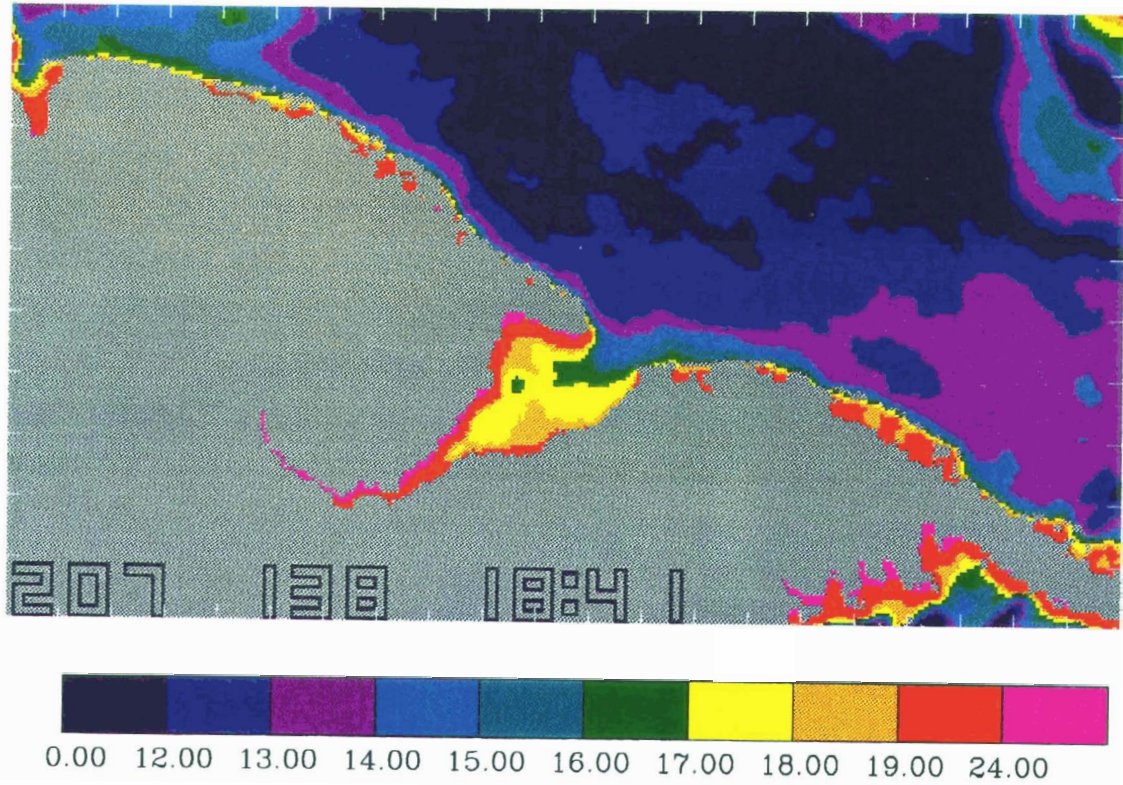


Figure 5.2. Sea surface temperature from AVHRR on day 139. Warmer water near the coast indicates the Delaware Coastal Current during downwelling favorable winds.

coastal current maximum speeds are 10 km from the shore. I speculate that the current is still frontally geostrophic, i.e., strongest currents occur where isopycnal slopes are strongest. I have no supportive hydrography, however.

Almost a year later I have both hydrography and detailed current information from underway ADCP profiling (fig. 5.3, same as fig. 4.3, p.77). Fig. 5.3a centers on the plume region, but I here concentrate on the downstream part of the figure. At the location of transect A in fig. 5.3 the plume region narrows from about 20 km to only 7 km within 4 km. Subtidal current vectors indicate a flow of about 10 cm/s with a strong onshore component which is consistent with the isohalines moving close to shore. In fig. 5.3b I depict the salinity as a function of depth and offshore distance. Largest salinity gradients I find at about 7 km from the coast. I introduce this reduction of current width as a characteristic of the onset of the coastal current region. Increasing speeds are another. The two characteristics are probably related through continuity. But what is the cause of the narrowing of the buoyant waters? As the inertial radius $L_i = U/f$, where U is a velocity scale, barely exceeds 2 km and I observe the feature more than 40 km from the source region, I exclude inertial turning as a possible process that is causing this abrupt narrowing of the buoyant waters. Instead I speculate that I observe the beginning of a first meander of an unstable coastal current.

Three weeks later we repeated the experiment, but went 40 km farther downshelf. Rough seas and time constraints prevented us from

a

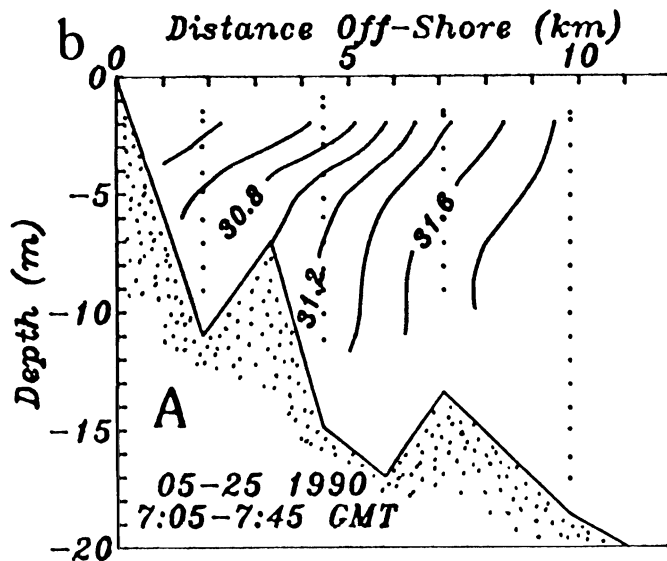
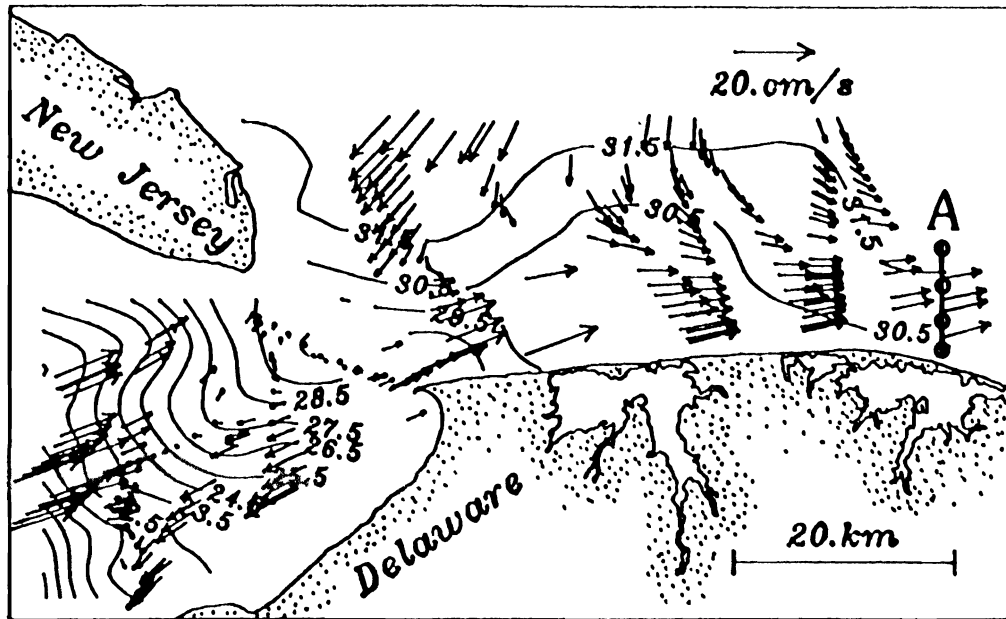


Figure 5.3. Salinity and subtidal flow field in May 1990. Shown is the transition from plume to coastal current region near the bend in the otherwise straight coastline. (a) The 31.5 psu isohaline moves from 20 km off-shore to less than 7 km off-shore within 10 km along-shore distance (from Wong and Münchow, 1991); (b) a vertical transect emphasizes the decreasing width of buoyant waters.

collecting good quality ADCP data. As in all previous surveys (see fig. 4.2, p.72), the plume in fig. 5.4a, too, widens from 10 km near the source to about 20 km near the bend of the coastline. The hydrography of this survey (fig. 5.4) lends strong support for the hypothesis of an unstable coastal current. The "wavy" pattern of isohalines near the surface starts about 30 km from the mouth of the estuary. The amplitude of the perturbation grows downstream. The "unperturbed" or "mean" position of a zone of maximum salinity gradient separates buoyant from ambient shelf waters. I tentatively draw this "mean" position as a dotted line in fig. 5.4a. The current narrows to 12 ± 4 km. The deviation of 4 km represents the amplitude of meanders which have a wavelength of about 16 km. The internal deformation radius is about 8 km.

In fig. 5.4b I show salinity transects across the shelf from the same mapping survey in June 1990. In each transect I find the maximum salinity gradient about 10 km from the shore; however, the gradient itself undergoes dramatic changes. In transect A the gradient is almost constant, but in transect C it resembles a classical front. The strong front extends from the bottom to the top of the water column. Farther downstream yet (transect D) I encounter the puzzling phenomenon of a single front (transect C) splitting into two (transect D). Wong and Münchow (1991) present these data qualitatively but do not offer an explanation. Here I speculate that instability processes deform the front without disrupting it. Garvine et al. (1988) report on such frontal instabilities near the shelf break.

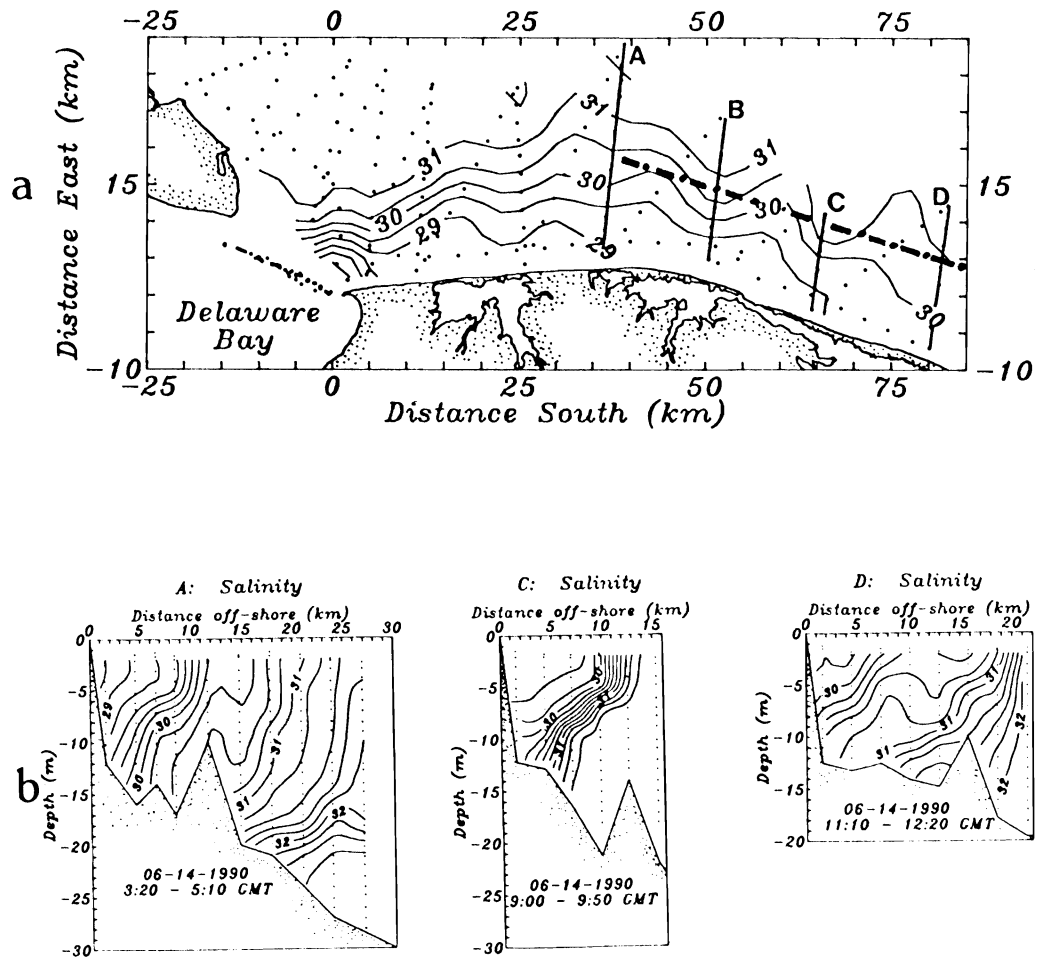


Figure 5.4. Salinity field in June 1990. Pronounced meanders are visible in the map of surface salinity (a). Salinity transects (b) indicate that buoyant waters extend to the bottom. The changes in width of the current along the shelf are suggestive of an unstable coastal current.

In summary, the Delaware Coastal Current extends more than 80 km along the shelf off Delaware, Maryland, and Virginia. Maximum gradients occur about 10 km from the coast. The flow appears to become unstable roughly at the location of a slight bend in the coastline. Stern and Whitehead (1990) study barotropic instability processes that a bent coastline introduces on a coastal current. This coastal current, however, is baroclinic and it is not clear if that study applies here.

5.3 The Hudson Coastal Current

5.3.1 Introduction

The Hudson River discharges about the same amount of freshwater into the coastal ocean as the Delaware River. Hence, it is no surprise that the onset of a buoyancy driven coastal current appears similar too. In fig. 5.5 I reproduce the surface salinity distribution near the mouth of the Hudson as well as a transect across the plume over the inner shelf off northern New Jersey (from Bowman and Iverson, 1978). Dominant features, such as a widening plume and an undulating front are by now familiar features of coastal currents in formation. In this section I will show that Hudson plume water can travel 150 km downstream from its source, thus extending along the entire shore of the state of New Jersey. I detected these buoyant waters with a mooring array just 20 km upstream from the mouth of the Delaware Estuary and with shipboard instruments. In the next section I

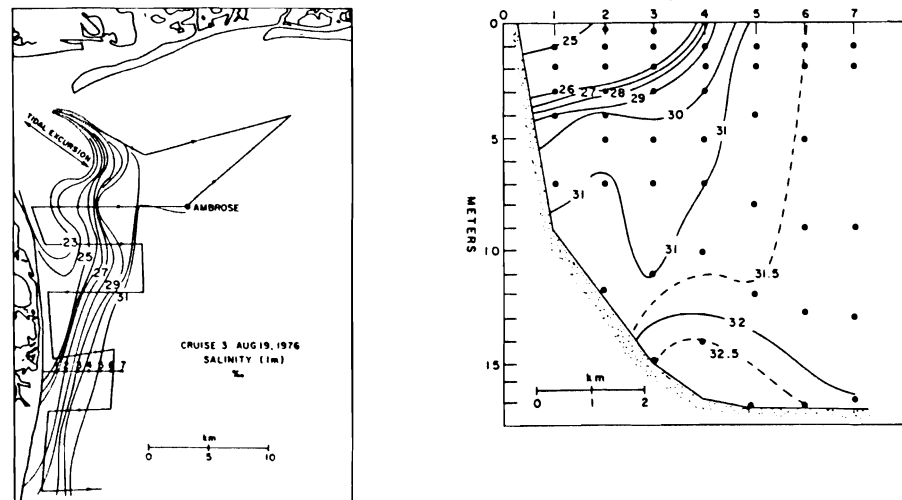


Figure 5.5. Plume of the Hudson River near its source. (a) surface salinity distribution; (b) salinity transect about 20 km from the mouth of the estuary. Data from August 1976 (from Bowman and Iverson, 1977).

will first provide strong evidence that light waters off southern New Jersey originate from the Hudson River upstream rather than the Delaware Estuary which is close by but downstream. Thereafter I study data from time series of current, salinity, and freshwater discharge in order to establish statistical relations between upstream discharge of freshwater and downstream response.

5.3.2 Morphology

In June of 1989 we obtained the three dimensional hydrography of buoyant waters just downstream of Atlantic City, NJ with shipboard instruments. We resolved the advance and retreat of a tongue of Hudson water. Fig. 5.6 clearly shows a low salinity pool upstream on day 165 along with two vertical salinity and temperature transects. One transect (fig. 5.6b) cuts through the pool of Hudson water while the second (fig. 5.6c) is just downstream of the pool. Warm, low salinity waters extend almost to the bottom near the shore (fig. 5.6b) while downstream (fig. 5.6c) warm, but saline waters occupy only the upper 10 m of the water column. In both transects, however, isohalines slope upward with distance from the shore. Thermal wind calculations imply velocities of the order of 10 cm/s downstream. Three days later slopes of isolines and current directions will have changed due to strong upwelling favorable winds on day 167. In figs. 5.6a and 5.6c I also mark the positions of the S4 current meters whose records I discuss next.

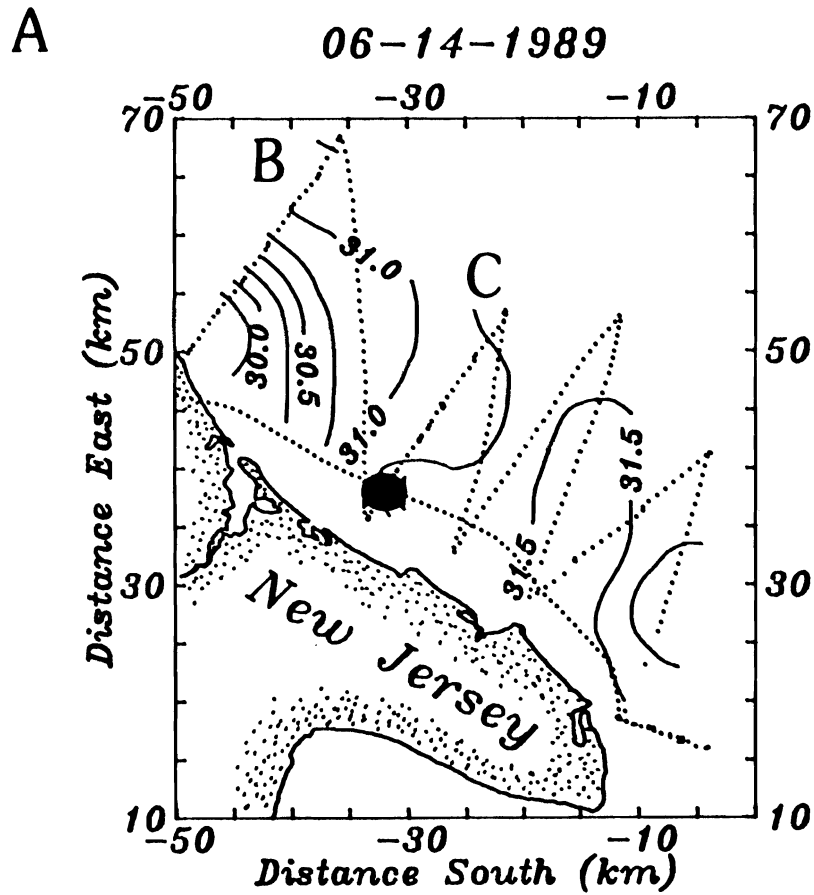


Figure 5.6. Hudson Coastal Current 06-14-1989. Locations of buoyant waters are more than 150 km downstream from the Hudson River: (a) Map of surface salinity that shows a tongue of buoyant water upstream; I label two transects B and C; (b) salinity (left panel) and temperature (right panel) for transect B; (c) as (b), but for transect C. Filled circles in (a) and (c) indicate the location of current meters A1 and A1B 6 m and 10 m below the surface, respectively. Note that very cold waters ($T < 12\text{ }^{\circ}\text{C}$) are below buoyant coastal current waters ($S < 31.5\text{ psu}$).

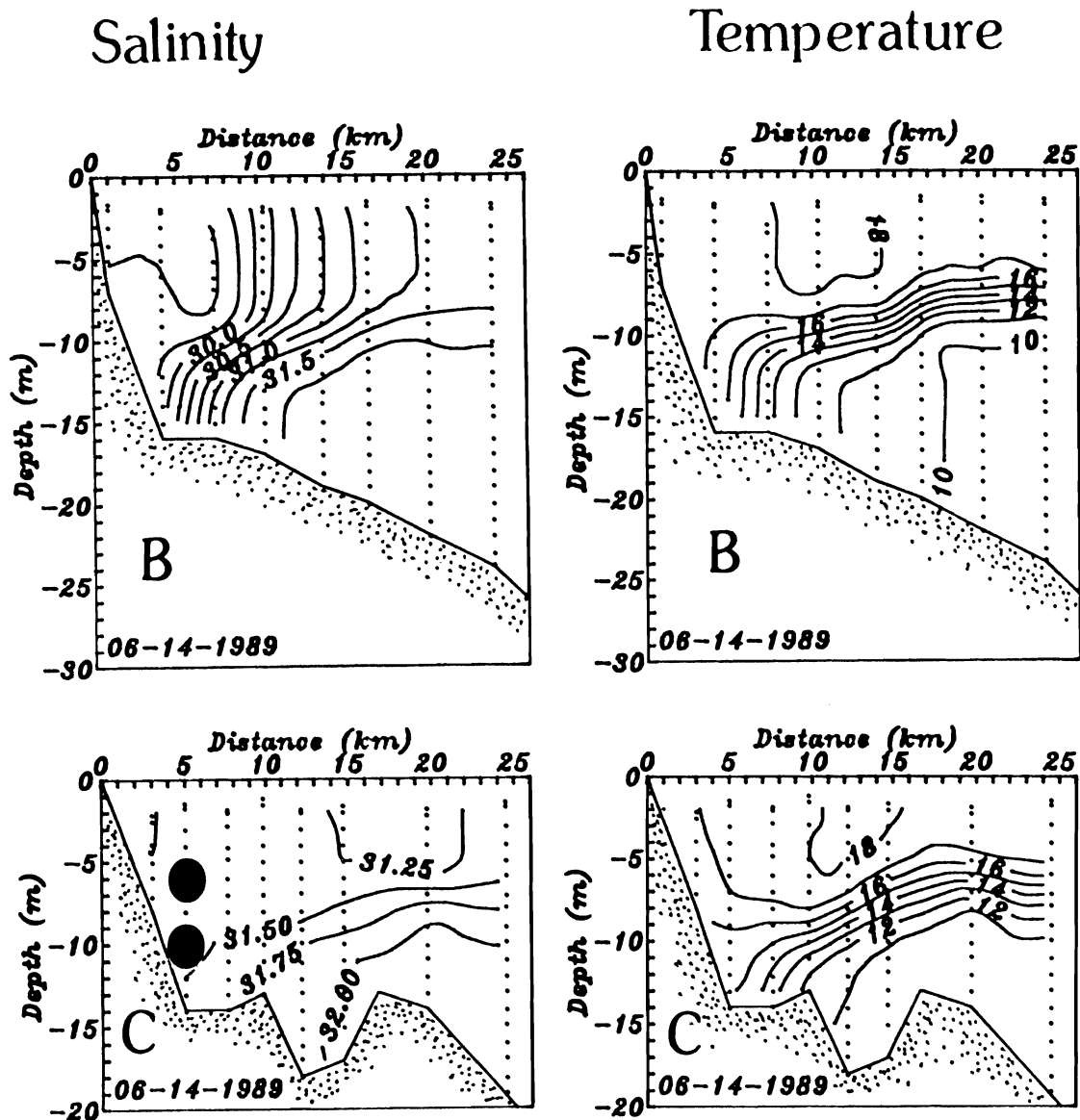


Figure 5.6. Hudson Coastal Current 06-14-1989. Locations of buoyant waters are more than 150 km downstream from the Hudson River: (a) Map of surface salinity that shows a tongue of buoyant water upstream; I label two transects B and C; (b) salinity (left panel) and temperature (right panel) for transect B; (c) as (b), but for transect C. Filled circles in (a) and (c) indicate the location of current meters A1 and A1B 6 m and 10 m below the surface, respectively. Note that very cold waters ($T < 12$ °C) are below buoyant coastal current waters ($S < 31.5$ psu).

I present the temporal evolution of variables during our surveys in fig. 5.7. There the wind and the unfiltered data from the moorings are shown. Wind constitutes an important perturbation in the flow and density fields. The ship profiled the area on day 165 and 168. Winds prior were generally weak and upwelling favorable. A strong downwelling event centers on day 162 and a relaxation event on day 165 (fig. 5.7a). In fig. 5.7 the along-shore currents are always positive (downstream) after day 160, thus opposing the upwelling favorable winds. As I argued in chapter 4, this is the likely consequence of buoyancy forcing. More important in the present context is the passage of a temperature front on day 165 coincident with the relaxing winds (fig. 5.7a). The entire water column warms by more than 5° C (fig. 5.7c) while the salinity decreases by 2 psu (fig. 5.7d). Thus lighter, warmer waters pass our mooring array on day 165 at the time of maximum downstream flow (30 cm/s). Also in fig. 5.7 I mark the time intervals when we mapped the horizontal and vertical distribution of salinity and velocity with CTD and ADCP instruments. These I study next for day 168.

Three days after the first survey (fig. 5.6) the slopes of isolines and current directions have switched (fig. 5.8). The salinity transect upstream (fig. 5.8b) indicates that buoyant waters have detached from the bottom and the coast. They are replaced by cold water ($T < 12^\circ \text{C}$) from depth which surfaced near the shore. From a short time sequence of transect data (fig. 5.9) I deduce that downstream light water moved offshore and upstream. This hypothesis is confirmed by direct current measurements from an ADCP

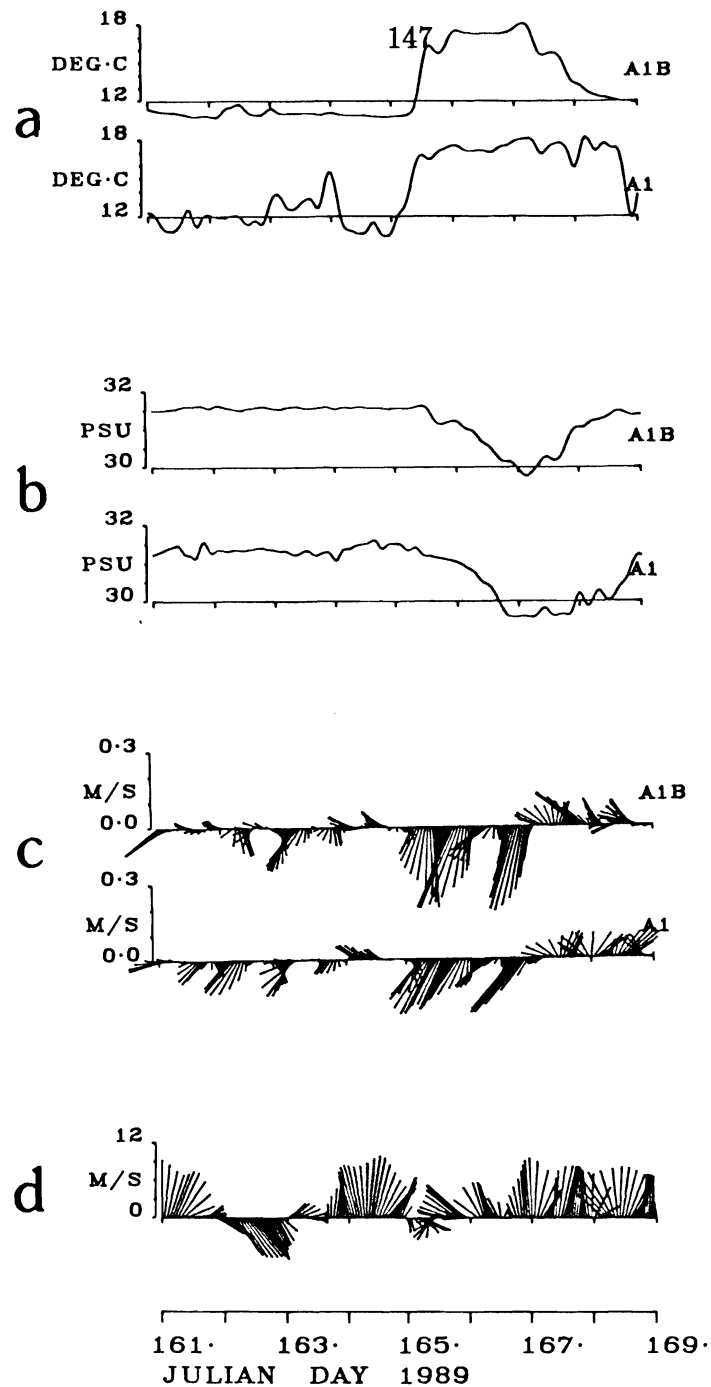


Figure 5.7. Hudson Coastal Current signals in time series. Shown are (a) temperature, (b) salinity, (c) current, and (d) wind for the period from June 10 (day 161) to June 18 (day 169) of 1989. For the location of current meters A1 and A1B see fig. 5.5. Note the arrival of warm, fresh coastal current water on June 14 (day 165). Currents during this episode peak at 30 cm/s and oppose the local winds.

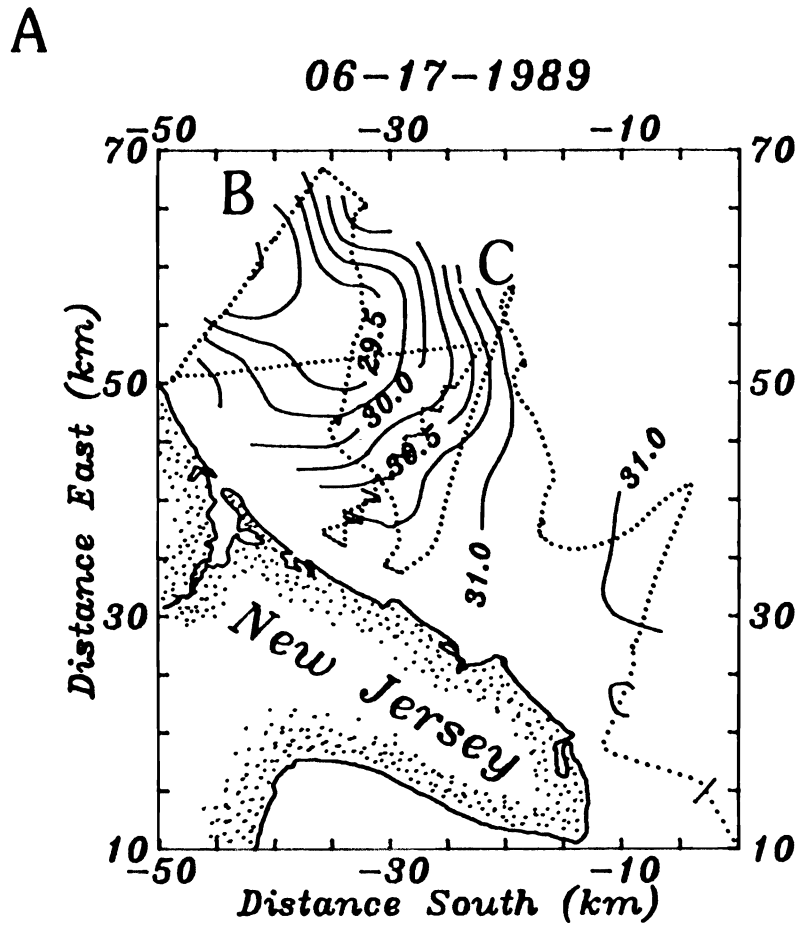


Figure 5.8. Hudson Coastal Current 06-17-1989. Buoyant waters from upstream moved downstream reaching transect C. Circulation induced by upwelling favorable winds advected the buoyant surface water off-shore (a), replaced them with cold waters from below, tilted isolines, and thus vertically stratified the water column (b and c).

Salinity

Temperature

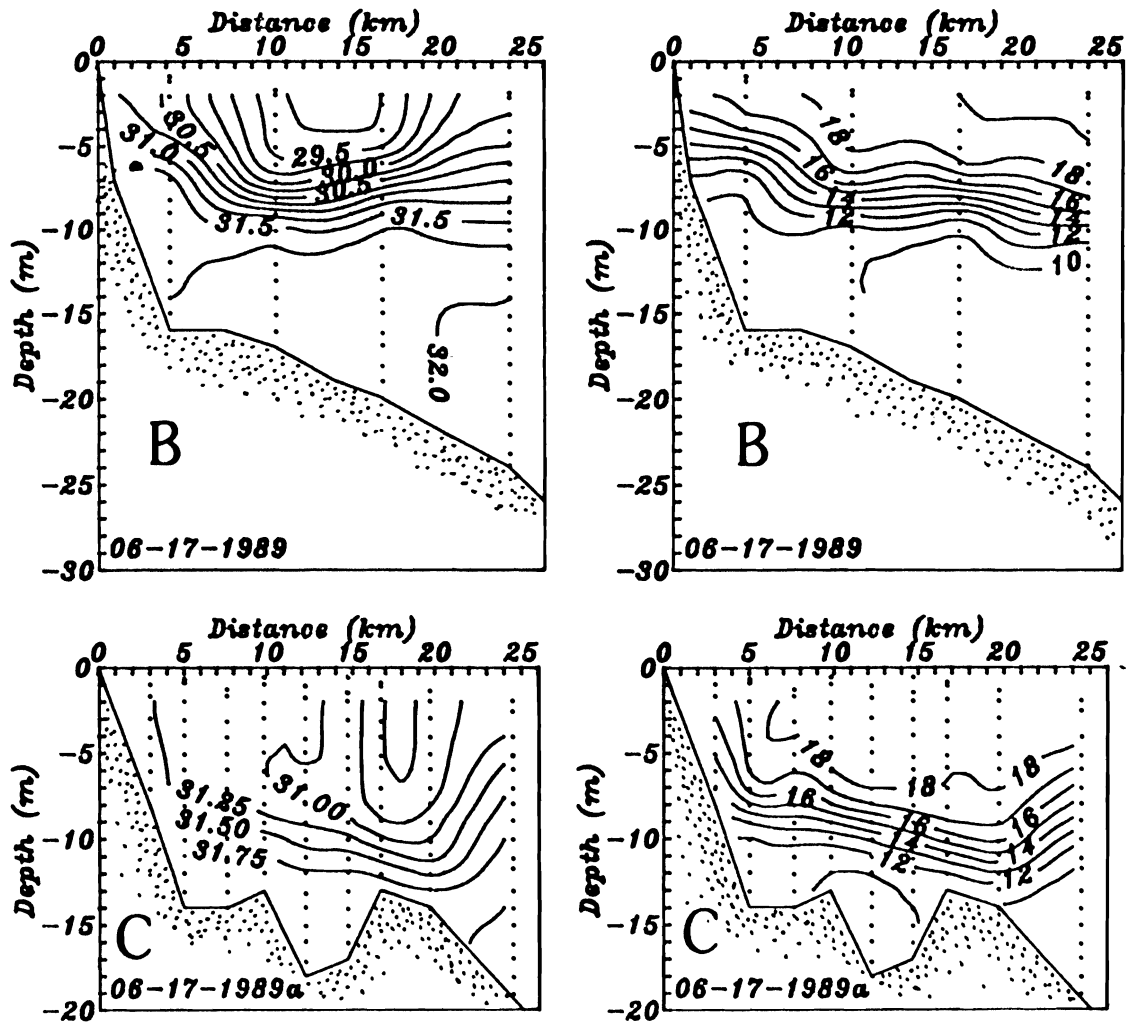


Figure 5.8. Hudson Coastal Current 06-17-1989. Buoyant waters from upstream moved downstream reaching transect C. Circulation induced by upwelling favorable winds advected the buoyant surface water off-shore (a), replaced them with cold waters from below, tilted isolines, and thus vertically stratified the water column (b and c).

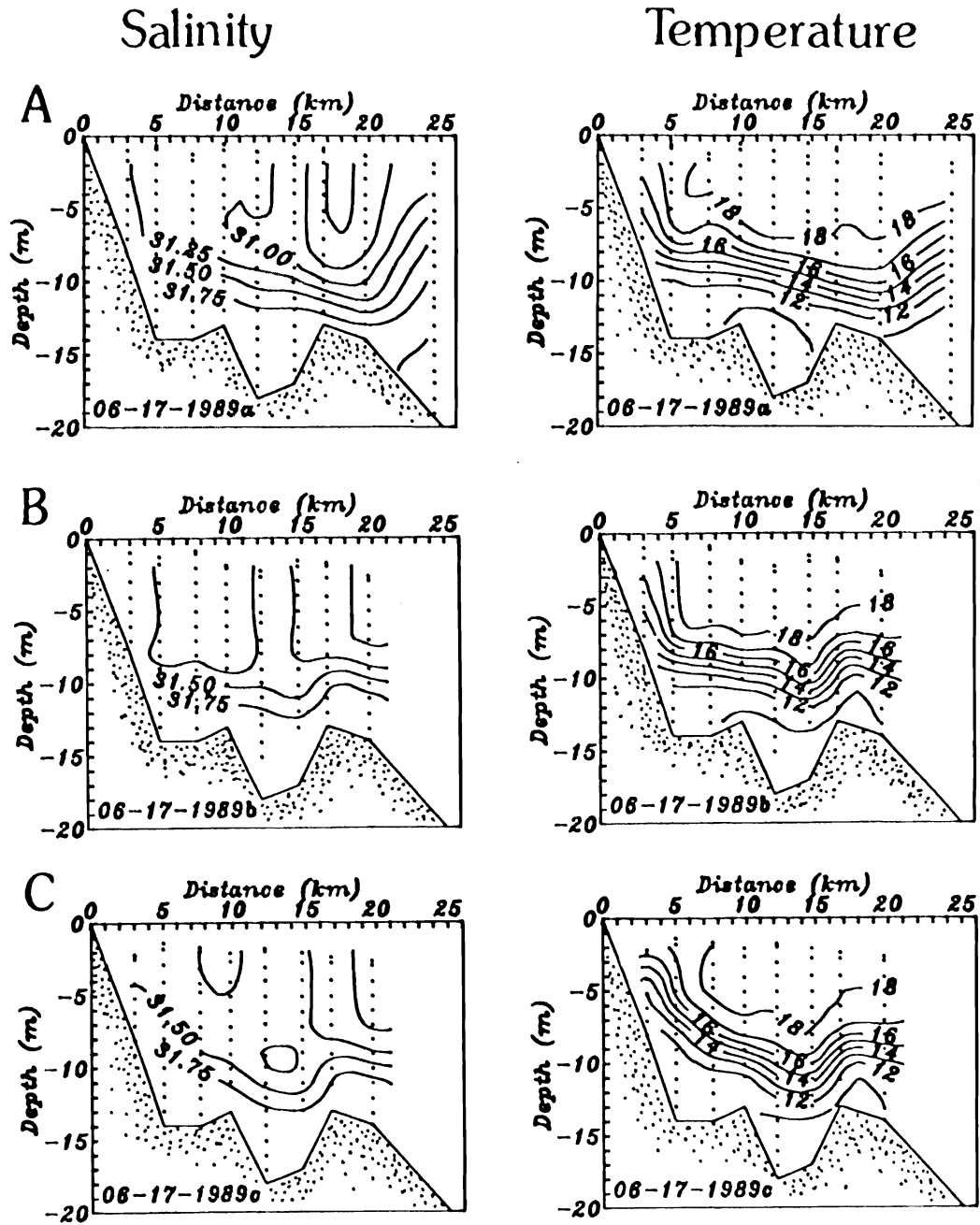


Figure 5.9. Retreat of the Hudson Coastal Current. Temporal sequence of salinity and temperature of transect C (see fig. 5.8 for location) on June 17, 1989. All three transects were taken within 9 hours.

that show a classical upwelling pattern with a strong onshore flow at depth (fig. 5.10). Note, however, that the Hudson Coastal Current must have moved farther downstream in the three days between the first and second survey (figs. 5.6 and 5.8), since buoyant waters are much lighter on day 168 than they were three days earlier. The surface salinity distributions emphasize this point.

I resolved the structure of the buoyant water very well as it moved offshore and upstream. The Hudson Coastal Current began its retreat as it responded to the upwelling favorable winds. Near the surface a strong offshore component is evident from drifter observations (not shown) while ADCP data imply that at mid-depth the flow was in the direction of the wind. At 10 m below the surface, however, I observe 5 cm/s onshore flow (fig. 5.10, see also fig. 4.14, p.111) which Ekman dynamics fail to explain (fig. 4.16, p.118). For the cause of this onshore flow I propose an along-shore pressure gradient that is balanced by the Coriolis force due to the flow toward the shore. The strong upwelling favorable winds (stress ≈ 0.1 to 0.2 N/m^2) set up an along-shore slope. The slope necessary to balance the remaining onshore flow of about 5 cm/s would be 5 cm in 100 km. Fitting a third order polynomial to 8 coastal sea level stations between Sandy Hook, NJ, and Duck, NC (Masse, 1988), I indeed find a slope in the study area between 8 cm per 100 km (day 167) and 3 cm per 100 km (day 169). The hypothesis of an along-shore pressure gradient balanced by an onshore flow is thus internally consistent with all other observations I have.

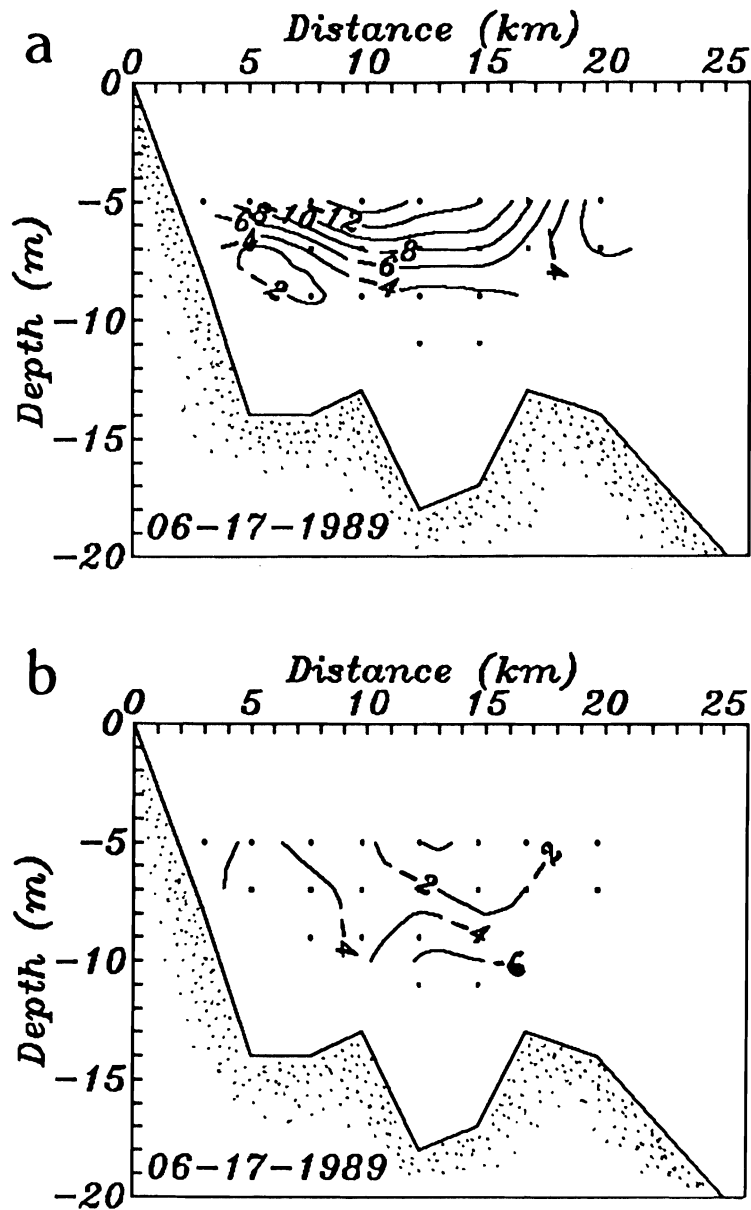


Figure 5.10. Transect of subtidal velocities 06-17-1989. Velocities are from ADCP profiling of transect C (see fig. 5.8 for location): (a) along-shore velocity component (negative is upstream); (b) across-shore velocity component (negative is onshore). Note the 6 cm/s onshore flow at depth.

In order to demonstrate that the above event is not a rarely occurring anomaly, I will discuss a second event where I again observe buoyant waters upstream from the mouth of the Delaware Estuary. Instead of a coherent tongue of buoyant waters, however, I here resolve a mature instability that has grown into an eddy. The horizontal surface salinity distribution off New Jersey (fig. 5.11) shows the dominance of that eddy as it interacts with the coastline in May 1989. In contrast to the previous event, the salinity field now consists of two vertical layers (fig. 2.3, p.15). The anti-cyclonic 5 m deep eddy is a buoyant layer which overlays ambient shelf waters. Upstream the lightest waters are next to the shore ($S < 29$ psu), while those of the eddy center are 15 km from the shore and are much lighter still ($S < 28$ psu). Since winds prior to this event were downwelling favorable for almost 10 days (fig. 5.12) it appears that the eddy shows the final downstream form of the Hudson Coastal Current. I may thus speculate on the existence of a fourth region of coastal currents, namely their final disintegration in the form of detaching eddies. Fig. 5.11 may well be an example of such a region.

5.3.3 Statistics

The low-pass filtered (2 day cut-off) time series of fig. 5.12 implies that no persistent downstream flow is maintained off New Jersey, in contrast to off Delaware. Instead, 150 km from the Hudson currents are highly variable and correlate well with the local winds. Salinities change little.

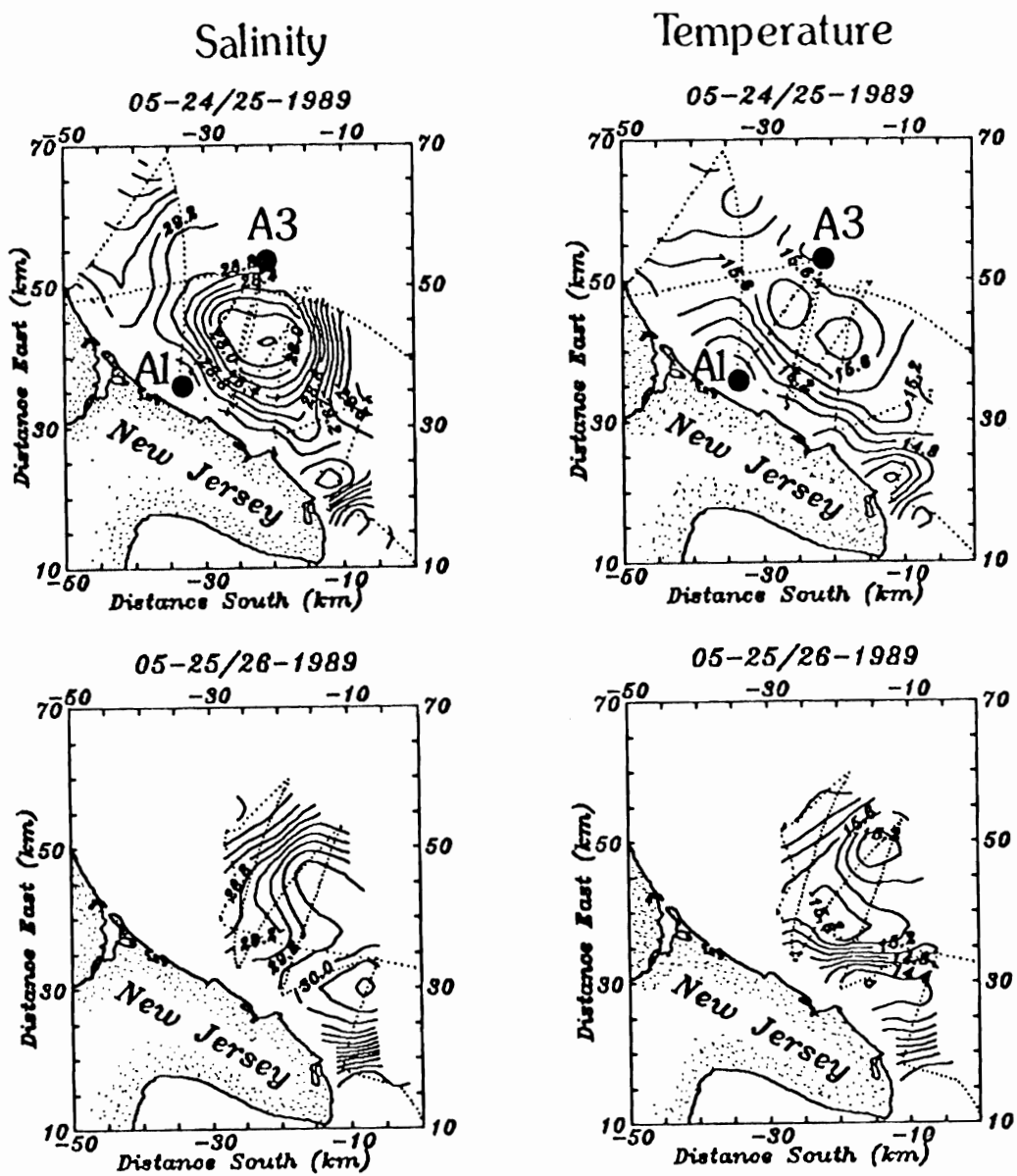


Figure 5.11. Coastal eddy off New Jersey. Surface salinity and temperature for two successive mappings off New Jersey in May 1989 (see also fig. 2.3, p.15). A warm, fresh eddy impinges on the coast. Winds and currents prior to this event were downwelling favorable and downstream, respectively (fig. 5.12). Filled circles indicate the location of two current meters.

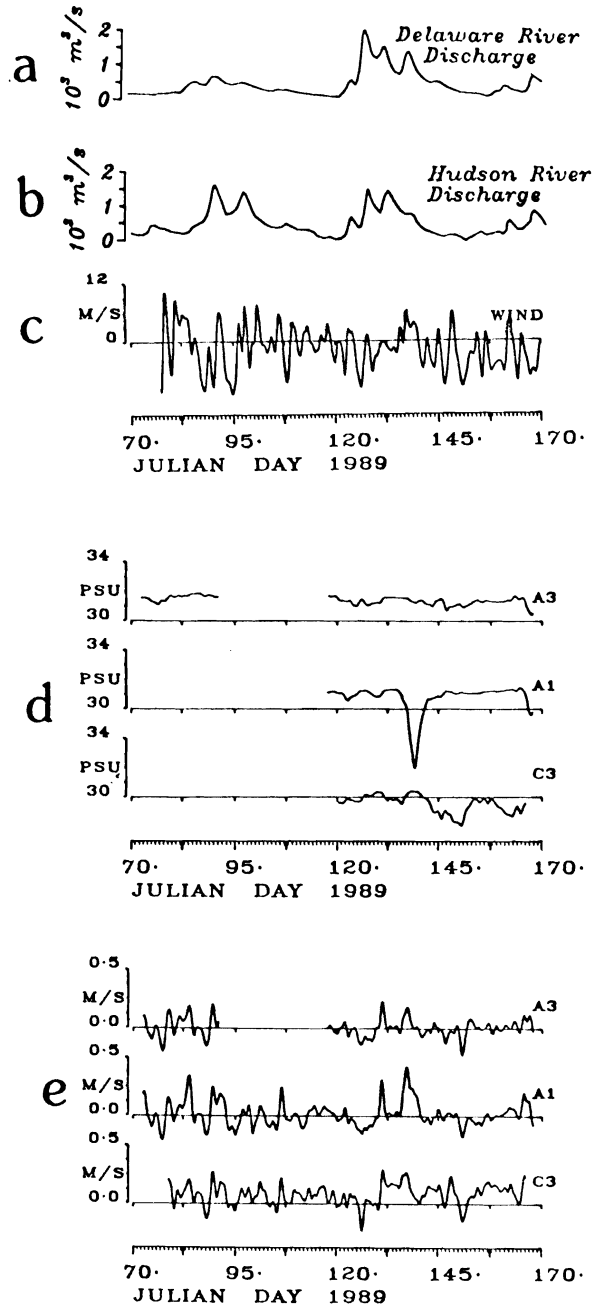


Figure 5.12. Discharge, wind, salinity, and current time series. I show fresh water discharge of (a) the Delaware River and (b) the Hudson River; (c) winds (downwelling favorable positive); (d) salinities; and (e) along-shore currents (downstream positive). The mooring locations A1 (inshore) and A3 (offshore) I marked in fig. 5.11. Mooring location C3 is about 70 km downstream and is always submerged in the Delaware Coastal Current. The salinity at A1 drops on day 140 by more than 5 psu and coincides with downstream currents that exceeded 40 cm/s.

Notable exceptions are two events when salinity decreases inshore by 6 psu and 3 psu on Julian day 138 and 168, respectively. It is these two events that I described above with shipboard data and that here I analyze statistically.

Since most of the high frequency subtidal variability (up to 5 days) correlates with the local winds, I first remove this part of the velocity and salinity record. I thus subtract from the original raw velocity or salinity data those signals that are partially coherent with the wind in a two input (wind and freshwater discharge), one output (velocity or salinity) system. In fig. 5.13a I then present the time domain cross-correlations of the de-winded data at various lags between Hudson River discharge and salinities off New Jersey. Maximum correlations with freshwater upstream are negative for salinity (fig. 5.13; increasing discharge decreases salinity) and positive for velocity (not shown; increasing discharge increases downshelf flow). Off New Jersey peak correlations are about 0.6 ± 0.25 at 7 and 49 days lag. The correlations reflect oscillatory forcing and response with a period of about 40 days. Indeed the freshwater discharge of the Hudson (and Delaware) peaks near Julian day 90, 125, and increases again near day 165 (fig. 5.12). From the present analysis alone I therefore cannot unambiguously determine which discharge event causes which salinity event.

In fig. 5.13b I present similar correlations, but now between Delaware River discharge and salinities off Delaware. I find similar

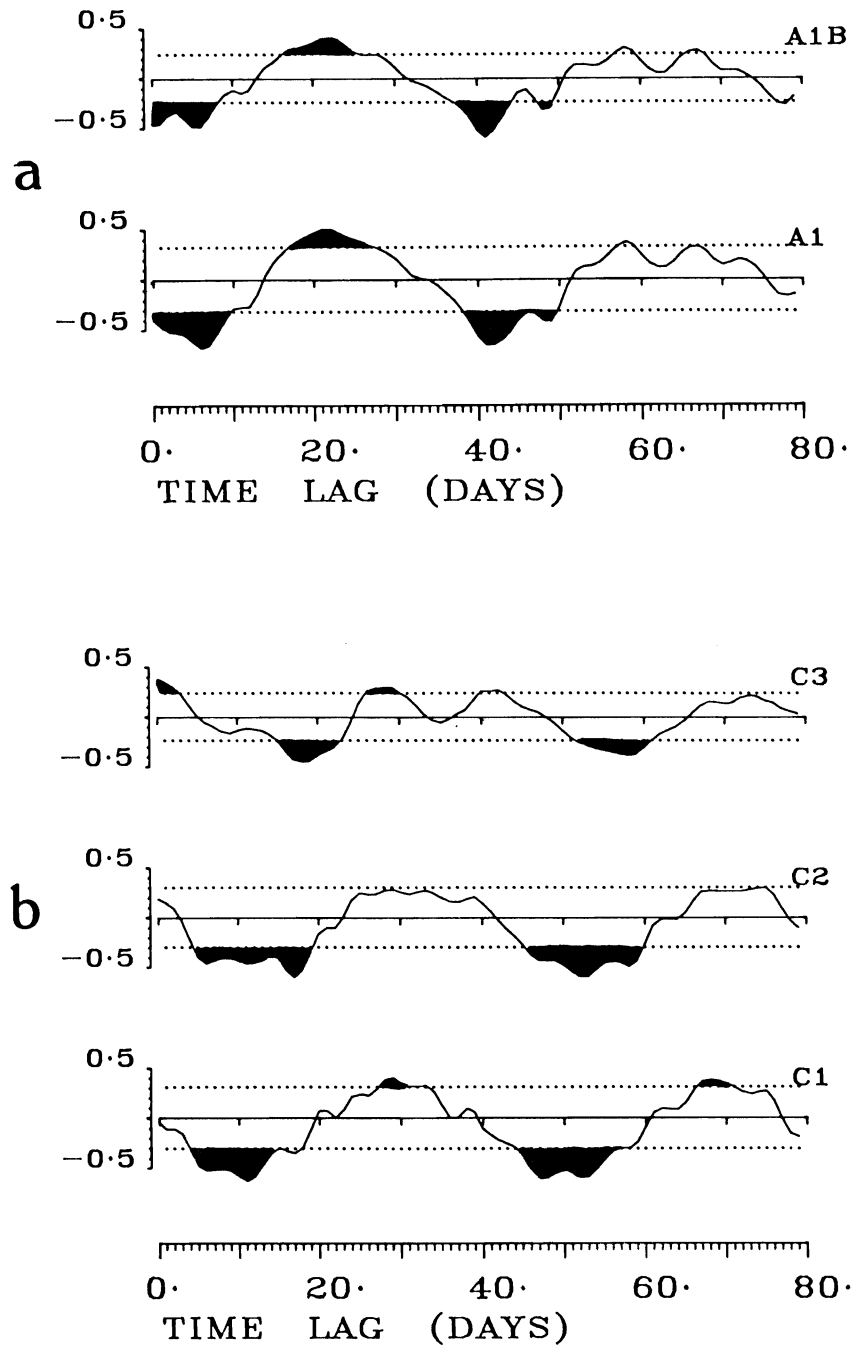


Figure 5.13. Cross-correlation of discharge with surface salinities. Data from the shelf (a) off New Jersey near the surface (A1) and bottom (A1B); see fig. 5.6 (p.144) for locations and (b) off Delaware at three surface meters C1, C2, and C3 (see fig. 4.10 (p.99, for locations). Largest significant correlations are negative (increasing discharge rates decrease salinities downstream) and are shown in black.

oscillatory behavior. Maximum correlations, however, occur at larger lags than those off New Jersey, namely 17 and 53 days. Garvine (1991) analyzed a much longer time series off Delaware and found correlations between discharge and salinity to peak between 10 and 20 days. I thus conclude that for the Delaware Coastal Current the response time to freshwater discharge is 17, not 53, days. Next I will demonstrate that for the correlations off New Jersey the reverse is true.

Off the coast of Delaware the mooring sites that are influenced by the discharge from the Delaware River are only 40 km from the mouth of the estuary or about 240 km from the freshwater gauge at Trenton, NJ. Off the coast of New Jersey the mooring sites influenced by the discharge from the Hudson River are more than 150 km downstream from the mouth of the estuary or about 350 km from the freshwater gauge at Greenville, NY, just upstream of Albany, NY. If the physical processes transporting buoyancy on the inner shelves off New Jersey and off Delaware are similar, then the lag times off New Jersey should be larger, not smaller, than those off Delaware, since the distance from the upstream buoyancy source is much larger. I thus argue that for the Hudson the second (49 days) lag is the correct response time while the first correlation peak is redundant.

But is the process I am implying, namely advection of buoyancy by the coastal currents, the correct process for both regimes? Consider an alternative: A linear baroclinic disturbance travels with the internal phase

speed $c_i = L_D f$, where f is the Coriolis parameter and L_D the internal deformation radius. Taking $L_D = 10$ km and $f = 10^{-4} \text{ s}^{-1}$, the phase speed is about 1 m/s. Thus the perturbation from the Hudson would arrive a few days later at our mooring location, hence favoring the 7 day time scale. A linear wave, however, does not transport material, but it may increase velocities and velocity shears, both of which would enhance vertical mixing, thus increasing salinities near the surface. I do not observe this and thus rule out a linear wave-like perturbation as the cause of the dramatic drops in salinities seen in fig. 5.12.

Finally, I emphasize that I observe the second decrease of salinity on day 165 on the New Jersey shelf but not on the Delaware shelf. The two discharge events of days 90 and 130 (see fig. 5.12, p.155) pass the mooring array off Delaware on Julian day 105 and 140, respectively. Off New Jersey, however, two freshwater events pass the mooring array on day 140 and 165 (see fig. 5.12). As there are only two major run-off events in the discharge record of the Hudson and Delaware rivers, I thus explain the presence of a salinity decrease on day 165 off New Jersey by the long response time to upstream buoyancy forcing more than a month earlier.

In summary I conclude that the salinity of the coastal waters off Atlantic City, NJ, responds to changes in freshwater run-off upstream about 50 days later. The waters off the coast of Delaware respond to similar changes in freshwater run-off upstream about 17 days later. Both time

scales thus favor the slow advection of salinity along the shelf.

5.4 Discussion, Scales, and Parameters

The above description of the coastal current region has focused on salinity since that variable best traces brackish estuarine waters on the shelf. In discussing dynamical properties of the flow, density and vorticity tendencies are more appropriate variables. While I have density transect data from which to estimate internal deformation radii, I lack velocity measurements to compute parameters depending upon velocity with the same confidence as I did in the source and plume regions. Nevertheless, in the plume region I discovered that the flow becomes linear and semi-geostrophic. I expect the same dynamics to hold in the coastal current region also. Geostrophic velocities from thermal wind computations will then provide reliable along-shore velocity scale estimates. These I will use here to estimate Froude and Rossby numbers.

In fig. 5.14 I present density data and corresponding thermal wind velocities relative to zero velocity at the bottom. While this choice certainly reflects subjective bias, I found few discrepancies between thermal wind speeds using this choice as compared with the thermal wind speeds that I obtained by using measured ADCP currents as reference speeds. Figs. 4.16 (p.118) and 4.17 (p.120) show fine examples of vanishing near bottom velocities in the coastal current. I average the along-shore geostrophic

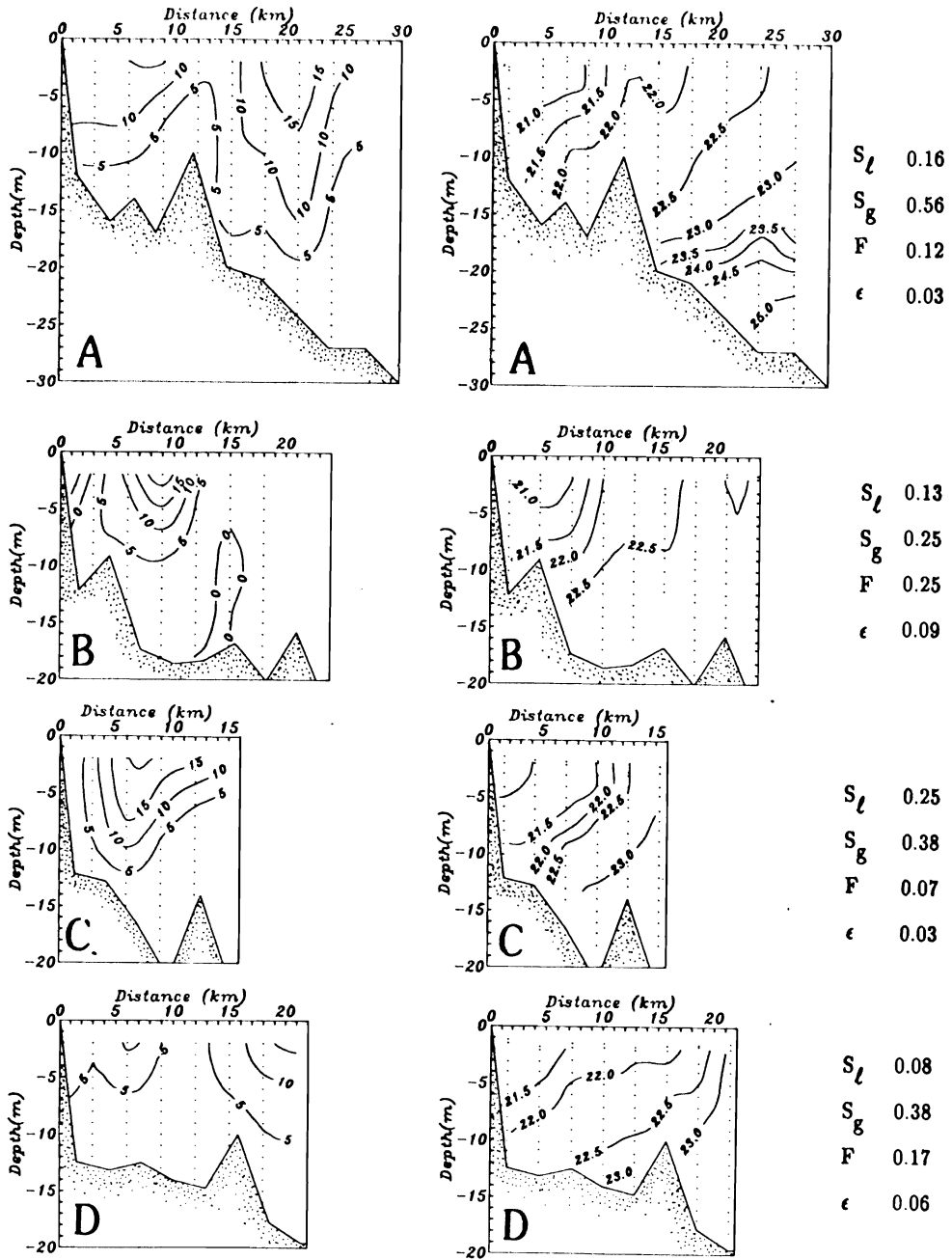


Figure 5.14. Thermal diagnostics for Delaware Coastal Current. Thermal wind speed (left panel) and density anomaly (right panel) on transect A,B,C, and D from June 1990. See fig. 5.4 (p.140) for the corresponding salinity map and the transect locations.

velocities due to the internal mass field over the entire transect to obtain a velocity scale (table 5.1). I then use the standard deviation from the section average of velocity to estimate the uncertainty of the derived parameters. The magnitude of the Rossby, Froude, and Burger numbers ϵ , F , and S , respectively, I label besides each transect (fig. 5.14) and list in table 5.1. All transects show a narrow jet with maximum speeds of about 20 cm/s at the density front. The flow is always subcritical ($F < 1$), but the most important finding here is that while both ϵ and S are much smaller than unity, their ratio is about 0.1. Once again this invalidates quasi-geostrophic dynamics (Pedlosky, 1986, p.364) while it calls for other models such as Cushman-Roisin (1986) or Allen et al. (1990).

The actual magnitudes of the parameters are insensitive to changes of the velocity scale within the deviation from a transect "mean" velocity. The Burger number S , though, is very sensitive to the choice of the geometric length scale L , since $S = (L_D/L)^2$, where L_D is the deformation radius. Hence, in table 5.1 I list both a global (S_g) and a local (S_ℓ) Burger number. The former reflects stratification only, since I take $L = L_g$ where L_g is the width of the coastal current at the mouth of the estuary (8 km). The local Burger number, in contrast, uses the local width of the current L_ℓ estimated from surface salinity maps, i.e., $L = L_\ell$. Since the current becomes unstable downstream and changes its width by more than 4 km (fig. 5.3, p.138), the local Burger number can be very different from the global one. In this section I do not attempt to estimate transverse current shear indicative of

Table 5.1. Scales and parameters for the coastal current region. The data to estimate the scales and parameters originate from June 1990 (see fig. 5.4, p. 140, for transect locations). The velocity scale U represents an average of the thermal wind velocity over the transect. The quantity ΔU is one standard deviation from the section mean U .

Transect:	A	B	C	D
L_D (km)	6.3	4.1	5.1	5.3
L_i (km)	0.8	1.0	0.4	0.9
L_ℓ (km)	15	11	10	18
S_ℓ	0.16	0.13	0.25	0.08
S_g	0.56	0.25	0.38	0.38
F	0.12	0.25	0.07	0.17
ϵ	0.03	0.09	0.03	0.06
U (cm/s)	3.8	7.0	2.7	7.2
ΔU (cm/s)	2.6	6.2	3.7	4.4

the magnitude of relative vorticity, because while the use of geostrophy gives a good velocity scale, its use to obtain velocity gradients is questionable.

In summary, even though the coastal currents in the Mid-Atlantic Bight become frequently unstable (see fig. 6.1, p.166), they can extend more than 100 km along the coasts from their respective buoyancy source upstream. I demonstrated the presence of buoyant waters from the Hudson River as far as 150 km downstream from its mouth. This alone emphasizes the importance of coastal currents for the along-shore distribution of material. The along-shore uniformity of dynamical parameters in the coastal current region of the Delaware Coastal Current implies that this region is distinct from the transitional plume region. Further, it implies that little dissipation takes place, since that would affect the overall structure of the coastal current and its parameters.

CHAPTER 6: AN INSTABILITY

6.1 Introduction

Over the last decade instability processes in the coastal ocean have received considerable attention (Griffiths and Linden, 1981; Petrie et al., 1987; Barth, 1989), even though field observations are generally rare. This is especially true for instabilities in very shallow water where Ekman numbers are $O(1)$. Further, most instability theories assume quasi-geostrophic dynamics which is inappropriate if finite changes in layer depth or bottom topography occur, as in the present application. The analytical studies of Barth (1989) and Gawarkiewicz (1991) are notable exceptions in this respect. They base their dynamics on more general primitive equations which they subject to infinitesimal perturbations. Here, however, I describe a mature instability that has finite amplitude.

Fig. 6.1 introduces the specific instability that I study in this chapter. It depicts two AVHRR images of sea surface temperature on Julian days 118 and 122. On day 118 a single meander is visible (fig. 6.1a) that develops four days later into a large amplitude instability with at least 4 meanders (fig. 6.1b). Hydrography (fig. 6.2) supports the notion that warm waters are relatively fresh and originate from the estuary, while the cold

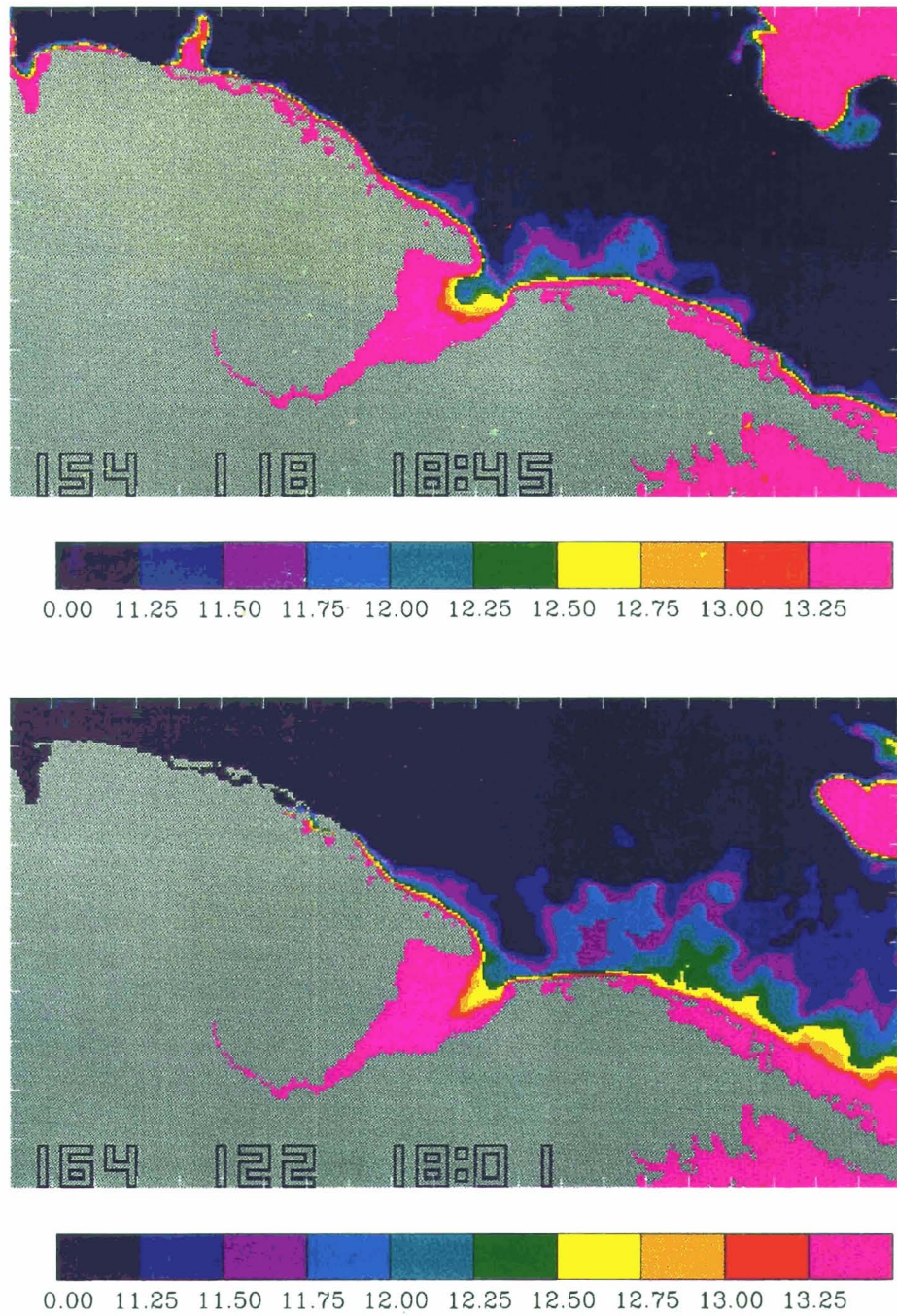


Figure 6.1. Instabilities from AVHRR sea surface temperature. (a) Day 118 (April 28, 1989), and (b) day 122 (May 2, 1989). Note the single meander in (a) that grows and propagates downstream (b).

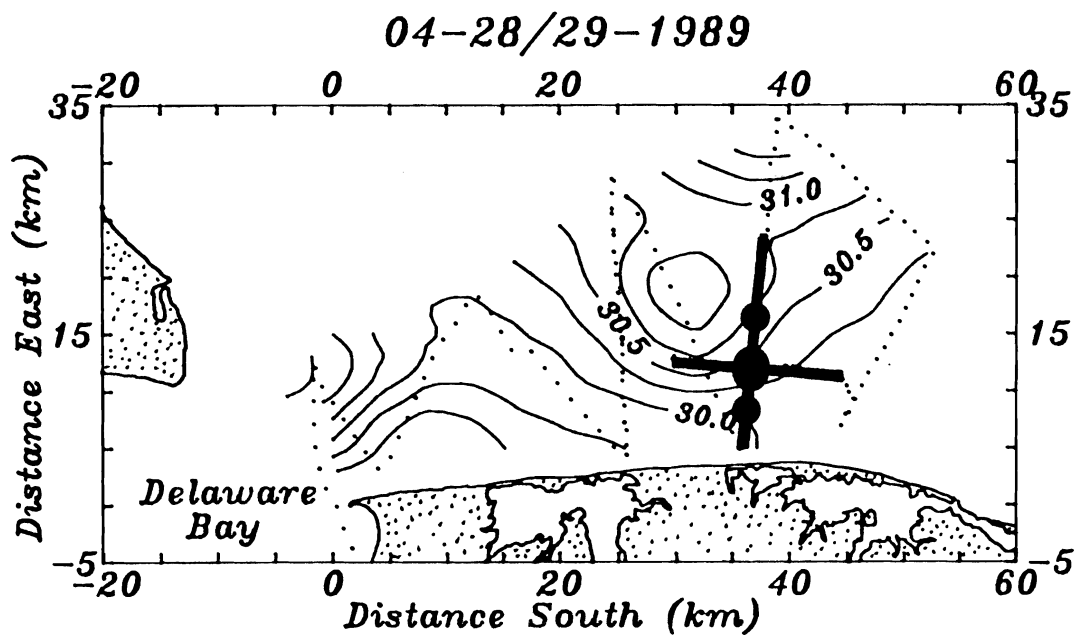


Figure 6.2. ADCP and CTD transect locations on salinity map. Sequentially, we first profiled the across-shelf transect (April 27), then the along-shelf one (April 28), and finally mapped the horizontal salinity field (April 28/29). I indicate S4 current meter locations as filled circles.

waters in the trough of the meander are relatively salty and represent shelf waters. I study this event in detail by diagnosing balances of mass and momentum at a single point. I will find a nondivergent flow with an along-shore balance between pressure gradients and local acceleration. The instability is thus highly time dependent.

The next section 6.2 will describe the instability of day 118 in much detail. In section 6.3 I then use the data to estimate terms in the depth averaged continuity and momentum equations at a point affected by the instability. The last section summarizes the results and outlines future studies.

6.2 Observations

In April 1989 an instability dominates the flow and density field off Delaware (fig. 6.1). From figs. 6.1 and 6.2 I estimate the dominant wavelength and amplitude of the instability to be about 40 and 10 km, respectively. Note, however, that in fig. 6.1b secondary instabilities with much smaller scales populate the first meander just downstream of the estuary. I can identify about 4 such smaller meanders on the first crest of the unstable coastal current (fig. 6.1b). Such features challenge numerical models, as they are very small scale (~1 km) and are often parameterized as "subgrid scale processes." To the observationalist, too, they are troublesome as they potentially alias larger scale features in shipboard surveys.

In fig. 6.3 I augment the surface salinity distribution with subtidal velocity vectors 5 m below the surface from ADCP profiling. Within 5 km of the coast the flow is weak and diffuse. Further off-shore, however, current speeds reach 20 cm/s. The flow is aligned with the isohalines and is thus qualitatively consistent with geostrophy, i.e., the circulation around the high salinity center (low pressure) is cyclonic. Thermal wind calculations of the along-shore velocity component reveal that the internal mass field explains most of the current variability within the transect (fig. 4.18, p.126). The along-shore velocity component, however, is always less than 10 cm/s (fig. 6.4a), while the across-shore velocity component reaches 16 cm/s about 15 km from the coast (fig. 6.4b).

The temporal evolution of currents at a point 8 km from the coast I present in fig. 6.5 where I complement a subtidal velocity time series from a moored current meter with velocity estimates from the ADCP. Both velocity components change by about 20 cm/s in only 6 hours. The signal is neither tidal nor wind driven (winds were generally less than 1 m/s) and I thus conclude that the coastal eddy or meander has moved over the station where the measurements were made. This hypothesis becomes clear in fig. 6.6 which depicts 3 along-shore density transects completed within 10 hours. The view in fig. 6.6 is from the coast toward off-shore. Initially, a density minimum occupies the center of the transect (fig. 6.6a). The flow associated with this density minimum accelerates downstream (see fig. 6.5, label "a"). As a result the light water moves downstream (to the right in fig. 6.6). The

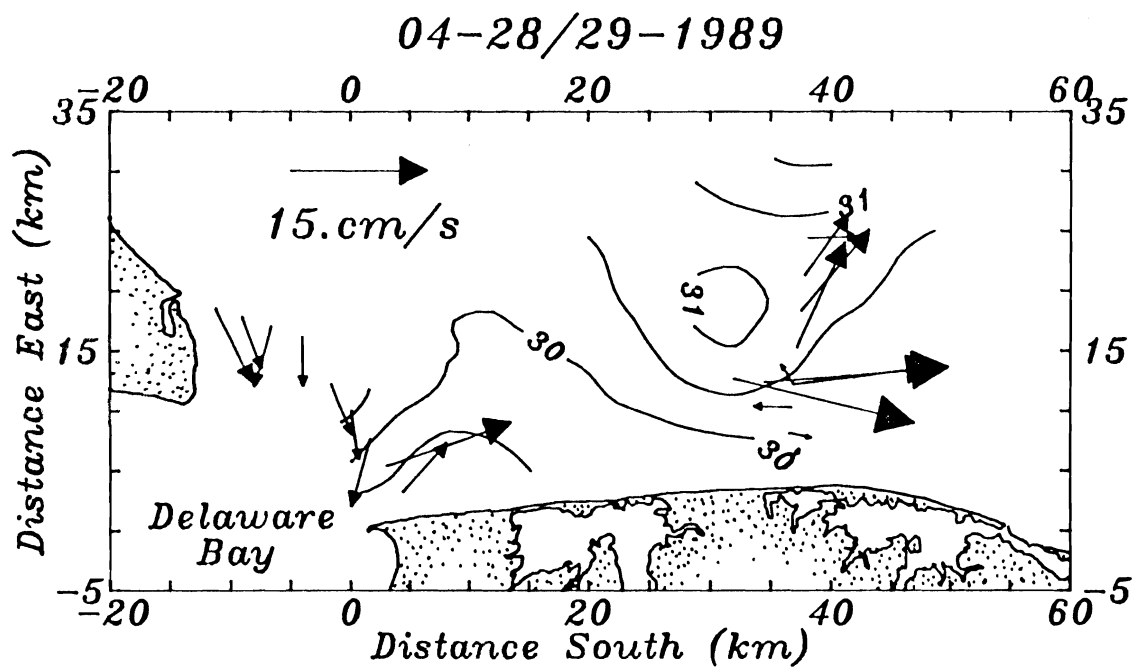


Figure 6.3. Subtidal surface velocity vectors on salinity map. The ship track for this mapping I show in fig. 6.2.

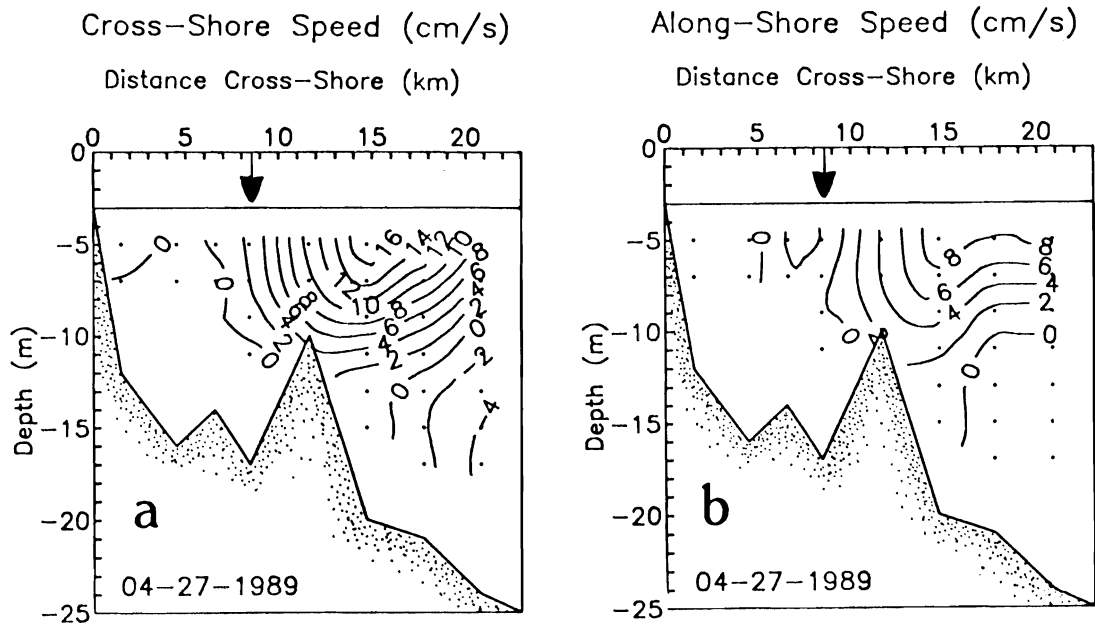


Figure 6.4. Across-shore subtidal velocity transect. (a) Cross-shore and (b) Along-shore speed. Notice the strong flow toward offshore near the surface about 15 km from the coast. The arrows indicate the location where the two transects of this section intersect (fig. 6.2).

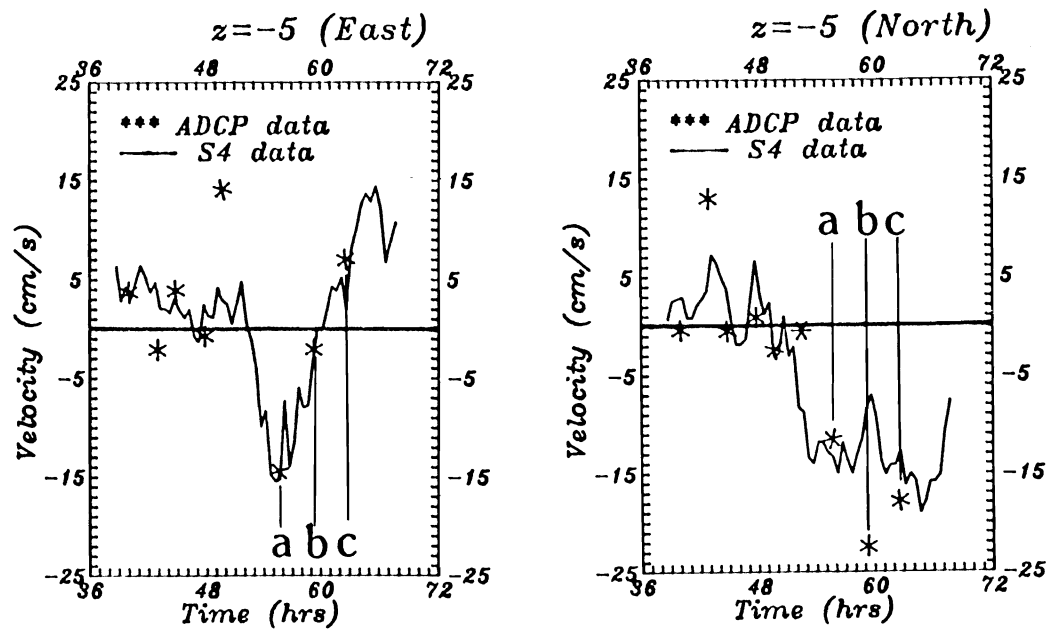


Figure 6.5. ADCP and S4 Current meter intercomparison. Shown in the right and left panels are the east and north component of the current vector. The location of this comparison is 5 m below the surface where the along- and across-shore transects intersect (see figs. 6.2, 6.4, and 6.7 for details). I label as (a), (b), and (c) the ADCP observations that correspond to the density transects shown in fig. 6.6.

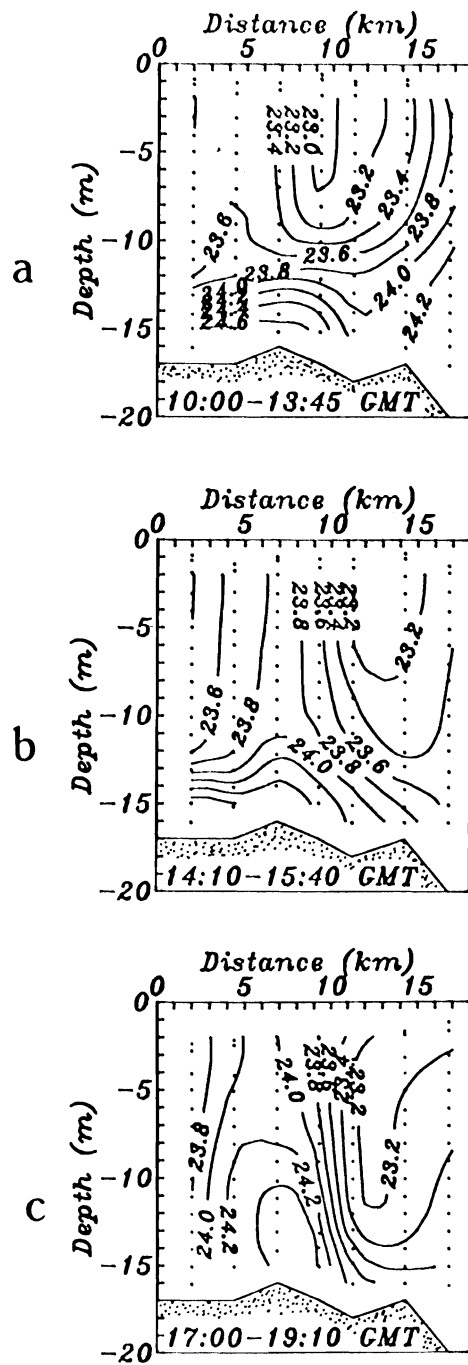


Figure 6.6. Three successive along-shore density transects. The sequence indicates that a meander propagates downstream, i.e., from left to right.

lighter water is then replaced by more saline water (fig. 6.6b). Fig. 6.6c presents the final view. Densities from upstream to downstream (left to right) first increase to about 1024.2 kg/m^3 , then decrease by about 1 kg/m^3 only to finally increase again. The transect of fig. 6.6c thus cuts across the crest and trough of the meander that I showed in figs. 6.1a and 6.2. The subtidal velocity components over this along-shore transect I depict in fig. 6.7. Qualitatively, the across-shelf velocity component is consistent with the geostrophic velocities in adjacent high and low pressure systems. The flow cannot, however, be nearly geostrophic, since it is highly time dependent (fig. 6.5). The dynamical analysis of the next section will indeed show that local acceleration is a major term in the momentum balance.

In this section I presented observations of a spatially and temporally variable instability that advects downstream. The flow is baroclinic; thermal wind explains the shear of the vertical currents well. Next I estimate the divergence and balance of forces of this flow from these data.

6.3 Balances

The data set that I presented above enables me to compute velocity and density gradients centered at the point where the along- and across-shore transects intersect. Wind and sea level data facilitate the computation of remaining terms in the momentum and continuity equations.

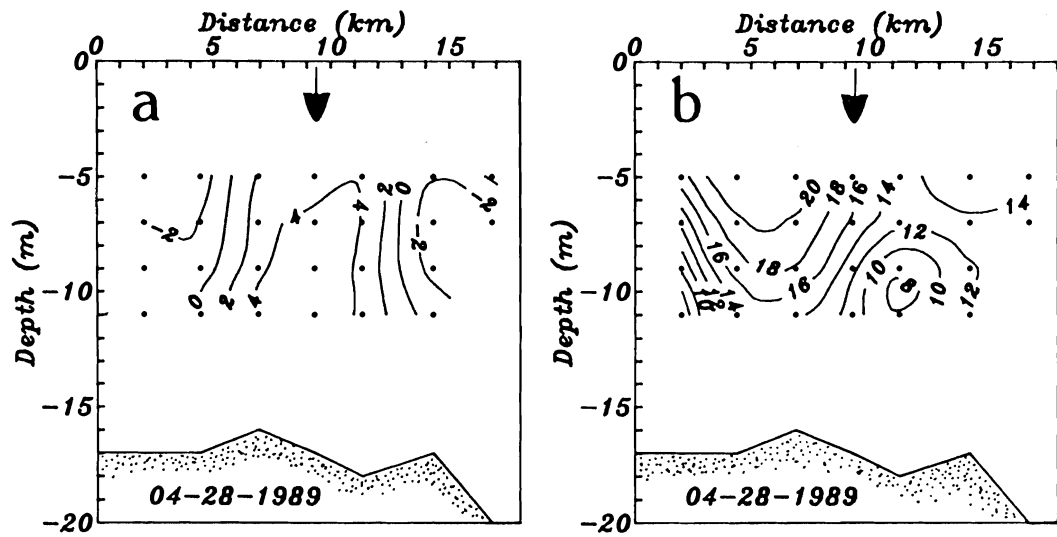


Figure 6.7. Along-shore subtidal velocity transects. I show (a) cross-shore (positive offshore), and (b) along-shore (positive downstream) currents. The arrows indicate the location where the along- and across-shore transects intersect (fig. 6.2).

The depth integrated continuity equation I write as

$$\partial_t \eta + \partial_x (uH) + \partial_y (vH) = 0$$

where (x,y) are along- and across-shelf co-ordinates positive downstream and off-shore, respectively. All terms should be computed from synoptically sampled data. My gradient estimates, however, are 13 hours apart, as we profiled first across and subsequently along the shelf. Since I here consider subtidal motion only, I assume that variables and their spatial gradients vary little within the 13 hours. I know, nonetheless, that speeds changed by about 20 cm/s within 6 hours (fig. 6.5) as the meander passed the transects. These difficulties result from inadequate Eulerian resolution of a feature that is more adequately described from a Lagrangian perspective (see also Maas, 1989). One should then interpret with caution all quantities in the following discussion that depend on the evaluation of spatial gradients. Nevertheless, I further assume constant depth and replace all derivatives by central differences with separation $\Delta x=3.7$ km, $\Delta y=5.0$ km, and $\Delta t=6$ hours. The continuity equation then becomes

$$\frac{1}{H} \frac{\Delta \eta}{\Delta t} (t_0) + \frac{\Delta (u)}{\Delta x} (t_0+13 \text{ hrs}) + \frac{\Delta (v)}{\Delta y} (t_0) = \epsilon_1$$

$$0.02 \quad -1.8 \pm 0.5 \quad +2.3 \pm 0.4 \quad 0.5 \pm 0.9$$

where the units of the numerical values below each term are 10^{-5} s^{-1} . The unbalanced residual I denote as ϵ_1 . The error bars here and in the following

are upper bounds due to 1 cm/s velocity error of each measurement that enters the estimation of a term. For example, the term Δu uses two velocity estimates and the error $\delta(\Delta u)$ is thus

$$\delta(\Delta u) = \left| \frac{\partial (\Delta u)}{\partial u_1} \right| \delta u_1 + \left| \frac{\partial (\Delta u)}{\partial u_2} \right| \delta u_2$$

and $\delta(\Delta u/\Delta x)$ is then $0.5 \times 10^{-5} \text{ s}^{-1}$, as I measure Δx , Δy , and Δt with negligible error. In any case, the results imply that the flow is nondivergent, since the time rate of change of the free surface is negligible in the continuity equation. The convergent along-shelf flow ($\partial_x u < 0$, fig. 6.4b) is roughly balanced by the divergent across-shelf flow ($\partial_y v > 0$, fig. 6.7a). The residual is $0.5 \pm 0.9 \times 10^{-5} \text{ s}^{-1}$ or about 25% of each of the two dominant terms. Closure is thus nearly obtained for the continuity equation.

The momentum balance is harder to establish as many more terms enter the balance. I write the depth averaged momentum equations as

$$\begin{aligned} \partial_t u + u \partial_x u + v \partial_y u - fv + g \partial_x \eta + (gH/2\rho_0) \partial_x \rho + ru/H - \tau_s^x / \rho H &= 0 \\ (1) \quad (2) \quad (3) \quad (4) \quad (5) \quad (6) \quad (7) \quad (8) \\ \partial_t v + u \partial_x v + v \partial_y v + fu + g \partial_y \eta + (gH/2\rho_0) \partial_y \rho + rv/H - \tau_s^y / \rho H &= 0 \end{aligned}$$

where the terms are local acceleration (1), nonlinear advection (2,3), Coriolis acceleration (4), barotropic (5) and baroclinic (6) pressure gradients, linearized bottom friction (7), and surface wind stress (8). In the baroclinic

pressure gradient (term 6) I assumed a depth independent density gradient $\nabla_h \rho$. The water depth I take as $H=17$ m. I estimate terms (1), (2), (3), (4), and (7) from the depth averaged ADCP velocity data, while I compute terms (5), (6), and (8) from sea level, density transect, and wind data, respectively. I estimate the velocity gradients in terms (2,3) by central differences while the Coriolis and frictional terms (4) and (7) I compute as the average of two estimates, namely those at time t_0 and at time t_0+13 hours, respectively. For the friction factor I used $r=5 \times 10^{-4} \text{ s}^{-1}$, a value at the lower end of the range of values used in the Mid-Atlantic Bight (Chapman et al., 1986; Pettigrew, 1981; Masse, 1988; Noble et al., 1983).

The numerical form for the along-shelf momentum balance is then

$$\begin{array}{cccccccccc} \frac{\Delta u}{\Delta t} & + & u \frac{\Delta u}{\Delta x} & + & v \frac{\Delta u}{\Delta y} & - & fv & + & g \frac{\Delta \eta}{\Delta x} & + & \frac{gH}{2\rho_0} \frac{\Delta \rho}{\Delta x} & + & \frac{r u}{H} & - & \frac{\tau_s^x}{\rho_0 H} & = & \epsilon_2 \\ +10.0 & & -1.0 & & +0.5 & -2.9 & & +6.9 & & -8.6 & & +0.1 & +0.0 & & & & 5.0 \\ \pm 1.0 & & \pm 0.5 & & \pm 0.5 & \pm 1.0 & & \pm 4.2 & & \pm ? & & \pm 0.5 & \pm 0.3 & & & & \pm 8.0 \end{array}$$

The units of the numerical values below each term are 10^{-6} m/s^2 . The balance is not closed, as the residual ϵ_2 is $5.0 \pm 8.0 \times 10^{-6} \text{ m/s}^2$. The uncertainty probably arises from inadequate estimation of the depth averaged currents and their gradients. The ADCP profiles currents reliably only between 5 m and 13 m below the surface in water that is about 17 m deep. The major terms in the balance, however, are local acceleration (term 1) and the pressure gradients (terms 5 and 6). Nonlinear advection terms

(2,3) are small and this balance is thus nearly linear. Bottom friction and Coriolis acceleration both contribute, but are always less than 30% of the major terms. The along-shore balance is thus complex, as many terms contribute. The flow is neither steady nor geostrophic in the along-shore direction at this point in space.

The across-shore momentum balance is even less clear, as I cannot estimate a potentially dominant term, namely the barotropic pressure gradient. Nevertheless, the respective depth-averaged equation is

$$\begin{array}{cccccccccc} \frac{\Delta v}{\Delta t} & + & u \frac{\Delta v}{\Delta x} & + & v \frac{\Delta v}{\Delta y} & + & fu & + & g \frac{\Delta \eta}{\Delta y} & + & \frac{gH}{2\rho_0} \frac{\Delta \rho}{\Delta y} & + & \frac{rv}{H} & - & \frac{\tau^y}{\rho_0 H} & = & \epsilon_3 \\ -5.0 & + & 0.3 & + & 0.7 & + & 5.5 & & ? & & +5.0 & + & 1.4 & + & 0.3 & + & 8.2 \\ \pm 1.0 & \pm & 0.5 & \pm & 0.5 & \pm & 1.0 & & \pm? & & \pm? & \pm & 0.9 & \pm & 0.3 & \pm & 4.2 \end{array}$$

where the units are the same as above. The residual ϵ_3 is now larger than any of the estimated terms as ϵ_3 is $8.2 \pm 4.2 \times 10^{-6} \text{ m/s}^2$. Now, however, I reemphasize that an important term is missing. The residual here could largely be compensated by a sloping sea level that is 0.8 cm higher at the coast than it is 10 km off-shore. Certainly, such a slope is not unreasonable. Even though the pressure gradients could then almost balance the Coriolis acceleration, the flow still has strong ageostrophic terms, especially the local acceleration (term 1). Again, all nonlinear terms are comparatively small, just as they were in the along-shelf balance.

In summary, I find the meandering disturbance of the coastal current (fig. 6.2) to be nondivergent. I find further that the momentum balance is nearly linear but that many terms contribute. Local acceleration and baroclinic pressure gradients dominate the momentum balance in both the across- and the along-shelf directions. I note, however, that I studied very local dynamics indeed, as I estimated all terms only for a single point in space and time. Hence I do not claim that the results are general, typical, or even characteristic. I claim, however, that underway profiling instruments such as the ADCP can provide far better estimates of terms in the momentum balance than fixed moored instruments do. Shipboard profiling instruments allow to resolve processes spatially. They thus lead to reliable spatial gradients of properties and allow the oceanographer to choose the spatial scale that one wants to analyze.

6.4 Discussion

Frequently, the coastal current exhibits meanders that occasionally develop into eddies. These instabilities have length scales that compare well with the internal deformation radius which is about 10 km. The vertical density structure of the flow is always partially mixed, a consequence of the $O(1)$ Ekman numbers. Hence the coastal current and its instabilities are always in contact with the bottom. The flow, however, is strongly baroclinic as lateral density gradients occur at all depths. Therefore I performed diagnostics that used depth-averaged dynamics. I retain a baroclinic

pressure gradient that, as it turns out, is a major term in the balance of forces. The analysis of the depth-averaged terms in the continuity and momentum equations respectively reveals a nondivergent and essentially linear flow. This is encouraging because, for example, one can then utilize a stream function. The large number of terms that enter the momentum balance, however, is discouraging. Besides local acceleration and pressure gradients, Coriolis forces are always important.

I judge the description of instabilities in this study incomplete at best. Most of the observational evidence covers the very large scale aspects only. I barely resolve the instability spatially; I do not resolve it temporally. Inadequate Eulerian measurement arrays do not well resolve moving features of the flow, such as the meander trough that I discussed in this chapter. Their dynamics I analyzed at a single point in space only. I am fully aware that the computed velocity gradients and thus the nonlinear terms are scale dependent measurements. Tidal and subtidal advection and dispersion act on the instabilities once they evolve. Further observational studies are clearly needed that should use underway profiling instruments such as the ADCP and the thermosalinograph. A sufficient number of drifters, deployed as moving current meters, will facilitate the computation of spatial gradients further. The goal should be to reliably estimate property gradients in the coastal ocean better than I did in this study.

As a first order model of the dynamics of the instability I advocate

a two layer model where both layers extend to the bottom and are separated by a front. Such a model could be constructed in the laboratory where finite amplitude instabilities can be observed under controlled conditions. Previous laboratory studies (Griffiths and Linden, 1981; Chabert D'Hieres et al., 1991) always modeled a shallow buoyant layer over a deep stagnant one. The simplicity of the proposed model geometry may also allow analytical instability analyses along the lines of Gawarkiewicz (1991). He emphasized the stabilizing effect of a sloping bottom.

CHAPTER 7: DISCUSSION AND PARAMETERS

The influx of buoyant waters into the coastal ocean affects the dynamics there profoundly. Lateral density gradients induce pressure gradients which, if balanced geostrophically, force an along-shore current in the direction of Kelvin wave phase propagation. The Delaware and Hudson estuaries each discharge about $750 \text{ m}^3/\text{s}$ of buoyant waters into the coastal ocean causing lateral density and pressure gradients. The fate of these outflows on the shelf of the Mid-Atlantic Bight was the subject of this dissertation.

From March through June of 1989 we repeatedly profiled fixed transects with shipboard CTD and ADCP instruments. A thermo-salinograph provided data to construct maps of surface salinities which proved extremely useful to interpret transect data in a three-dimensional context. I identified frontal regions, instabilities, and eddies throughout my study region. Data from current meters and clusters of satellite-tracked drifters provided rich Eulerian and Lagrangian flow field descriptions, respectively. I further secured wind, sea level, and freshwater discharge data for the entire Mid-Atlantic Bight, as well as all available AVHRR thermal imagery. I described a complex but coherent three-dimensional flow and density field and presented dominant momentum balances estimated from

data. I found three dynamically different regimes, namely a source, a plume, and a coastal current region. I may further speculate on the existence of a fourth region containing isolated eddies shed from finite amplitude instabilities upstream. These eddies, however, I observe on a single occasion only (fig. 5.11, p.154) and I therefore cannot generalize the results. Nevertheless, all three (or four) regimes are best summarized by nondimensional parameters such as Rossby, Burger, and Ekman numbers. Here I discuss the different regions using fig. 7.1 which summarizes the main results of this dissertation. It depicts the along-shore variability of the coastal current in terms of Rossby and Burger numbers, as well as the variability of vorticity ratios. As part of the discussion I also review theoretical results that relate to the Delaware Coastal Current in particular and buoyancy driven coastal currents in general.

Near the mouth of the estuary the source region turns the buoyant water anti-cyclonically over the entire water depth. Nonlinear inertial forces are important. The turning outflow, however, is separated from one coast as both the internal deformation radius and the inertial radius are much smaller than the width of the estuary. A strong, tidally modulated front separates seaward flowing, positively buoyant, estuarine waters from ambient shelf ones. Shelf water then enters the estuary beside, not below, the outflowing and turning jet. The width of the current exiting the estuary, though, matches the deformation radius so that the local Burger number is near unity. The Rossby number $\epsilon=U/(fL)$ is 0.15, but I interpret the ratio of

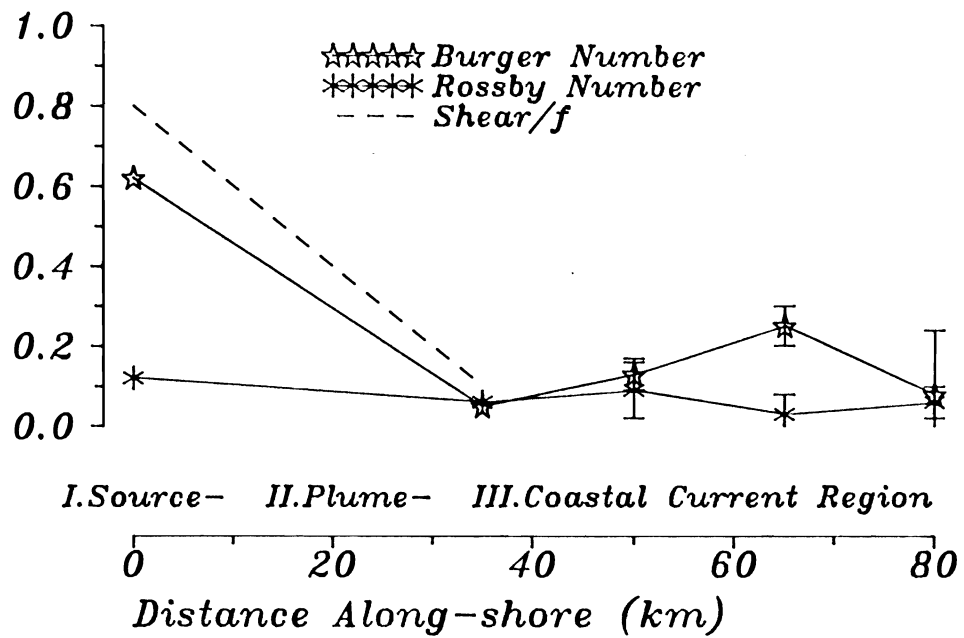


Figure 7.1. Along-shore variability of nondimensional parameters. The error bars represent uncertainties in the velocity scale and the width of the current. I omit them when I estimate parameters from the three experiments in March, April, and June 1989 that resolved tides.

relative to planetary vorticity (labeled shear/ f in fig. 7.1) as a better estimate of the Rossby number. The latter Rossby number reaches 0.8 and represents the frontal character of the source region. All these results are robust and insensitive to the freshwater discharge rates upstream.

Two three-dimensional models predict the tidal and subtidal circulation of the Delaware Estuary and the accompanying continental shelf. The finite element model of Walters (1991) prescribes the density field, reproduces observed tidal currents to within 5%, but fails to correctly predict the subtidal flow near the mouth of the estuary. The finite difference model of Galperin and Mellor (1990a, 1990b, and 1990c) solves both the density and the flow field simultaneously, reproduces observed tidal currents to within a factor of two, but fails equally to reveal the intriguing inflow/outflow arrangement of the subtidal flow near the mouth of the Delaware Estuary. The failures of the latter model will surface again below.

Downstream of the source region I find that buoyant waters mix with ambient shelf water and spread across the shelf from one to several local internal deformation radii (see fig. 4.2, p.72). Diffusive processes such as bottom friction thus appear to be active. Indeed, isopycnals intersect the sloping bottom near, but not at, the coast, while offshore they converge to a zone of enhanced density gradients. Isopycnals reaching the bottom are the major structural difference between this and the Alaska and Norwegian coastal currents which generally detach from the bottom. In this plume

region I find time mean currents at about 10 cm/s which oppose the mean upwelling favorable winds. Strongest currents occur where the isopycnal slopes are strongest. While thermal wind diagnostics of along-shore currents explain observed flows qualitatively, the quantitative comparison with ADCP data indicates that the vertical shear is not controlled by the internal mass field alone (fig. 4.17, p.120). This is not surprising, because upwelling favorable winds and sloping topography impose torques, too. Even though the bottom Ekman layer depth is of the same order as the water depth, I find statistically significant correlation between across-shore currents and along-shore winds. Waters move away and toward the coast near the surface and bottom, respectively. This implies a lateral surface slope which opposes the pressure gradients induced by the internal mass field. Trajectories from drifters also moved mostly downstream while drifting off-shore. Lagrangian auto-correlation time scales are similar to Eulerian time scales suggesting that nonlinear advective acceleration are unimportant in this region. Consistent with this, both local Rossby number ϵ and the ratio ξ/f of relative to planetary vorticity are much smaller than 1 (fig. 7.1). Burger number S , however, becomes smaller also, i.e.,

$$\epsilon \leq S \approx \xi/f \ll 1.$$

While the across-shelf momentum balance is geostrophic to first order, the governing vorticity equation is certainly not quasi-geostrophic, since S and ϵ are similar in magnitude. However, since the dynamical parameter S changes

by a factor of almost 10 from the source to the plume region (fig. 7.1), I interpret the latter as one of dynamic transition. Its structure includes an off-shore zone of enhanced density gradients.

The third dynamical region is the coastal current region. There the Delaware Coastal Current narrowed abruptly 40 km downstream from the source, increased its speed, and maintained its lateral structure at least another 50 km down-shelf. The current narrowed at a bend in the otherwise straight coastline. In 1989 surface drifters entering this regime under moderately downwelling favorable winds increased their speed from about 30 cm/s in the plume region to 50 cm/s downstream. I hypothesize that not until here was a coastal current finally established. Diffusive processes appear less dominant, as both Rossby and Burger numbers stayed nearly constant along the shelf in this region (fig. 7.1).

Twice I discovered remnants of the outflow from the Hudson River in my study area. The observed along-shore extent of the Hudson Coastal Current, more than 150 km, emphasizes the dramatic impact that coastal currents have on the coastal zone downstream. The Hudson Coastal Current that far from its source, however, appears only intermittently. Hence one could argue for a fourth region, namely that of final decay of coastal currents. As instabilities grow, they may generate eddies, which then become imbedded in the ambient flow. Future research should explore this region more systematically, since little is known of it.

Many theoretical models of buoyancy driven coastal currents have been proposed over the last decade. They fall into two distinct categories, namely process studies and general circulation models. The former generally concentrate on some isolated physical aspects of the flow, while the latter attempt to resolve many such processes. I first discuss reduced gravity and frictional models as examples of process studies. Thereafter I compare results from the general circulation models of Galperin and Mellor (1990a, 1990b, 1990c) and Chao (1987, 1988) with observations.

Reduced gravity models of coastal ocean circulation generally assume a shallow, buoyant surface layer that is dynamically active above a deep layer where the motion is independently set (Cherniawsky and LeBlond, 1986; Garvine, 1987; O'Donnell, 1990). One cannot apply these models to the circulation on the shelf off Delaware, Maryland, and New Jersey, because here a single buoyant layer occupies the entire water column. The dynamics of the source region, however, resembles many features modeled by Garvine (1987). I find the inertial turning of the buoyant waters and frontal regions to be similar to Garvine (1987) and O'Donnell (1990). These models, however, develop supercritical ($F > 1$) flow in contrast to the subcritical flow that I observe. The model of Cherniawsky and LeBlond (1986) is even less suited as it omits nonlinear advection and frontal structure by assuming small perturbations to a geostrophic basic state. A different, but equally inapplicable model is Zhang et al. (1987). This quasi-geostrophic model includes thin surface and bottom Ekman layers. The Delaware Coastal

Current, however, cannot possibly be quasi-geostrophic, because the "layer perturbations" extend over the entire depth. Quasi-geostrophic theory cannot accommodate such large "perturbations" (Flierl, 1984). Further, the Ekman numbers on the inner shelf of the Mid-Atlantic Bight are $O(1)$ which implies that the geostrophic interior and all Ekman layers overlap.

Frictional forces in the Delaware Coastal Currents extend over the entire water depth. Hence, frictional models such as proposed by Heaps (1972) and Vennell and Malanotte-Rizzoli (1990) should be more appropriate to model coastal currents in shallow water. As it turns out, however, they are not. Both models are steady, allow $O(1)$ vertical Ekman numbers, assume a vertically uniform mass field, but both models contain horizontal density gradients that drive the flow. Heaps (1972) prescribes a constant density gradient, ignores along-shelf variability, but resolves the resulting vertical current structure. In contrast, Vennell and Malanotte-Rizzoli (1990) solve for the density field as well, model horizontal variability with a stream function, but depth average all variables. The two models thus address different aspects of density driven shelf dynamics with friction. Heaps (1972) predicts currents with maximum downstream speeds near the surface. The current veers clockwise with depth (northern hemisphere) so that bottom flows are toward the coast. In the absence of density effects currents influenced by bottom stresses veer in the opposite sense, namely counter-clockwise. I interpret the onshore bottom current as the landward

return flow of the seaward extension of the estuarine gravitational circulation on the shelf. Pape and Garvine (1982) and Halliwell (1973) observed such bottom flows with drifters that were deployed near the sea bed in the Mid-Atlantic Bight and the Irish Sea, respectively. The along-shore surface currents in Heaps (1972), however, geostrophically balance the pressure gradients associated with the prescribed density field. The model does not, however, say how the density field is maintained.

The model of Vennell and Malanotte-Rizzoli (1990) concentrates on the spatial evolution of buoyancy forced currents. These originate from specified inflows either from the coast or from upstream. In order to avoid strong coupling between the density and the flow field, the inflow from the coast must be weak, less than 2 cm/s. This is an order of magnitude too small as compared to the outflow from the Delaware Estuary. Troublesome, however, is the monotonic increase (decrease) in current width (speed). Eventually, the current fills the entire 100 km wide shelf. Along with Heaps (1972) the authors appear to model larger scale aspects of the shelf circulation, i.e., large relative to the internal deformation radius L_D . Neither of the frictional models contain as a scale L_D as they both neglect vertical density variations. In the Delaware Coastal Current I observe small but finite vertical density gradients. These are dynamically important, since they determine L_D which is the dominant scale of motion.

Finally, I compare my observations with results from two general

circulation models, namely those of Galperin and Mellor (1990a, 1990b, 1990c) and Chao (1987, 1988, 1990). The former authors attempt to simulate the dynamics of the Delaware Estuary and the continental shelf in 1984 as realistically as possible. They employ real bottom topography and specify tidal, wind, freshwater discharge, and surface heat flux forcing functions. Even though freshwater discharge rates in 1984 and 1989 are comparable, the model results often disagree qualitatively with my observations from 1989. For example, I observe a buoyant plume off Delaware (fig. 4.2, p.72) under 7 different freshwater discharge and wind conditions. In the model simulations of Galperin and Mellor (1990a, 1990b, 1990c) this plume is always highly susceptible to local winds, often absent, and occasionally even found upstream. These model results clash with observations on the shelf. Inside the estuary the model results also clash with observations namely those of Wong and Münchow (1991). The model predicts saline waters near the Delaware side of the estuary and fresher waters near New Jersey for both upwelling and downwelling favorable winds (Galperin and Mellor, 1990b, p.273). Wong and Münchow (1991) report freshwater on both sides of the estuary. During upwelling favorable winds the model then predicts a buoyant plume on the shelf that moves upstream. During downwelling favorable winds a few days later no plume waters are found on the shelf. The reader may draw her or his own conclusion about the model performance on the shelf by comparing the many details of this dissertation with those of the model by Galperin and Mellor (1990a, 1990b, and 1990c).

A second, less ambitious, but more carefully designed general circulation model (Chao, 1988) purposely avoids simulating all aspects of estuarine shelf interaction. It succeeds, however, in realistically reproducing many aspects of the buoyancy driven coastal current that I observe. Chao's idealized model geometry consists of a rectangular box representing an estuary that opens onto a large continental shelf. He specifies the discharge of freshwater at the head of the estuary which, after reaching the continental shelf after some mixing in the estuary, forms a plume-like bulge and a narrow coastal current downstream. These are qualitative features that I observe in the Delaware Coastal Current as well. The model, however, neither simulates correctly the observed location of the bulge nor the vertical structure of observed variables for the Delaware Coastal Current. This deficiency probably arises from frictional coefficients that are too small for the Delaware Coastal Current. Chao (1988) chose eddy viscosities for a flow that was to resemble the outflow from the Chesapeake Bay. This coastal current off Virginia (Boicourt, 1973) exhibits much more vertical structure than the Delaware Coastal Current. Frictional effects in the former outflow are small and Chao (1988) uses vertical Ekman numbers that are $O(10^{-2})$. Off Delaware and New Jersey, in contrast, I find vertical Ekman numbers that are $O(1)$.

Chao (1988) further proposes the use of two nondimensional parameters for a classification of buoyant plumes and coastal currents. The first parameter, a densimetric Froude number, measures nonlinearity and

stratification. The second parameter measures the influence of friction. He organizes model results with these two parameters and distinguishes four different regimes. The flow is either supercritical ($F > 1$) or subcritical ($F < 1$) and either diffusive or nondiffusive. Within this scheme I identify the Delaware Coastal Current as diffusive–subcritical.

I finally note that the dynamical richness of the observed flow and density fields challenges present modeling capabilities, even though the basic ingredients are rather simple: Sloping isopycnals form an off–shore zone of large density gradients that reach the sloping bottom just off the coast. Moderately upwelling favorable winds oppose the along–shore current, induce depth dependent across–shore flow, and thus reduce isopycnal slopes. In contrast, downwelling favorable winds support the coastal current, induce depth dependent across–shore flow also, but this flow now keeps buoyant waters close to shore and increases the slopes of isopycnals. Tidal mixing, on the other hand, acts to homogenize the water column vertically, thus enhancing isopycnal slopes. Meanders and instabilities develop frequently. However, since downstream from the source region $\epsilon \leq S \ll 1$, I propose that a frontal geostrophic model with topography and friction will serve as a first step to understand the findings reported in this dissertation.

Observationally, I advocate use of continuously profiling instruments that move. The shipboard ADCP of this study and a towed undulating CTD (SEASOAR) are two specific examples of such instruments.

A drifter that carries profiling instruments is another. Only such instruments will adequately reveal the instability processes that often passed my instrument array. As that array was fixed in space, I barely resolved spatially, and did not resolve temporally, even the largest instabilities. Carefully designed drifter studies in conjunction with shipboard surveys that use the above instruments will provide information on the coastal ocean well beyond this study.

REFERENCES

- Ählnas, K., T.C. Royer, and T.H. George (1987). Multiple dipole eddies in the Alaskan Coastal Current detected with Landsat Thematic Mapper data. *J. Geophys. Res.*, 92, 13041–13047.
- Allen, J.S., J.A. Barth, and P.A. Newberger (1990). On intermediate models for barotropic continental shelf and slope flow fields. Part I: Formulation and comparison of exact solutions. *J. Phys. Oceanogr.*, 20, 1017–1042.
- Barlett, M.S. (1978). *Stochastic processes*. 3rd ed., Cambridge University Press, New York, NY.
- Barth, J.A. (1989). Stability of a coastal upwelling front. 2. Model results and comparison with observations. *J. Geophys. Res.*, 94, 10857–10883
- Barth, J.A. (1987). Stability of a coastal upwelling front over topography. PhD thesis. MIT/WHOI-87-48.
- Battisti, D.S. and A.J. Clarke (1982). A simple model for estimating barotropic tidal currents on continental margins with specific application to the M_2 tide off the Atlantic and Pacific coasts of the United States. *J. Phys. Oceanogr.*, 12, 8–16.
- Beardsley, R.C. and J. Hart (1978). A simple theoretical model for the flow of an estuary onto a continental shelf. *J. Geophys. Res.*, 83, 873–883.
- Bendat, J.S. and A.G. Piersol (1980). *Engineering applications of correlation and spectral analysis*. John Wiley, New York, NY.
- Blanton, J.O. (1981). Ocean currents along a nearshore frontal zone on the continental shelf of the eastern United States. *J. Phys. Oceanogr.*, 11, 1627–1637.
- Boicourt, W.C. (1973). The circulation on the continental shelf from Chesapeake Bay to Cape Hatteras. PhD Dissertation, The Johns Hopkins University, Baltimore, MD, 183pp.

- Bowman, M.J. and R.L. Iverson (1978). Estuarine and plume fronts. In: "Oceanic fronts in coastal processes," Bowman and Esaias (Eds.). Springer Verlag, New York, NY.
- Brink, K.H., R.C. Beardsley, P.P. Niiler, M. Abbott, A. Huyer, S. Ramp, T. Stanton, and D. Stuart (1991). Statistical properties of near-surface flow in the California Coastal Transition Zone. *J. Geophys. Res.*, 96, 14693–14706.
- Chabert d'Hieres, G., H. Didelle, and D. Obaton (1991). A laboratory study of surface boundary currents: Application to the Algerian Current. *J. Geophys. Res.*, 96, 12539–12548.
- Chao, S.-Y. (1990). Instability of fronts over a continental margin. *J. Geophys. Res.*, 95, 3199–3213.
- Chao, S.-Y. (1988). River forced estuarine plumes. *J. Phys. Oceanogr.*, 18, 72–88.
- Chao, S.-Y. (1987). Wind driven motion of estuarine plumes. *J. Phys. Oceanogr.*, 18, 1144–1166.
- Chao, S.-Y. and W.C. Boicourt (1986). Onset of estuarine plumes. *J. Phys. Oceanogr.*, 16, 21137–2149.
- Chapman, D.C., J.A. Barth, R.C. Beardsley, and R.G. Fairbanks (1986). On the continuity of mean flow between the Scotian shelf and the Middle Atlantic Bight. *J. Phys. Oceanogr.*, 16, 758–772.
- Chatwin, P.C. and C.M. Allen (1985). Mathematical models of dispersion in rivers and estuaries. *Ann. Rev. Fluid Mech.*, 17, 119–149.
- Cherniawsky, J. and P.H. LeBlond (1988). The baroclinic circulation in Hudson Strait. *Atmos. and Oceans*, 12, 417–426.
- Cherniawsky, J. and P.H. LeBlond (1986). Rotating flows along indented Coastlines. *J. Fluid Mech.*, 169, 379–407.
- Colin de Verdiere, A. (1983). Lagrangian eddy statistics from surface drifters in the eastern North Atlantic. *J. Mar. Res.*, 41, 375–398.
- Csanady, G.T. (1978). The arrested topographic wave. *J. Phys. Oceanogr.*, 8, 47–62.
- Cushman-Roisin, B. (1986). Frontal geostrophic dynamics. *J. Phys. Oceanogr.*, 16, 132–143.
- Davis, R.E. (1991). Lagrangian ocean studies. *Ann. Rev. Fluid Mech.*, 23, 73–64.

- Davis, R.E. (1985a). Drifter observation of coastal surface currents during CODE: The statistical and dynamical views. *J. Geophys. Res.*, 90, 4756–4772.
- Davis, R.E. (1985b). Drifter observation of coastal surface currents during CODE: The method and descriptive view. *J. Geophys. Res.*, 90, 4741–4755.
- Ekman, V.W. (1905). On the influence of the earth's rotation on ocean currents. *Ark. Mat. Astronom. Fys.*, 2, 55–108.
- Epifanio, C.E., A.K. Masse, and R.W. Garvine (1989). Transport of blue crab larvae by surface currents off Delaware Bay, U.S.A. *Marine Ecology Progress Series*, in press.
- Fischer, H.B., E.J. List, R.C.Y. Koh, J. Imberger, and N.H. Brooks (1979). *Mixing in inland and coastal water*. Academic Press, New York, N.Y.
- Flierl, G.R. (1984). Rossby wave radiation from a strongly nonlinear warm eddy. *J. Phys. Oceanogr.*, 14, 47–58.
- Foldvik, A., K. Aagaard, and T. Toerresen (1988). On the velocity field of the East Greenland Current. *Deep Sea Res.*, 35, 1335–1354.
- Freeland, H.J., P.B. Rhines, and T. Rossby (1975). Statistical observations of the trajectories of neutrally buoyant floats in the North Atlantic. *J. Mar. Res.*, 33, 383–404.
- Galperin, B. and G.L. Mellor (1990a). A time dependent, three-dimensional model of the Delaware Bay and River system. Part I: Description of the model and tidal analysis. *Estuar. Coast. Shelf Sci.*, 31, 231–253.
- Galperin, B. and G.L. Mellor (1990b). A time dependent, three-dimensional model of the Delaware Bay and River system. Part II: Three-dimensional flow field and residual circulation. *Estuar. Coast. Shelf Sci.*, 31, 255–281.
- Galperin, B. and G.L. Mellor (1990c). Salinity intrusion and residual circulation in Delaware Bay during the draught of 1984. In: "Residual currents and longterm transport," R.T. Cheng (Ed.), Springer Verlag, New York, NY.
- Garrett, C., J. Middleton, M. Hazen, and F. Majaess (1985). Tidal currents and eddy statistics from iceberg trajectories off Labrador. *Science*, 227, 1333–1335.

- Garrett, C. and B. Petrie (1981). Dynamical aspects of the flow through the Strait of Belle Isle. *J. Phys. Oceanogr.*, 11, 376–393.
- Garvine, R. W. (1991). Subtidal frequency estuary–shelf interaction: Observations near Delaware Bay. *J. Geophys. Res.*, 96, 7049–7064.
- Garvine, R.W. (1987). Estuary plumes and fronts in shelf waters: A layer model. *J. Phys. Oceanogr.*, 17, 1877–1896.
- Garvine, R.W. (1985). A simple model of estuarine subtidal fluctuations forced by local and remote wind stress. *J. Geophys. Res.*, 90, 11945–11948.
- Garvine, R.W. (1977). Observations of the motion field of the Connecticut River plume. *J. Geophys. Res.*, 82, 441–454.
- Garvine, R.W. (1974a). Physical features of the Connecticut River outflow during high discharge. *J. Geophys. Res.*, 79, 831–846.
- Garvine, R.W. (1974b). Dynamics of small scale oceanic fronts. *J. Phys. Oceanogr.*, 4, 557–569.
- Garvine, R.W., K.-C. Wong, and G.G. Gawarkiewicz (1989). Quantitative properties of shelfbreak eddies. *J. Geophys. Res.*, 94, 14475–14483.
- Garvine, R.W., K.-C. Wong, G.G. Gawarkiewicz, R.K. McCarthy, R.W. Houghton, and F. Akman III (1988). The morphology of shelfbreak eddies. *J. Geophys. Res.*, 93, 15593–15607.
- Gawarkiewicz, G.G. (1991). Linear stability models of shelfbreak fronts. *J. Phys. Oceanogr.*, 21, 471–488.
- Gent, P.R. and McWilliams (1983). Regimes of validity for balanced models. *Dyn. Atmos. Oceans*, 7, 167–183.
- Giessen, A. van der, W.P.M. de Ruijter, and J.C. Borst (1990). Three dimensional current structure in the Dutch coastal zone. *Neth. J. Sea Res.*, 25, 45–55.
- Gill, A.E. (1976). Adjustment under gravity in a rotating channel. *J. Fluid Mech.*, 77, 603–621.
- Grant, W.D., and O.S. Madsen (1986). The continental shelf bottom boundary layer. *Ann. Rev. Fluid Mech.*, 18, 265–305.
- Grant, W.D., and O.S. Madsen (1979). Combined wave and current interaction with a rough bottom. *J. Geophys. Res.*, 84, 1797–1808.

- Griffiths, R.W. and P.F. Linden (1981). The stability of buoyancy driven coastal currents. *Dyn. Atmos. Oceans*, 5, 281–306.
- Halliwell, A.R. (1973). Residual drift near the sea bed in Liverpool Bay: An observational study. *Geophys. J. R. Astr. Soc.*, 32, 439–458.
- Haskins, H.H. (1954). Final report—Part II to the U.S. Navy Hydrographic Office: Inshore survey—approaches to Delaware Bay. Unpublished manuscript.
- Hansen, D.V. and M. Rattray Jr. (1965). Gravitational circulation in estuaries. *J. Mar. Res.*, 23, 104–122.
- Heaps, N.S. (1972). Estimation of density currents in the Liverpool Bay area of the Irish Sea. *Geophys. J. R. Astr. Soc.*, 30, 415–432.
- Hickey, B.M., R.E. Thompson, H. Yih, and P.H. LeBlond (1991). Wind and buoyancy driven fluctuations in the Vancouver Island Coastal Current. *J. Geophys. Res.*, 96, 10507–10538.
- Hill, A.E. and J.H. Simpson (1988). Low frequency variability of the Scottish Coastal Current induced by along-shore pressure gradients. *Estuar. Coast. Shelf Sci.*, 27, 163–180.
- Hinze, J.O. (1975). *Turbulence*. McGraw-Hill, New York, NY.
- Hopkins, T.S. and A.L. Swoboda (1986). The nearshore circulation off Long Island, August 1978. *Cont. Shelf Res.*, 5, 431–473.
- Hoskins, B.J. (1975). The geostrophic momentum approximation and the semi-geostrophic equations. *J. Atmos. Sci.*, 32, 233–242.
- Ikeda, M., J.A. Johannessen, K. Lygre, and S. Sandven (1989). A process study of meso-scale meanders and eddies in the Norwegian Coastal Current. *J. Phys. Oceanogr.*, 19, 20–35.
- Johannessen, J.A., E. Svendsen, S. Sandven, O.M. Johannessen, and K. Lygre (1989). Three dimensional structure of meso-scale eddies in the Norwegian Coastal Current. *J. Phys. Oceanogr.*, 19, 3–19.
- Johnson, R.J., T.C. Royer, and J.L. Luick (1988). On the seasonal variability of the Alaskan Coastal Current. *J. Geophys. Res.*, 93, 12423–12437.
- Kirwan, A.D. Jr. (1988). Notes on the cluster method for interpreting relative motion. *J. Geophys. Res.*, 93, 9337–9339.

- Krauss, W. and C.W. Böning (1987). Lagrangian properties of eddy fields in the northern North Atlantic as deduced by satellite-tracked buoys. *J. Mar. Res.*, 45, 259–291.
- Kundu, P.K. and J.S. Allen (1976). Some three dimensional characteristics of low frequency current fluctuations near the Oregon coast. *J. Phys. Oceanogr.*, 6, 181–199.
- Lentz, S.J. and C.D. Winant (1986). Subinertial currents on the southern California shelf. *J. Phys. Oceanogr.*, 16, 1737–1750.
- Lopez, M, Clarke, A.J. 1989. The wind driven shelf and slope water flow in terms of local and remote response. *J. Phys. Oceanogr.*, 19,1091–1101.
- Maas, L.R.M. (1989). A comparison of Eulerian and Lagrangian current measurements. *Dtsch. Hydro. Zt.*, 42, 111–132.
- Mardia, K.V. (1972). *Statistics of directional data*. Academic Press, San Diego, CA.
- Masse, A.K. (1990). Withdrawal of shelf water into an estuary: A barotropic model. *J. Geophys. Res.*, 95, 16085–16096.
- Masse, A.K. (1988). Estuary–shelf interaction: Delaware Bay and the inner shelf. Phd Dissertation, University of Delaware, Newark, DE.
- Mayer, D.A, D.V. Hansen, and D.A. Ortman (1979). Long-term current and temperature observations on the Middle Atlantic shelf. *J. Geophys. Res.*, 84, 1776–1792.
- Mertz, G., M.J. El-Sabh, D. Proulx, A.R. Condal (1988). Instability of a buoyancy driven coastal jet: The Gaspe Current and its St. Lawrence precursor. *J. Geophys. Res.*, 93, 6885–6893.
- Mitchum, G.T. and A.J. Clarke (1986). The frictional nearshore response to forcing by synoptic scale winds. *J. Phys. Oceanogr.*, 16, 934–946.
- Monin, A.S. and A.M. Yaglom (1975). *Statistical fluid dynamics*, vol. 2. MIT Press, Cambridge, MA.
- Mooers, C.N.R. (1973). A technique for the cross-spectral analysis of pairs of complex-valued time series, with emphasis on properties of polarized components and rotary invariants. *Deep Sea Res.*, 20, 1129–1141.
- Mork, M. (1981). Circulation phenomena and frontal dynamics of the Norwegian Coastal Current. *Phil. Trans. Roy. Soc. Lond.*, A302, 635–647.

- Münchow, A., A. K. Masse, and R. W. Garvine (1991a). Astronomical and nonlinear tidal currents in a coupled estuary shelf system. *Cont. Shelf Res.* (in press).
- Münchow, A., R. W. Garvine, and T. F. Pfeiffer (1991b). Subtidal currents from a shipboard acoustic Doppler profiler in tidally dominated waters. *Cont. Shelf Res.* (in press).
- Mysak, L.A. 1980. Recent advances in shelf wave dynamics. *Rev. Geophys. Space Phys.* 18, 211–241.
- Nihoul, J.C.J. and F.C. Roday (1975). The influence of "tidal stress" on the residual circulation. *Tellus*, 27, 484–489.
- Noble, M, B. Butman, and E. Williams (1983). On the longshelf structure and dynamics of subtidal currents on the eastern United States continental shelf. *J. Phys. Oceanogr.*, 13, 2125–2147.
- O'Donnell, J. (1990). The formation and fate of a river plume: A numerical model. *J. Phys. Oceanogr.*, 20, 551–569.
- O'Donnell, J. (1988). A numerical technique to incorporate frontal boundaries in two dimensional layer models of ocean dynamics. *J. Phys. Oceanogr.*, 18, 1584–1600.
- Pape, E.H. III and R.W. Garvine (1982). The subtidal circulation in Delaware Bay and adjacent shelf waters. *J. Geophys. Res.*, 87, 7955–7970.
- Pedlosky, J. (1986). *Geophysical fluid dynamics*. 2nd edition, Springer Verlag, New York, NY.
- Petrie, B., B.J. Topliss, and D.G. Wright (1987). Coastal upwelling and eddy development off Nova Scotia. *J. Geophys. Res.*, 89, 12979–12991.
- Pettigrew, N.R. (1981). The dynamics and kinematics of the coastal boundary layer off Long Island. PhD thesis, MIT/WHOI.
- Poulain, P.-M. and P.P. Niiler (1989). Statistical analysis of the surface circulation in the California Current system using satellite-tracked drifters. *J. Phys. Oceanogr.*, 19, 1588–1603.
- Pratt, L.J. and M.E. Stern (1986). Dynamics of potential vorticity fronts and eddy detachment. *J. Phys. Oceanogr.*, 16, 1101–1120.
- Richardson, P.L. (1983). Eddy kinetic energy in the North Atlantic. *J. Geophys. Res.*, 88, 4355–4367.

- Riser, S.C. and H.T. Rossby (1983). Quasi-Lagrangian structure and variability of the subtropical western North Atlantic. *J. Mar. Res.*, 41, 127-162.
- Royer, T.C. (1983). Observations of the Alaskan Coastal Current. In: "Coastal Oceanography;" H. Gade, A. Edwards, H. Svendsen (Eds), Plenum Publishing Corp.
- Royer, T.C., J.A. Vermesch, T.J. Weingartner, H.J. Niebauer, and R.D. Muench (1990). Ocean circulation associated with the Exxon Valdez oil spill. *Oceanography*, 2, 3-10.
- Ruijter, W.P.M. de, A. van der Giessen, and F.C. Groenendijk (1990). Current and density structure in the Netherlands coastal zone. Proceedings 5th International Conf. on Physics of Estuaries and Coastal Seas, Gregynog 1990, Springer Verlag, Heidelberg, Germany (in press).
- Saetre, R., J. Aure, and R. Ljoen (1988). Wind effects on the lateral extension of the Norwegian coastal waters. *Cont. Shelf Sci.*, 8, 239-253.
- Salmon, R. (1983). Practical use of Hamilton's principle. *J. Fluid Mech.* 132, 431-444.
- Send, U. (1989). Vorticity and instability during flow reversal on the continental shelf. *J. Phys. Oceanogr.*, 19, 1620-1633.
- Simpson, J.E. (1987). Gravity currents in the environment and laboratory. Wiley, New York, NY.
- Simpson, J.H., E.G. Mitchelson-Jacob, and A.E. Hill (1989). Flow structure in a channel from an Acoustic Doppler Current Profiler. *Cont. Shelf Sci.*, 10, 589-603.
- Simpson, J.H. and A.E. Hill (1986). The Scottish Coastal Current. In: "The role of freshwater outflow in coastal marine ecosystems," S. Skreslet (Ed.), NATO ASI Series G.: Ecological Science, Vol. 7, 453 pp.
- Simpson, J.H. and R.D. Pingree (1978). Shallow sea fronts produced by tidal stirring. In: "Oceanic fronts and coastal processes," Bowman and Esaias (Eds.), Springer Verlag, Berlin, Germany.
- Simpson, J.H. and J.R. Hunter (1974). Fronts in the Irish Sea. *Nature*, 250, 404-406.

- Smith, S.D. (1988). Coefficients for sea surface wind stress, heat flux, and wind profiles as a function of wind speed and temperature. *J. Geophys. Res.*, 93, 15467–15472.
- Sokal, R.R. and F.J. Rohlf (1981). *Biometry*. 2nd edition, Freeman, New York, NY. 859pp.
- Stern, M.E. (1989). Evolution of locally unstable shear flow near a wall or coast. *J. fluid Mech.* 198, 70–99.
- Stern, M.E. and J.A. Whitehead (1990). Separation of a boundary jet in a rotating fluid. *J. Fluid Mech.*, 217, 41–69.
- Stern, M.E. and L.J. Pratt (1985). Dynamics of vorticity fronts. *J. Fluid Mech.*, 161, 513–532.
- Tang, C.L. (1980). Mixing and circulation in the north western Gulf of St. Lawrence: A study of a buoyancy driven current system. *J. Geophys. Res.* 85, 2787–2796.
- Taylor, G.I. (1921). Diffusion by continuous movements. *Proc. London Math. Soc.*, A20, 196–211.
- Tennekes, H. and J.L. Lumley (1972). *A first course in turbulence*. MIT Press, Cambridge, MA.
- Thompson, K.R. and D.T. Pugh (1986). The subtidal behavior of the Celtic Sea— Part II. Currents. *Cont. Shelf Res.*, 5, 321–346.
- Thompson, L.A. and W.R. Young (1989). An upper bound on the size of sub mesoscale vortices. *J. Phys. Oceanogr.*, 19, 233–237.
- Thompson, R.E. and R.E. Wilson (1987). Coastal countercurrent and mesoscale eddy formation by tidal rectification near an oceanic cape. *J. Phys. Oceanogr.*, 17, 2096–2126.
- Vennell, M.R. and P. Malanotte-Rizzoli (1990). The influence of a steady baroclinic deep ocean on the shelf: The vertical well-mixed case. *J. Phys. Oceanogr.*, 20, 489–505.
- Walters, R.A. (1991). A 3-D, finite element model for coastal and estuarine circulation. *Cont. Shelf Res.* (in press).
- Weaver, A.J. and W. Hsieh (1987). The influence of buoyancy flux from estuaries on the continental shelf circulation. *J Phys. Oceanogr.*, 17, 2127–2140.

- Whitehead, J.A. (1989). Internal hydraulic control in rotating fluids – Applications to the oceans. *Geophys. Astrophys. Fluid Dyn.*, 48, 169–192.
- Whitehead, J.A. and D.C. Chapman (1986). Laboratory observations of a gravity current on a sloping bottom: The generation of shelf waves. *J. Fluid Mech.*, 172, 373–399.
- Wong, K–C. and A. Münchow (1991). Buoyancy forced interaction between estuary and inner shelf: Observation. *J. Geophys. Res.* (submitted).
- Woods, A.W. and R.C. Beardsley (1988). On the barotropic discharge of a homogeneous fluid onto a continental shelf. *Cont. Shelf Sci.*, 8, 307–327.
- Zhang, Q.H., G.S. Janowitz, and L.J. Pietrafesa (1987). The interaction of estuarine and shelf waters: A model and applications. *J. Phys. Oceanogr.*, 17, 455–469.
- Zimmerman, J.F.T. (1986). The tidal whirl–pool: A review of horizontal dispersion by tidal and residual currents. *Neth. J. Sea Res.*, 20, 133–154.
- Zimmerman, J.F.T. 1980. Vorticity transfer by tidal currents. *J. Mar. Res.*, 38, 601–630.